ENGINYERIA ELECTRÒNICA ELÈCTRICA I AUTOMÀTICA

UNIVERSITAT ROVIRA I VIRGILI

Graduate Students Meeting on Electronics Engineering

Tarragona, Spain. June 28 - 29, 2018

BOOK OF ABSTRACTS

IEEE

ENGINYERIA ELECTRÒNICA ELÈCTRICA I AUTOMÀTICA

UNIVERSITAT ROVIRA I VIRGILI

Graduate Students Meeting on Electronics Engineering

Tarragona, Spain. June 28 - 29, 2018

Programme

Thursday June 28th, 2018

14:30 Opening

14:35 Invited Talk

Mass Spectrometry Imaging in Clinical Research

Bram Heijs. *Leiden University Medical Center***.** The Netherlands

15:35 Ph. D. Students Oral Presentations

- Novel Concept to Calculate the B2B Tunneling Probability based on an area equivalent WKB approach for a usage in TFET Compact Models, **Fabian Horst**

- Design and control of a bidirectional DC/DCconverter for an electric vehicle application, **Catalina González**

- Simulating the impedance spectroscopy of an hybridperovskite solar cells via time-dependent 1D driftdiffusion model, **Ilario Gelmetti**

16:20 Break and Poster Session

16:40 Invited Talk

Magnetic filaments: a new promising technological field

Joan Josep Cerdà. *Universitat de les Illes Balears*, Spain

Friday June 29th, 2018

9:30 Invited Talk

Smart Surfaces for SERS Detection

María Pilar Pina. *Universidad de Zaragoza,* Spain.

10:30 Ph. D. Students Oral Presentations

- Optical Biosensing based on Nanoporous Anodic Alumina Rugate Filters, **Karen Acosta**

- Assessment of THS exposure effects in liver bymultiplatform metabolomics analysis, **Sonia Torres**

- Bidirectional Isolated Low-Power DC-DC Converter for Balancing of Utility-Scale PV Systems, **Nazmul Hassan**

11:15 Break and Poster Session

11:35 Invited Talk

The new approach to photoelectric properties of the MIS system at near zero photocurrents. Theory and applications

Henryk Przewlocki. *Institute of Electron Technology*, Warsaw

12:35 Ph. D. Students Oral Presentations

-Interferometric real time monitoring of bioconjugation of Streptavidin in Nanoporous Anodic Alumina, **Laura Pol**

-Electropolishing 1100 Aluminum Alloy for Solar Concentrators. **Sara María Aguilar**

-Benzothiadiazole Substituted Semiconductor Molecules for Organic Solar Cells: The Effect of the Solvent Annealing Over the Thin Film Hole Mobility Values. **Cristina Rodriguez**

13:20 Closing and Lunch

Invited Sessions

Mass Spectrometry Imaging in Clinical Research

Bram Heijs
Leiden University Medical Center
The Netherlands

Matrix-assisted laser desorption/ionization mass spectrometry imaging (MALDI-MSI) is an analytical technique that allows the visualization of 100-1000's biomolecules directly from tissue sections. Often applied in clinical research, samples are often limited and precious. Robust and novel methodologies are required to extract as much molecular information from the tissues as possible in order to gain insight in the molecular background of disease. In the presented work, the combination of on-tissue (enzyme) chemistry and high resolution MALDI-MSI is displayed in order to obtain more in-depth access to specific analytes or obtain sequential access to multiple analyte classes from the same tissue section.

Magnetic filaments: a new promising technological field

Joan J. Cerdà[a] , Pedro Sánchez[b] , Daniel Lüsebrink [c] , Sofia Kantovich [b,d] , Elena S. Pyanzina[d] , Ekaterina V. Novak[d] , and Tomàs Sintes[e]

[a] Departament de Fsica UIB i Institut d'Aplicacions Computacionals de Codi Comunitari (IAC3), Campus UIB, 07122 Palma de Mallorca, Spain,
[b] Faculty of Physics, Universität Wien, Boltzmanngasse 5, 1090 Wien, Austria ,
[c] UCB Department of Physics and Astronomy, University of British Columbia, 6224 Agr. RoadVancouver, B.C. V6T 1Z1, Canada,
[d] Ural Federal University, Lenin av. 51, 620000, Ekaterinburg, Russia,
[e] IFISC (UIB-CSIC) Instituto de Física Interdisciplinar y Sistemas Complejos, Campus UIB, 07122 Palma de Mallorca, Spain.

Magnetic filaments [1,2,3,4] or Stockmayer polymers are strings of magnetic nanocolloids linked consecutively to form nano-chains. These polymers exhibit very unusual properties and their structural and rheological properties can be tuned externally via magnetic fields leading to many potential applications. Such applications range from solutions of those polymers used as enhanced ferrofluids till the design of mesoscopic structures known as magnetic brushes [5,6,7], where magnetic polymers are attached by one of their ends to a surface in order to create the responsive structures. Magnetic brushes can be used as actuators as well as filters among many other applications like new revolutionary types of nanochromatographic columns. In this talk we will explore the potential of magnetic filaments and show the results of our preliminary tests aimed to assess the viability of these systems for technological applications.

References

[1] J.J. Cerdà et al., Soft Matter 9 (2013)7185–7195.
[2] J.J. Cerdà et al., Phys.Chem.Chem.Phys. 18 (2016), 12616–12625.
[3] D. Lüsebrink et al., J.Chem. Phys., J. Chem- Phys. 145 (2016) 234902.
[4] D.A. Rozhkov, et al., Molecular Simulation 44 (2018), 507–515.
[5] P.A. Sánchez et al., Faraday Discuss. 186 (2016)241–263.
[6] P.A. Sánchez et al., Macromolecules 48 (2015)7658–7669.
[7] E. Pyanzina et al., Soft Mattter, 13 (2017) 2590–2602.

Smart Surfaces for SERS Detection

María Pilar Pina
Universidad de Zaragoza
Spain

Surface Enhanced Raman Spectroscopy (SERS) is one of the leading techniques for label-free ultrasensitive vibrational fingerprinting of a variety of molecular compounds. Since its discovery in 1974. the field of research is continuously evolving thanks to the advances in bottom up or top-down strategies for the synthesis and fabrication of nanomaterials combined with an increased understanding of their plasmonic properties. In this talk, I will briefly introduce the SERS fundamentals, describe its potential advantages for sensing applications and present its main limitations when dealing with gas/vapor sensing at trace level. Then, I will primarily focus on our main contributions to this topic, with emphasis on: the fabrication/synthesis approaches for metallic nanostructures, and the deployment of either partition layers or more selective coatings over the plasmonic surface for the real time label-free detection of neurotoxic agents in gas phase.

The new approach to photoelectric properties of the MIS system at near zero photocurrents. Theory and applications

Henryk Przewlocki
Institute of Electron Technology, Warsaw
Poland

The energy band diagram is a fundamental property of any semiconductor device. Photoelectric measurements are the most effective methods of nanoelectronic devices band diagram determination. They deserve therefore detailed theoretical analysis and precisely controlled experimental procedures. The theory of photoelectric phenomena taking place in the MIS system which is now commonly accepted and applied agrees quite well with the experimental results for high enough electric fields in the insulator, however it fails at low electric fields (usually for $E<(10^4\text{-}10^5)$ V/cm, i.e. at near zero photocurrent. The failure of the "classical" theory will be demonstrated and our new approach to this problem will be presented. It will be shown that this approach opens up the possibilities of developing new measurement methods of high accuracy.

ENGINYERIA ELECTRÒNICA ELÈCTRICA I AUTOMÀTICA

UNIVERSITAT ROVIRA I VIRGILI

Graduate Students Meeting on Electronics Engineering

Tarragona, Spain. June 28 - 29, 2018

Regular Sessions

Assessment of THS exposure effects in liver by multiplatform metabolomics analysis

Sònia Torres[1], Sara Samino[1], Pere Ràfols[1,2], Neema Adhami[3], Manuela Martins-Green[3], Xavier Correig[1,2], Noelia Ramírez[1,2]

[1] Metabolomics Interdisciplinary Lab, IISPV, DEEEA-Universitat Rovira i Virgili, Tarragona, Spain; [2]CIBERDEM, Spanish Biomedical Research Centre in Diabetes and Associated Metabolic Disorders, Barcelona, Spain; [3]Department of Cell Biology and Neuroscience, University of California, Riverside
sonia.torres@urv.cat; sara.samino@urv.cat; pere.rafols@urv.cat; nadha001@urc.edu; Manuela.martins@ucr.edu; Xavier.correig@urv.cat; Noelia.ramirez@urv.cat

Abstract

Thirdhand smoke (THS) is the accumulation of secondhand smoke gases and particles that become embedded in materials. Inhalation, ingestion and dermal absorption are the main pathways of THS exposure. Although the increasing evidences of THS hazards, the specific cellular and molecular consequences of exposure to THS remain to be fully elucidated. We used a multiplatform metabolomics approach by Mass Spectrometry Imaging (MSI), Nuclear Magnetic Resonance (NMR) and liquid chromatography coupled to high-resolution mass spectrometry (LC-MS), for the characterization of metabolic disorders in liver of mice exposed to THS. We demonstrate that THS exposure results in abundant hepatic triglyceride accumulation, choline deficiency and oxidative stress which lead to Non Alcoholic Fatty Liver Disease (NAFLD).

1. Introduction

Thirdhand tobacco smoke (THS) is a novel and poorly understood pathway of tobacco exposure that is produced by the accumulation of secondhand smoke (SHS) on environmental surfaces that ages with time, becoming progressively more toxic [1]. The health effects of THS exposure have been recently studied using cells[2] and animal models[3][4]. Liver is an essential organ involved in metabolizing many toxins, including drugs, and chemicals. Just one previous study assessed THS hazards on liver [5] revealing that THS leads to increased lipid levels and non-alcoholic fatty liver disease. However, the metabolic pathways implicated in liver disease because of THS exposure are currently unknown. The main objective of this paper is the characterization of the specific metabolic disorders caused in liver beacause of THS exposure. To that end, we present a broad characterization of liver of mice exposed to THS through a multiplatform metabolomics approach by the combination of three different analytical platforms, Mass Spectrometry Imaging (MSI), for the mapping of lipids in control and THS samples, Nuclear Magnetic Resonance (NMR) and liquid chromatography coupled to high-resolution mass spectrometry (LC-MS) for the identification of a wider range of metabolites.

2. Materials and methods

C57BL/6 mice were exposed for 24 weeks to THS, under conditions that mimic exposure of humans in homes of smokers. Liver extracts were analyzed by ^{1}H NMR and UHPLC-MS. The acquired ^{1}H NMR spectra were integrated using the AMIX 3.8 software package (Bruker, GmBH). Several database engines (BBioref AMIX database (Bruker), Chenomx and HMDB [2] were used for 1D-resonances assignment and metabolite identification. The statistical analysis was performed using RStudio (version 3.3.2). FDR-adjusted $p<0.05$ was considered to indicate a statistically significant difference between groups.

LC-MS data was processed by using the XCMS software (version 2.9.2). to detect and align features. Filtered features (minimum intensity and analytical variation) were used for univariate statistical analysis. Features with p-value, FDR corrected < 0.05 and fold change > 1 were putatively identified by searching

against Human Metabolome Data Base (version 3.0) within 5 ppm error threshold. Relevant putatively identified metabolites were used for MS/MS analysis and identification by comparing the obtained experimental mass fragmentation spectra with those found in open access databases (e.g., Human Metabolome Database, METLIN and LipidMaps).

Mass spectrometry images of liver were acquired by laser desorption-ionization MS using sputtered gold nanolayers over the tissue slices. LDI-MS data was processed using the in house developed rMSI and rMSIproc R packages [6]. HMDB 4.0 database was used for identification. Then statistical analysis to compare control and THS samples was done using K-means approach. Identification of some putative identified metabolites were confirmed by UHPLC-MS/MS.

3. Results

Our NMR and UHPLC-MS/MS-based untargeted metabolomic approach revealed more than 95 metabolites dysregulated in liver due to THS exposure. Lipid metabolic profiling unequivocally identified a total of 42 lipids comprising of triglycerides (TG), phosphocholines (PC), lysophosphocholines (LPC), sphingomyelin (SM), cholesterol, coenzyme Q9 and fatty acids. The differential expressions of lipids in response to THS (fold change) revealed that 21 tryglecerids, unsaturated phosphocholines, lysopophoscholines, Docosahexaenoic (DHA), Oleic, Linoleic, monosaturated and polyunsaturated fatty acids are up regulated in THS liver samples. Against, saturated PC, sphingomyelin, free and total cholesterol and Coenzyme Q9 are down regulated in THS samples.

MS images showed lipid accumulation in the form of lipid droplets and increased lipid droplets concentration due to THS-exposure (Figure 1). The abnormal lipid metabolism known as NAFLD was confirmed by the deficiency of Choline and all metabolites related with phosphatidylcholine synthesis. Choline deficiency has an important role in NAFLD, it has been related not only with the deposition of triacylglycerol in liver and reduced phospholipid synthesis [7][8] but also with the expression of genes involved in cell proliferation, differentiation and apoptosis, and with liver dysfunction [9] and cancer.

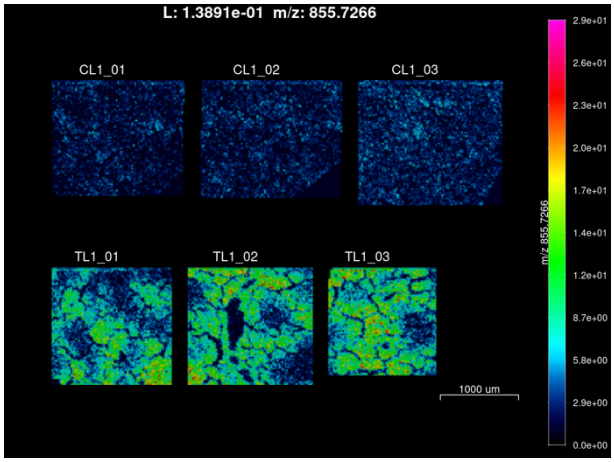

Figure 1. MS images of liver slices that plot the relative abundance of the triglyceride TG(52:4) in control (first row) and THS exposed liver samples (second row).

Pathway analysis showed that 19 metabolites of the dysregulated metabolites were involved in the glutamate, glutathione and nicotine /nicotinamide metabolism pathways, which are related to nucleic acid and protein synthesis among others[10],[11],[12]. Furthermore, the dysregulation of these pathways confirms the oxidative stress nature of THS exposure health effects. Oxidative stress also affects lipid composition. Thus, the overexpression of monounsaturated and polyunsaturated fatty acids as well as that of Polyunsaturated PC found in THS increase the risk of suffering lipid peroxidation, which are product of oxidative stress [13].

5. Conclusions

The multiplatform metabolomic approach presented here allowed an enhanced characterisation of the metabolite disorders in liver of mice exposed to THS. The combination of three different analytical platforms allowed the identification of more than 90 metabolites relevant for the health assessment of THS exposure. NMR provided reliable identifications and quantifications, UHPLC-MS was key for the identification of many dysregulated metabolites and the identification of lipids, whereas MSI allowed us to enrich the biological interpretation by the mapping of lipids in control and THS-exposed livers. Moreover, the identified metabolites can potentially serve as biomarkers for the elucidation of NAFLD and its various stages.

References

[1] P. Jacob *et al.*, "Thirdhand Smoke : New Evidence , Challenges , and Future Directions," 2016.

[2] B. Hang *et al.*, "Thirdhand smoke causes DNA damage in human cells," *Mutagenesis*, vol. 28, no. 4, pp. 381–391, Jul. 2013.

[3] A. N. N, Y. Chen, and M. Martins-Green, “Biomarkers of disease can be detected in mice as early as 4 weeks after initiation of exposure to third-hand smoke levels equivalent to those found in homes of smokers.,” *Clin. Sci.*, vol. 131, no. 19, pp. 2409–2426, 2017.

[4] N. Adhami, S. R. Starck, C. Flores, and M. M. Green, “A health threat to bystanders living in the homes of smokers: How smoke toxins deposited on surfaces can cause insulin resistance,” *PLoS One*, vol. 11, no. 3, pp. 1–19, 2016.

[5] M. Martins-Green *et al.*, “Cigarette smoke toxins deposited on surfaces: Implications for human health,” *PLoS One*, vol. 9, no. 1, pp. 1–12, 2014.

[6] P. Ràfols *et al.*, “RMSI: An R package for MS imaging data handling and visualization,” *Bioinformatics*, vol. 33, no. 15, pp. 2427–2428, 2017.

[7] J. L. Sherriff, C. Properzi, J. Oddo, and L. A. Adams, “Choline , Its Potential Role in Nonalcoholic Fatty Liver Disease , and the Case for Human and Bacterial Genes 1 , 2,” no. 12, pp. 5–13, 2016.

[8] V. Michel, Z. Yuan, S. Ramsubir, and M. Bakovic, “Choline transport for phospholipid synthesis.,” *Exp. Biol. Med. (Maywood).*, vol. 231, no. 5, pp. 490–504, 2006.

[9] Z. Li, L. B. Agellon, and D. E. Vance, “Phosphatidylcholine homeostasis and liver failure,” *J. Biol. Chem.*, vol. 280, no. 45, pp. 37798–37802, 2005.

[10] B. Hang *et al.*, “Adverse health effects of thirdhand smoke: From cell to animal models,” *Int. J. Mol. Sci.*, vol. 18, no. 5, 2017.

[11] S. D. Yelamanchi *et al.*, “A pathway map of glutamate metabolism,” *J. Cell Commun. Signal.*, vol. 10, no. 1, pp. 69–75, 2016.

[12] G. Wu, Y. Fang, S. Yang, J. R. Lupton, and N. D. Turner, “Recent Advances in Nutritional Sciences Glutathione Metabolism and Its Implications for Health 1,” no. December 2003, pp. 489–492, 2018.

[13] A. Reis and C. M. Spickett, “Chemistry of phospholipid oxidation,” *Biochim. Biophys. Acta - Biomembr.*, vol. 1818, no. 10, pp. 2374–2387, 2012.

Benzothiadiazole Substituted Semiconductor Molecules for Organic Solar Cells: The Effect of the Solvent Annealing Over the Thin Film Hole Mobility Values

Cristina Rodríguez-Seco[1], Subhayan Biswas[2], Ganesh D. Sharma*[2], Anton Vidal-Ferran[1,3]*, Emilio Palomares*[1,3].

1. Institute of Chemical Research of Catalonia-The Barcelona Institute of Science and Technology (ICIQ-BIST). Avda. Països Catalans, 16. Tarragona. E-43007. Spain. (+34) 977 920 200. E-mail: cseco@iciq.es, avida@iciq.es, epalomares@iciq.es.
2. Department of Physics, The LNM Institute of Information Technology, Jamdoli, Jaipur 302031, India. (+91)141 518 9211. E-mail: gdsharma273@gmail.com.
3. ICREA. Passeig Lluís Companys, 23. Barcelona, E-08010. Spain.

Abstract

We have synthesized and characterized two low molecular weight organic molecules, namely CS01 and CS03 having the benzo[c][1,2,5]thiadiazole-4,7-diamino core but differing in the number of aromatic rings at the amino groups. The molecules, when processed to make thin organic films, display absorbance up to the near IR region (≈750 nm) and good hole mobility values. Upon mixing each organic semiconductor molecule with the fullerene derivative $PC_{71}BM$ we monitored a strong quenching of the fluorescence emission. We assigned such process to efficient charge transfer from the CS01 and CS03 molecules to the fullerenes. We prepared organic solar cells and obtained, as a first attempt, efficiencies over 2% under 1 sun light simulated solar radiation. Furthermore, the film optimization through solvent annealing process increased further the efficiencies up to 4.80 % for CS01 and 5.12 % for CS03. The observed increase in efficiency is due to a better morphology. However, an analysis in depth reveals that the solvent annealing leaded to a better hole mobility but the electron mobility remains alike.

1. Introduction

Silicon based solar cells are the leading photovoltaic technology but it is desirable to look at other more flexible, low cost, low weight transparent and suitable for roll-to-roll fabrication materials. Organic solar cells (OSCs) based on the solution processed bulk heterojunction (BHJ) consisting of conjugated polymer as donor and fullerene and non-fullerene acceptor meet all these necessities.

OSCs prepared using low molecular weight molecules are attracting interest due to their small losses in Voc in comparison with other organic semiconductor materials[5], like the polymers. However, the so called "*small molecules (SMs)"* have the advantage of not being dependent on regionregularity issues, differences in molecular weight and the difficult purification processes to clean the catalysts[6]. Moreover, their synthesis has a few steps and it is easy to scale up. To achieve efficient light harvesting, it is also desirable that the SMs extend their absorbance as far as in the IR as possible[7]. The state of the art of OSCs based on SMs had made great strides with PCE more than 11 % based on fullerene derivatives as acceptors[9], which is comparable to the polymer counterpart.

Benzo[*c*][1,2,5]thiadiazole-based molecules have been used recently to prepare OSCs[10-12]. We report the synthesis, photophysical and electrochemical properties of two novel benzo[*c*][1,2,5]thiadiazole derivatives (**Scheme 1**). The electrochemical measurements indicate that these SMs are suitable as donor along with $PC_{71}BM$ ([6,6]-phenyl C_{71} butyric acid methyl ester) as acceptor for the solution processed BHJ OSCs. After the optimization of the active layer, the OSCs based on **CS01** and **CS03** exhibit overall PCEs of to 4.80 % and 5.12 %, respectively. The higher value for **CS03** is attributed to the denser π-π stacking distance, more crystalline, beneficial for better hole transport and

broader absorption spectra of **CS03**:$PC_{71}BM$ active layer.

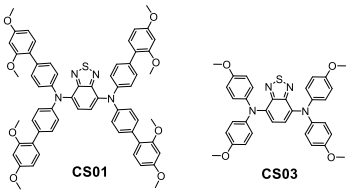

Scheme 1 Chemical structures of **CS01** and **CS03.**

2. RESULTS AND DISCUSSION.

2.1 Absorption and PL emission spectra

The absorbance of **CS01** and **CS03** in solution ($1x10^{-5}$ M) and in thin film (thickness 80 nm) processed from chloroform solution are shown in **Figure 1(a)**. The absorption spectra of **CS01** and **CS03** in solution show a panchromatic absorption from 350 nm to 650 nm and 700 nm, respectively. Moreover, an important red shift of the main absorption band with a noticeable shoulder can be monitored when the molecules are deposited in thin films attributed to the strong interactions may be originated from the ordered SM π-π packing[13], due to the formation of J-type aggregates in the solid state. In fact, for the **CS03** the formation of J-aggregates seems favored and a higher bathochromic shift is observed. The optical gap (E_{gap}^{opt}) was calculated from the onset of the absorption wavelength (λ_{onset}) in the thin films using $E_{gap}^{opt}=1240/\lambda_{onset}$, with values of 1.72 eV and 1.65 eV for **CS01** and **CS03**, respectively.

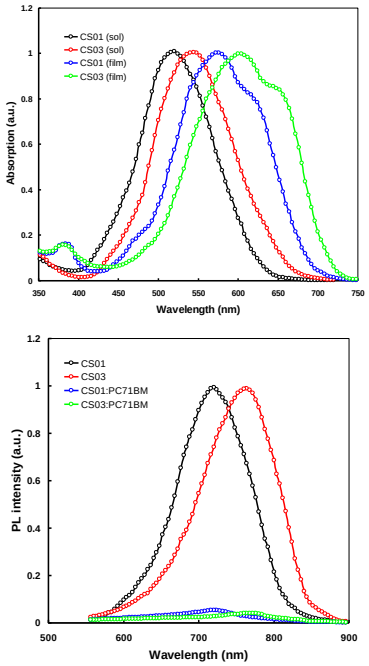

Figure 1 (a) Normalized absorption spectra of **CS01** and **CS03** in chloroform solution and thin films. (b) Fluorescence emission spectra for **CS01** and **CS03** and the **CS01**:$PC_{71}BM$ and **CS03**:$PC_{71}BM$ thin films upon excitation at λ_{ex}=530 nm for **CS01** and λ_{ex}= 540 nm for **CS03**.

Figure 1(b) illustrates the PL spectra. When the organic thin films contain the fullerene derivative $PC_{71}BM$ in a ratio 1:2 the **CS01** and **CS03** fluorescence is totally quenched. This indicates efficient electron transfer from the **CS01** and **CS03** excited state to the fullerene and it is a first indication that both **CS01** and **CS03** can be used in BHJ thin films, together with the $PC_{71}BM$, in OSCs.

2.2 Electrochemical properties and relative energy levels.

The electrochemical properties of **CS01** and **CS03** were analyzed using cyclic voltammetry (CV). **Figure 2** shows the cyclic voltammograms. Both compounds show a first reversible oxidation wave at 0.22V for **CS01** and 0.03V for **CS03** versus Fc/Fc^+. From those values, the relative HOMO energy level for **CS01** and **CS03** was calculated: -5.32 eV and -5.13 eV by applying **Equation 1**, respectively. The deeper value for the **CS01** HOMO should lead to higher V_{OC} in the solar cells compared to the **CS03**. The relative LUMO energy values are -3.6 eV for **CS01** and -3.48 eV for **CS03** as calculated using **Equation 2**.
The experimental results show good correlation with the theoretical values with the HOMO energy value for **CS01** being deeper than the HOMO energy value of **CS03**.

Equation 1 E_{HOMO} (eV) = [-q(Eox+5,1)]eV

, where *q* is the electron charge, Eox is the oxidation potential of the first wave of the molecule measured using Fc/Fc^+ as reference.

Equation 2 E_{LUMO} (eV) = Eg^{opt}- E_{HOMO}

Figure 2 Cyclic voltammograms for **CS01** (a) and **CS03** (b) using ferrocene (Fc/Fc^+) as internal reference in dichloromethane measured at room temperature.

2.3 Photovoltaic measurements

OSCs were fabricated with the following device structure ITO/PEDOT:PSS/**CS01** or **CS03**:$PC_{71}BM$/ PFN/Al. We have optimized the performance of OSCs through varying the D:A weight ratios in $CHCl_3$ solution. The optimized weight ratio is 1:2 for both the **CS01** and the **CS03**. The current-voltage (J-V) curves

under illumination for the devices are shown in **Figure 3a** and photovoltaic parameters are listed in **Table 1**. As commented before, the higher V_{OC} observed for **CS01** is due to the deeper relative HOMO energy value in comparison with the **CS03**. As demonstrated previously, for equal recombination kinetics the V_{OC} of the organic solar cells can be correlated with the energy difference between the HOMO of the electron donor molecule and the LUMO energy level of the electron acceptor molecule. The differences in J_{SC} can be understood in terms of better light harvesting in the case of the **CS03** thin films as already observed in **Figure 1a**. Nonetheless, to reinforce our hypothesis we measured the incident photon to current conversion efficiency (IPCE) spectra for the OSCs (**Figure 3b**) which is in perfect agreement with the absorption data. Moreover, the integration of the IPCE spectrum with respect to the 1.5 AM G sun spectra leads to values of J_{SC} very close (**Table 1**).

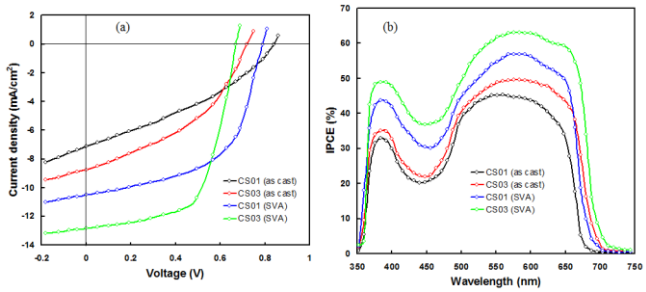

Figure 3 (a) Photocurrent –voltage characteristics under 1 sun simulated illumination and (b) IPCE spectra of the organic solar cells based on **CS01** and **CS03** as donor and $PC_{71}BM$ as acceptor.

Table 1. Photovoltaic parameters (J_{SC} (photocurrent density), V_{OC} (open Circuit Voltage), FF (fill factor), PCE (solar cell efficiency at 1 sun) for the different solar cells using **CS01** and **CS03** as donor and $PC_{71}BM$ as acceptor.

	J_{SC} (mA/cm^2)	V_{OC} (V)	FF	PCE (%)	J_{SC} (mA/cm^2)[b]
CS01 (as cast)	7.13	0.84	0.34	2.03	7.01
CS03 (as cast)	8.61	0.73	0.38	2.39	8.49
CS01 (SVA)	10.48	0.79	0.58	4.80	10.37
CS03 (SVA)	12.81	0.67	0.62	5.32	12.73

[b] Calculated after the integration of IPCE spectra with respect to the 1.5 AM G solar spectrum.

The **CS01** and **CS03** based OSCs without any treatment showed low PCEs mainly due to the low values of both J_{SC} and FF and may be due to poor nanoscale morphology of the active layer which lead to charge recombination during their transportation towards electrodes. In order to improve the morphology of the active layer, we have adopted the solvent vapor annealing (SVA) as reported in literature[14]. We have used CS_2 for SVA treatment during 30 s due to its high vapour pressure and the solubility the SMs have with it Moreover, $PC_{71}BM$ exhibits better solubility in CS_2 as compared to other solvent such as tetrahydrofuran. Therefore, the combination of high vapour pressure and medium solubility of the small molecule donor implies fast vapour penetration in the active layer. The current-voltage characteristics of the OSCs based on SVA treated active layer are shown in **Figure 3a** are listed in **Table 1**. The photovoltaic performance of the OSCs has been significantly enhanced compared to as cast OSCs. Since the SVA treatment the crystallite of donor materials are grown, this treatment for longer time, would make an over grown of the crystallite (> exciton diffusion length) and as large as the film thickness and the active layer no longer form the BHJ networks.

The increase in the J_{SC} for the OSCs after the SVA treatment has been also confirmed from the IPCE spectra of devices (**Figure 3b**). Those values are higher than those for the as cast counterparts, indicating that the exciton generation and their dissociation into free charge carriers have been improved, related to the improved nanoscale morphology and phase separation.

The hole mobility of **CS01** and **CS03** in the blend films were measured by the J-V characteristics on the hole only devices (**Figure 4**). The hole mobility values for as cast and SVA treated active layers are summarized in **Table 2**. The electron mobility in the as cast and SVA treated active layers were measured using electron only devices in similar manner as for hole mobility and complied in **Table 2**. There is a slight change in the electron mobility values after the SVA treatment. The improved hole mobility and better balance between the electrons and holes mobility after the SVA treatment could promote charge transport and reduced charge recombination, leading to improvement in J_{SC} and FF, and thereby PCE. Moreover, the hole mobility in **CS03**:$PC_{71}BM$ is higher than that of **CS01**:$PC_{71}BM$ for as cast and SVA processing conditions, respectively irrespective of processing conditions, may be one the reasons for high values of FF and PCE for former OSCs.

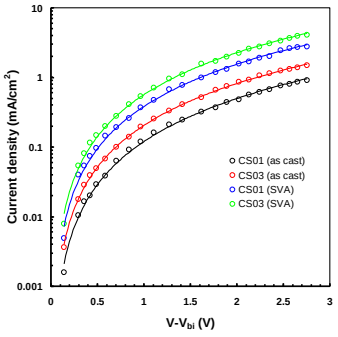

Figure 4. (a) Current-voltage characteristics of hole-only devices based on **CS01**:$PC_{71}BM$ and **CS03**:$PC_{71}BM$ photoactive thin films.

Table 2. Solar cells carriers mobility measured using the Space Charge Limited Current (SCLC) model.

Active layer	Hole mobility (cm^2/Vs)	Electron mobility (cm^2/Vs)	Ratio
CS01:$PC_{71}BM$ (as cast)	2.56×10^{-5}	2.13×10^{-4}	8.32
CS03:$PC_{71}BM$ (as cast)	4.19×10^{-5}	2.28×10^{-4}	5.44
CS01:$PC_{71}BM$ (SVA)	7.89×10^{-5}	2.42×10^{-4}	3.06
CS03:$PC_{71}BM$ (SVA)	9.87×10^{-5}	2.48×10^{-4}	2.51

3. Conclusions

In summary, we have synthesized two new low weight organic molecules that can be processed to form semiconductor organic thin films. The molecules show excellent absorption from the visible to the near IR region of the sun spectra and interfacial electron transfer process when mixed in thin BHJ films with $PC_{71}BM$. The optimization through SVA of the photoactive films in solar cells with the standard configuration ITO/PEDOT:PSS/Photoactive film/PFN/Al leads to efficiencies of 4.80 % and 5.1 for **CS01** and **CS03**, respectively. However, a deeper analysis of the photovoltaic parameters leads to the finding that the SVA processing implies the formation of an unbalanced process between holes and electrons mobility. While the hole mobility property of the thin BHJ film improves noticeably, the electron mobility characteristics remains almost identical indicating the improved balanced charge transport. Nevertheless, the solvent annealing has positive effects on the film morphology that leads to better charge collection as measured by monitoring the changes in J_{ph} *vs.* V_{eff} leading to higher solar-to-energy conversion efficiencies over 5 % in the case of the **CS03** molecule. These SMs can be used as donor with the low bandgap non-fullerene acceptors and we are working in this direction.

References

[1] Espinosa, N.; Hosel, M.; Angmo, D.; Krebs, F. C., Solar Cells with One-Day Energy Payback for the Factories of the Future. *Energy & Environmental Science* **2012**, *5*, 5117-5132.

[2] Liu, C.; Wang, K.; Gong, X.; Heeger, A. J., Low Bandgap Semiconducting Polymers for Polymeric Photovoltaics. *Chemical Society Reviews* **2016**, *45*, 4825-4846.

[3] Li, G.; Zhu, R.; Yang, Y., Polymer Solar Cells. *Nature Photonics* **2012**, *6*, 153.

[4] Lu, L.; Zheng, T.; Wu, Q.; Schneider, A. M.; Zhao, D.; Yu, L., Recent Advances in Bulk Heterojunction Polymer Solar Cells. Chemical Reviews 2015, 115, 12666-12731.

[5] Tuladhar, S. M., et al., Low Open-Circuit Voltage Loss in Solution-Processed Small-Molecule Organic Solar Cells. *ACS Energy Letters* **2016**, *1*, 302-308.

[6] Ku, J.; Song, S.; Park, S. H.; Lee, K.; Suh, H.; Lansac, Y.; Jang, Y. H., Palladium-Assisted Reaction of 2,2-Dialkylbenzimidazole and Its Implication on Organic Solar Cell Performances. *The Journal of Physical Chemistry C* **2015**, *119*, 14063-14075.

[7] Varotto, A.; Nam, C.-Y.; Radivojevic, I.; P. C. Tomé, J.; Cavaleiro, J. A. S.; Black, C. T.; Drain, C. M., Phthalocyanine Blends Improve Bulk Heterojunction Solar Cells. *Journal of the American Chemical Society* **2010**, *132*, 2552-2554.

[8-9] Wu, R.; Yin, L.; Li, Y., P-Linkage Effect of Push-Pull-Structure Organic Small Molecules for Photovoltaic Application. *Sci. China Mater.* **2016**, *59*, 371-388. Collins, S. D.; Ran, N. A.; Heiber, M. C.; Nguyen, T.-Q., Small Is Powerful: Recent Progress in Solution-Processed Small Molecule Solar Cells. *Advanced Energy Materials* **2017**, *7*, 1602242-n/a.

[10-12] Mohammad, L.; Chen, Q.; Mitul, A.; Sun, J.; Khatiwada, D.; Vaagensmith, B.; Zhang, C.; Li, J.; Qiao, Q., Improved Performance for Inverted Organic Photovoltaics Via Spacer between Benzodithiophene and Benzothiazole in Polymers. *The Journal of Physical Chemistry C* **2015**, *119*, 18992-19000. Zeng, J.; Zhang, T.; Zang, X.; Kuang, D.; Meier, H.; Cao, D., D-a-P-a Organic Sensitizers Containing a Benzothialzole Moiety as an Additional Acceptor for Use in Solar Cells. *Sci. China. Mater.* **2013**, *56*, 505-513. Ku, J.; Lansac, Y.; Jang, Y. H., Time-Dependent Density Functional Theory Study on Benzothiadiazole-Based Low-Band-Gap Fused-Ring Copolymers for Organic Solar Cell Applications. *The Journal of Physical Chemistry C* **2011**, *115*, 21508-21516.

[13] Badgujar, S.; Lee, G.-Y.; Park, T.; Song, C. E.; Park, S.; Oh, S.; Shin, W. S.; Moon, S.-J.; Lee, J.-C.; Lee, S. K., Organic Solar Cells: High-Performance Small Molecule Via Tailoring Intermolecular Interactions and Its Application in Large-Area Organic Photovoltaic Modules (Adv. Energy Mater. 12/2016). *Advanced Energy Materials* **2016**, *6*, n/a-n/a.

[14] Wang, J.-L.; Wu, Z.; Miao, J.-S.; Liu, K.-K.; Chang, Z.-F.; Zhang, R.-B.; Wu, H.-B.; Cao, Y., Solution-Processed Diketopyrrolopyrrole-Containing Small-Molecule Organic Solar Cells with 7.0% Efficiency: In-Depth Investigation on the Effects of Structure Modification and Solvent Vapor Annealing. *Chemistry of Materials* **2015**, *27*, 4338-4348.

Interferometric real time monitoring of bioconjugation of Streptavidin in Nanoporous Anodic Alumina

L. Pol, L.K. Acosta, E. Xifre-Perez J. Ferré-Borrull, L.F. Marsal

Departament d'Enginyeria Electrònica, Elèctrica i Automàtica, Universitat Rovira i Virgili, Països Catalans 26, 43007, Tarragona, Spain
Lluis.marsal@urv.cat

Abstract

Sequential attachment of streptavidin and biotin to nanoporous anodic alumina (NAA) inner pore surfaces is a key step in the design of biosensing systems based on such structure. In this work we study by means of reflection interference spectroscopy (RIfS) the attachment of these two molecules to NAA functionalized with 3-aminopropyltriethoxysilane (APTES) and we evaluate how RIfS signal depends of different biotin concentrations.

1. Introduction

Nanoporous anodic alumina is a material with growing interest in nanotechnology since it consists on an array of regularly ordered straight pores perpendicular to the material surface [1] obtained by the electrochemical anodization of aluminum in the appropriate conditions [2]. Thanks to its high surface-to-volume ratio, tailorable geometry and chemical stability NAA is widely used as a biosensing platform [3]. For this propose the surface modification of NAA by grafting functional molecules is a key step. The streptavidin-biotin interaction system is widely used in biosensors [4]. Thanks to their strong affinity and specificity, it is easy to immobilize any biotinylated molecule on a biosensor surface previously functionalized with and provide sensitivity for a great variety of analytes [5].

Optical biosensing with NAA has been demonstrated with the Reflection Interference Spectroscopy method [6]: the atachment of a specific chemical or biological molecule to the inner pore surface (conveniently modified) of a NAA thin film is detected by a change in the reflectance spectrum, quantified as a shift in the film effective optical thickness (EOT). In this work, we study the successive attachment of streptavidin and biotin to the NAA inner pore surfaces, adequately functionalized, by means of RIfS. The data on the detectability of these grafting steps is a key knowledge to understand the results in successive biosensing experiments.

2. Experimental

NAA thin films were obtained following the two-step anodization process [6] using a 0.3 M oxalic acid electrolyte at an anodization potential of 40 V and at 4 ºC in both anodization steps. Anodization time of the second step was adjusted to obtain a pore length of 5 µm. Figure 1 shows a top-view SEM picture of one of the NAA thin films obtained with such procedure. NAA were then immersed in 5% w/w H_3PO_4 for 10 min to adjust the pore diameter to 50 nm. Finally, 5 nm thickness gold film of was deposited by sputtering on top of the NAA to increase contrast in the measured spectra.

Functionalization of the NAA started by immersing during 1h in boiling hydroxyperoxide (H_2O_2) to obtain hydroxyl (-OH) groups on the surface. Next, samples were incubated (under nitrogen flux) for 1h in 20µl of dry toluene and with 0.2µl of APTES added dropwise, followed by rinsing with toluene and ethanol and storage in oven overnight. Prior to flow cell experiments, streptavidin was mixed with EDC and NHS both at 8mg/ml for 30 min so as to activate the carboxyl group.

To carry out the RIfS experiments NAA samples were mounted on a flow cell. In all steps, the different solutions were circulated until a stable value of EOT was achieved. First step consisted of buffer injection followed by the circulation of the streptavidin (previously incubated with EDC-NHS) at 100 µg/ml. After this step, buffer was injected to wash the non-bounded streptavidin. Finally, biotin at different concentrations (25 µg/ml, 50 µg/ml and 100 µg/ml) was circulated to study the influence of biotin concentration.

To prove the god attachment of a biotinylated molecule to the streptavidin we use biotinylated thrombin after the injection of streptavidin. In this case the injection was followed by the circulation of streptavidin at 50 µg/ml, then buffer was injected to wash the non-binding streptavidin molecules and finally biotinylated thrombin was injected at 20 µg/ml.

2. Results

Figures 2 and 4 shows the results of the flow cell experiments. The graphs show the relative change of EOT as a function of the experiment time. In the figure 2, as a reference, the 0% change corresponds to the stable level after the first PBS injection, while a 100% change corresponds to the variation of EOT after the streptavidin circulation. Figures 2 a b and c correspond to 25 µg/ml, 50 µg/ml and 100 µg/ml biotin concentrations respectively. In all the experiments, the injection of streptavidin is clearly detected by the RIfS method with a rapid increase in EOT as the injection begins and stabilization after 300 s. The circulation of the PBS buffer results in a reduction of the EOT indicating the washing of the non-linked streptavidin molecules.

Figure 4 shows the result when we inject biotinylated thrombin after the streptavidin, in this case we observe an increase of 5nm in EOT which reminds after injection of PBS.

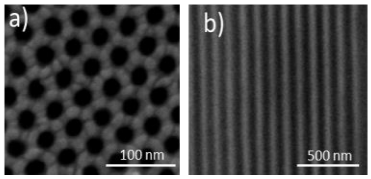

Figure1: SEM pictures of the nanoporous anodic alumina samples a) Top view and b) cross-section.

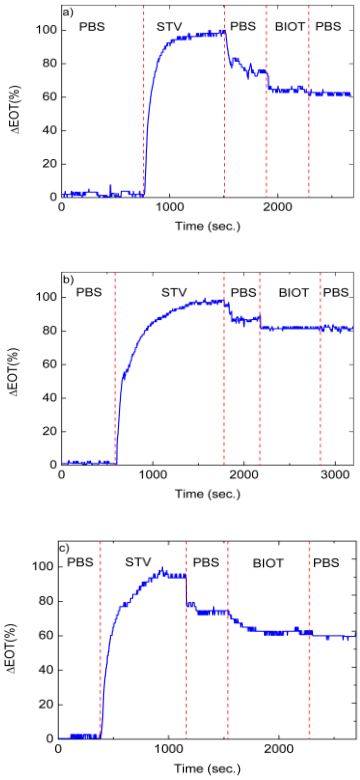

Figure 2: Relative EOT change as a function of time in flow cell with injections of streptavidin (STV) at 100 µg/ml and biotin (BIOT) at a)25µg/ml, b)50 µg/ml, and c)100 µg/ml

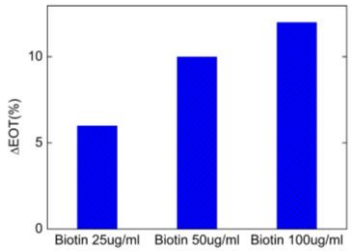

Figure 3: Relative EOT change after injection of biotin and stabilization in consecutively increased concentrations (25, 50 and 100 µg/ml).

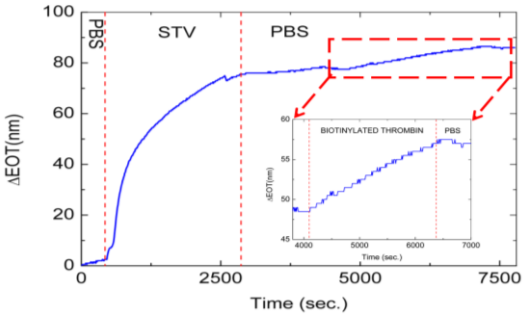

Figure 4: Relative EOT change as a function of time in flow cell with injections of streptavidin (STV) at 50 µg/ml and 20µg/ml biotnylated thrombin.

7. Conclusions

The capability NAA-based sensing of streptavidin-biotin attachment with RIfS has been demonstrated.

Attachment of streptavidin, previously activated with EDC/HNS cross-linker, to the APTES is clearly shown in the RIfS experiments as an EOT increase. Instead, a decrease in EOT after the circulation of biotin is observed. Furthermore, EOT decrease is bigger for higher biotin concentration.

Moreover, we prove the good attachment of biotinylated thrombin to the NAA through streptavidin, this suggest that we can attach any biotinylated molecule to the surface of alumina for biosensors design.

Acknowledgments

This work was supported in part by the Spanish Ministry of Economy and Competitiveness TEC2015-71324-R (MINECO/FEDER), the Catalan authority AGAUR 2017 SGR 1527, and ICREA under the ICREA Academia Award

References

[1] L. Vojkuvka, et al., *Superlattices and Microstructures*, **2008**, 44 (4), 577-582.

[2] A. Santos, et al., *Journal of Electroanalytical Chemistry*, **2011**, 655 (1), 73-78.

[3] G. Macias, et al., *The Analyst*, **2015**, 140 (14), 4848-4854.

[4] Z. Lin, et al., *Talanta*, **2008**, 75, 965–972

[5] T. Kumeria, et al., *Biosensors and Bioelectronics*, **2012**, 35, 167–173.

[6] J. Ferre-Borrull, et al., Optical properties of nanoporous anodic alumina and derived applications. In: D. Losic, A. Santos editors. Nanoporous Alumina. Fabrication, Structure, Properties and Applications, Springer Series in Materials Science, **2015,** 219, 185-217.

Optical Biosensing based on Nanoporous Anodic Alumina Rugate Filters

Laura K. Acosta, Elisabet Xifre-Perez, Josep Ferré-Borrull and Lluis F. Marsal*

*Departament d'Enginyeria Electrònica, Elèctrica i Automàtica, Universitat Rovira i Virgili, Avinguda Països Catalans 26, 43007 Tarragona, Spain. *Corresponding author e-mail address: lluis.marsal@urv.cat*

Abstract

Rugate filters based on nanoporous anodic alumina are nanostructures are obtained by electrochemical anodization of aluminium in the appropriate conditions and by means of continuously varying anodization current. In this work we show the design and fabrication of rugate filters using successive sinusoidal components in the anodization and study its capabilities in biosensing.

1. Introduction

Rugate filters with continuous variation of the refractive index with depth are one-dimensional photonic crystals with tunable stop bands. They present an interesting optical response characterized by a narrow and high reflectance band [1-2]. Nanoporous Anodic Alumina (NAA) is a very suitable material for the formation of variable refractive index structures because of its cost-effective and highly controlled fabrication process [3]. NAA consists of a network of self-arranged pores perpendicular to the surface in an aluminum oxide matrix. This nanomaterial presents an exceptionally high effective surface area (hundreds of m^2/cm^3), very useful for applications like optical biosensing and drug delivery platforms [4-7].

In this work, we design and fabricate Rugate filters with complex optical response based on NAA (RF-NAA) with photonic peaks in the UV and VIS spectral range. They are formed by stacking together three periodic structures tuned at different wavelengths. These RF-NAA are used for developing a sensing system with real time monitoring for the detection of biological elements. D-Glucose solutions with different concentrations are used to evaluate the sensitivity of this complex optical structure.

2. Materials and Methods

Materials

High purity Aluminium foils (thickness 0.5 mm and purity 99.99%), Ethanol (C_2H_5OH), perchloric acid ($HClO_4$), oxalic acid ($H_2C_2O_4$), hydrochloric acid (HCl), copper chloride (CuCl) and D-glucose ($C_6H_{12}O_6$) were purchased from Sigma-Aldrich. Double deionized water (DI) (18.6 MΩ) was used for all the solutions unless other specified.

Fabrication

First Al substrates were degreased in acetone, cleaned with ethanol and DI water and finally dried under steam of air. Before the anodization, Al substrates were electropolished in a mixture of Ethanol and Perchloric acid 4:1 at 20 V and 5ºC for 5 min. During the electropolishing step the stirring direction was alternated every 60 s. After the electropolishing the samples were cleaned with ethanol and DI water and dried under steam of air [4]. Then, the anodization was carried out in $H_2C_2O_4$ 0.3 M at 5ºC applying a sinusoidal current profile with several design parameters like offset current (I0), amplitude current (I1), Period (T) and number of periods (N). Multiple periodic currents are applied sequentially instead of simultaneously. In this case, the different rugate filters are stacked on the same structure. This permits to use a bigger current contrast in the current variations and using electrolytes with different composition. Figure 1 shows the sinusoidal current profile and involved parameters during the fabrication.

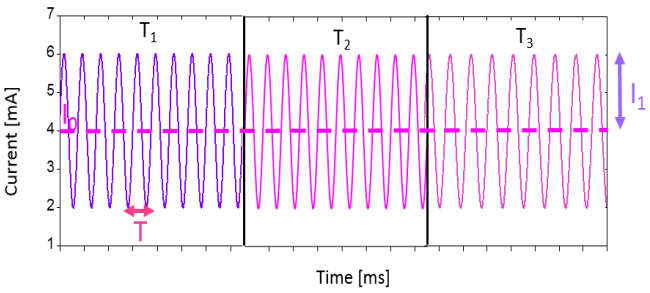

Figure 1. Current profile in stack configuration of Rugate Filters based on nanoporous and alumina and involved fabrication parameters.

3. Results

Figure 2 shows the reflectance spectrum of the described sample after removing the remaining aluminum. As it can be seen, the three successive sinusoidal currents give rise to the formation of three stop bands. The height of these stop bands reaches between 25 % and 52 % while its widths are between 20

nm and 30 nm. It can be observed that there is a direct relationship between the period of the anodization current and the corresponding central wavelength, λ_1 = 516 nm of T_1 = 160 s, λ_2 = 606 nm of T_2 = 175 s, λ_3 = 694 nm of T_3 = 195 s.

The ability to detect a change in refractive index of the medium filling the pores has been investigated by real-time spectroscopy. To this end, the sample is mounted in a sealed cell with a transparent window that permits the measurement of the reflectance spectrum by a fiber mini spectrometer as different fluids are injected to the cell and fill the staked structure NAA pores. Figure 3 shows s a plot of the peak wavelength for each stop band in the sample as a function of time, as different glucose solutions of increasing concentration are injected. It can be seen that the peak wavelength shifts linearly towards higher values for increasing glucose concentrations, with a lower limit of detection.

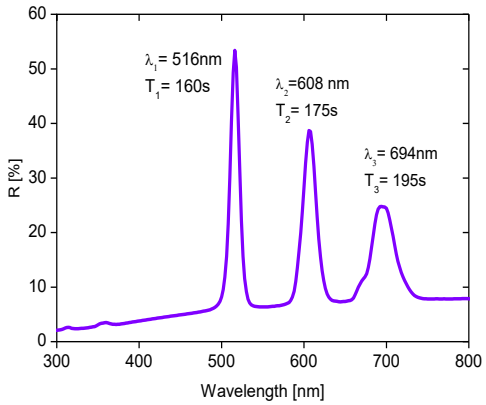

Figure 2. Reflectance spectra of Nanoporous Anodic Alumina Rugate Structures samples with different period time (T) in stack configurartion

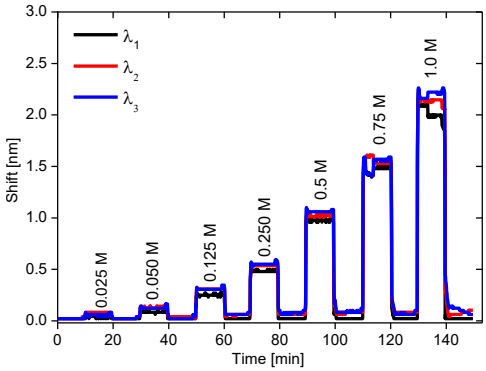

Figure 3. Peak wavelength shift as a function of time for the three photonic stop bands of the stacked structure, as glucose solutions with the indicated concentration are injected in the flow cell.

4. Conclusions

In this work we demonstrate the possibility to fabricate Rugate filters based in Nanoporous Anodic Alumina in stack configuration by the application of successive sinusoidal anodization currents with different period. The central wavelength of the obtained photonic stop bands is directly related with the period of each of the different applied successive sinusoidal currents. Further research will be carried out to determine the relation between these two magnitudes. We also demonstrated the ability of these structures to detect a change in the refractive index of the fluid filling the pores by means of real-time spectroscopy.

Acknowledgements

This work was supported in part by the Spanish Ministry of Economy and Competitiveness TEC2015-71324-R (MINECO/FEDER), the Catalan authority AGAUR 2017 SGR 1527, and ICREA under the ICREA Academia Award

References

[1] J. Ferre-Borrull, E. Xifre-Perez, J. Pallares, L.F. Marsal. Optical properties of nanoporous anodic alumina and derived applications. In: D. Losic, A. Santos editors. Nanoporous Alumina. Fabrication, Structure, Properties and Applications, Springer Series in Materials Science Vol. 219 (2015) p. 185-217.

[2] M.M. Rahman, L.F. Marsal, J. Pallarès, J. Ferré-Borrull, *ACS Appl. Mat. Interfaces*, 2013, *5*, 13375-13381.

[3] T. Kumeria, A. Santos, M.M. Rahman, J. Ferré-Borrull, L.F. Marsal, D. Losic, *ACS Photonics*, 2014, *1*, 1298-1306

[4] G. Macias, L.P. Hernández-Eguía, J. Ferré-Borrull, J. Pallares, L.F. Marsal, ACS Appl. Mater. Interfaces, **5** (2013) 8093.

[5] J. Ferré-Borrull, J. Pallarès, G. Macias, L.F. Marsal, Materials, 2014, 7, 5225-5253.

[6] G. Macias, J. Ferré-Borrull, J. Pallares, L.F. Marsal, Nanoscale research letters, 9 (2014) p. 315

[7] A. Santos, J.H. Yoo, C. Vashisth, T. Kumeria, Y. Wang, D. Losic, Nanoscale, 8 (2016) 1360.

Polymer Solar Cells Made From Azafullerene Acceptors

Michael Bothe[a], **María Pilar Montero-Rama[b]**, Aurélien Viterisi[b], Werther Cambarau[c], Caterina Stenta[b], Emilio Palomares[c], Lluis F. Marsal[b,*], Max von Delius[a,*].

[a] Institute of Organic Chemistry and Advanced Materials, University of Ulm, Albert-Einstein-Allee 11, 89081 Ulm, Germany.
[b] Departament d'Enginyeria Electrònica, Elèctrica i Automàtica. Universitat rovira I Virgili, Av. Països Catalans 26, Tarragona, Spain.
[c] Institute of Chemical Research of Catalonia (ICIQ), Avda. Països Catalans 16, 43007 Tarragona, Spain

* indicates the corresponding authors.
max.vondelius@uni-ulm.de
lluis.marsal@urv.cat

Abstract

Herein we describe a library of four azafullerene (AF) monoadducts (DPS-$C_{59}N$, HDP-$C_{59}N$, DBOP$C_{59}N$ and DHOP-$C_{59}N$) used as acceptor materials in PSCs in conjunction with PTB7.

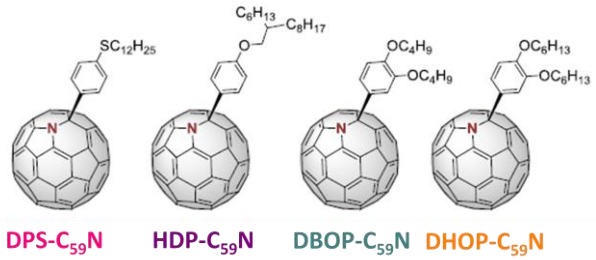

Figure 1: Structure of azafullerenes.

1. Introduction

Polymer solar cell (PSCs) have attracted great interest in the field of renewable energy due to their recent increase in power conversion efficiency and low manufacturing costs. Since the early days of PSCs, a great number of electron donor materials have been reported, however very few alternatives to PCBM fullerenes have been reported to date. Recently, Azafullerenes have been considered as a promising alternative acceptor material due to their stronger absorption in the visible region of the solar spectrum compared to $PC_{60}BM$, without affecting the frontier orbital energies.

2. Experimental and Results

Fabrication of solar cells: The hole transport material (PEDOT:PSS) was spin-coated on the top of the pre-patterned ITO surface, yielding a film thickness of *ca.* 30 nm. The PTB7/AF (donor/acceptor) blend solutions were prepared from a 1:1 or 2:3 D/A weight ratio in Chloroform (10 mg/mL total weight concentration) with 3 or 1 % w/w of DIO additive. The blend solution were deposited by spin coating at 1300 rpm, for 30 s on top of the ITO/PEDOT:PSS surface. After spin-coating, the samples were placed in a thermal evaporator and a Ca layer (20 nm) and an Ag layer (100 nm) were deposited under high vacuum ($1x10^{-6}$ mbar). The active area of the devices were 0.09 cm^2.

Solar cells characterization: The *J-V* characteristics of the devices were recorded using a Sun 2000 solar simulator (150W, ABET Technologies). The illumination intensity was measured to be 100 mW/cm^2 with a calibrated silicon photodiode (NREL). The results are summarized in the table 1 for each fullerene, and the *J-V* characteristics of the best performing devices plotted in Figure 2.

	DPS$C_{59}N$	**HDP$C_{59}N$**	**DBOP$C_{59}N$**	**DHOP$C_{59}N$**
J_{SC} [mAcm^{-2}]^a	8.43	0.92	2.40	0.55
V_{OC} [V]	0.728	0.655	0.666	0.632
FF [%]	49	28	32	25
PCE [%]	3.03	0.19	0.55	0.09
D/A ratio	2:3	2:3	1:1	1:1
DIO [%]	2	2	3	3

Table 1: [a] Values of best-performing devices measured at 1 SUN A.M. 1.5 illumination (100 mW cm^{-2}). Solvent: $CHCl_3$. PCE: power conversion efficiency. D/A: donor/acceptor. DIO: 1,8-Diiodooctane.

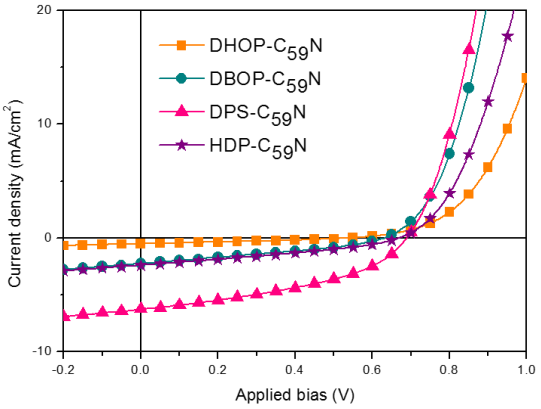

Figure 2: J-V characteristics of best-performing devices.

3. Conclusions

We observed that all azafullerenes, except DPS-C59N, show rather deteriorated J-V characteristics. Our studies indicate that thiophenol-functionalized azafullerenes substituted with single n-alkyl chains lead to favorable J-V characteristics. Although it can be difficult to draw clear structure–property relationships in OPV, we deduced from our studies that two- fold n-alkyl-substituted and branched-alkyl-substituted derivatives lead to poorer characteristics. Further studies on azafullerene-based OSCs should therefore focus on single n-alkyl chain functionalization. [1]

4. Acknowledgment

This work was supported by the Spanish Ministry of Economy, Industry and Competitiveness (MEIC) for grant numbers, TEC2015-71915-REDT and TEC2015-71324-R (MINECO/FEDER), by the ICREA for the ICREA Academia Award and by the Catalan authority for project AGAUR 2017 SGR 1527, and the Deutsche Forschungsgemeinschaft (DFG) (SFB 953, ‘Synthetic Carbon Allotropes’), the Daimler und Benz Stiftung (grant no. 32-12/13).

5. References

[1] M. Bothe, *et.al.* Synthesis, 50 (2018) A-H.

Gold-coated Black Silicon: An Efficient Substrate for Laser Desorption Ionization Mass Spectrometry Applications

Ștefania-Alexandra Iakab[1], Pere Rafols[1,2], Xavier Correig[1,2]

[1] Rovira i Virgili University, Department of Electrical Electronic Engineering and Automation, Avinguda Països Catalans 26, 43007 Tarragona, Spain
[2] Spanish Biomedical Research Centre in Diabetes and Associated Metabolic Disorders (CIBERDEM), C/ Monforte de Lemos 3-5, 28029 Madrid, Spain
Contact: stefania-alexandra.iakab@urv.cat tel: 977256570

Abstract

Mass spectrometry imaging is a label-free analytical technique capable of molecularly characterizing biological samples, including tissues and cell lines. The organic matrices used in matrix-assisted laser desorption/ionization mass spectrometry experiments hampers the analysis of low molecular weight compounds (i.e. metabolites) due to the high interfering ions generated by the organic matrix itself. The use of solid-state substrates instead of the classical matrices is very appropriate to overcome this problem. In this study we focus on developing a novel nanostructured substrate based on black silicon fabricated by reactive ion etching and coated with sputtered gold. The hydrophobic/hydrophilic properties of this surface have been tailored in order to detect both polar and nonpolar compounds. This surface demonstrated to be very effective for analyzing imprinted mouse brain tissues and fingerprints.

1. Introduction

Matrix-assisted laser desorption/ionization mass spectrometry (MALDI-MS) is a popular technique that has been used extensively in mass spectrometry imaging (MSI) for protein and peptide mapping of animal or vegetal samples. However, the main problems of this technique are the limited spatial resolution, the lack of spatial homogeneity and the difficulty to detect low molecular weight compounds (< 400 Da) because of the interfering signals coming from the organic matrices [1].

Nanostructured functional surfaces have been developed to eliminate the use of MALDI matrices and to overcome the above mentioned limitations. These matrix-free LDI-MS methods demonstrated their great value by their versatility: both liquid analysis and tissue metabolite mapping can be achieved at low concentrations and with little or no ion fragmentation [2].

We investigated the fabrication and use of novel gold-coated black silicon substrates (Au-BSi) for LDI metabolomics analysis of imprinted fingerprint and mouse brain tissue. Characterization of structure, reflectance, and hydrophilic/hydrophobic behavior revealed that the gold-coated black silicon substrate possesses optimal properties for LDI analysis.

2. Fabrication and Characterization

The black silicon substrates have been prepared using reactive ion etching (RIE) processes as previously described in [3]. A mixture of oxygen (O_2) and sulfur hexafluoride (SF_6) plasma with 1:1 ratio, was used to create the ordered needle-like structures as presented in Fig. 1. Afterwards, a gold layer of 10 nm thickness was deposited onto the black silicon by sputtering. Finally, the hydrophilic (hydrophobic) regions were obtained by applying O_2 (CHF_3) plasma treatment with the help of a silicon shielding mask (Fig. 1.).

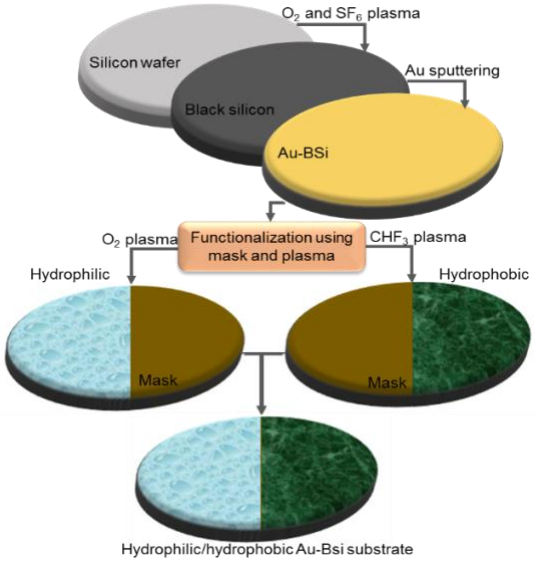

Fig. 1. Fabrication steps of selective Au-BSi substrate.

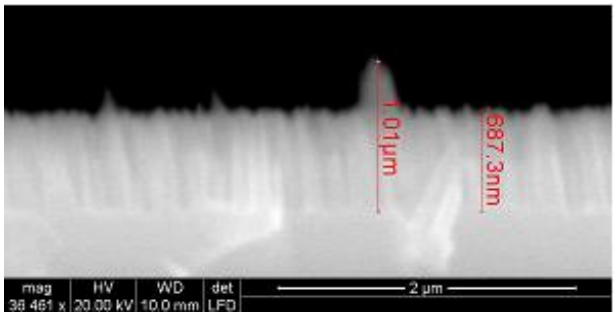

Fig. 2. Scanning Electron Microscopy cross-section image of Au-BSi substrate.

The black silicon surface presents a needle-like array structure (Fig. 2.), that absorbs visible light and gives the black aspect of silicon. Remarkably, at 337 nm (the wavelength of LDI-MS laser) the reflectance value is very low (<2%). The hydrophobic or hydrophilic property of the gold-coated black silicon surface was characterized with a contact angle (CA) measurement equipment. We fabricated the superhydrophobic surface with a mean CA of ~165º, due to CH_x terminal groups and the hydrophilic surface with a mean CA of ~45º, due to hydroxyl terminations (Fig. 3).

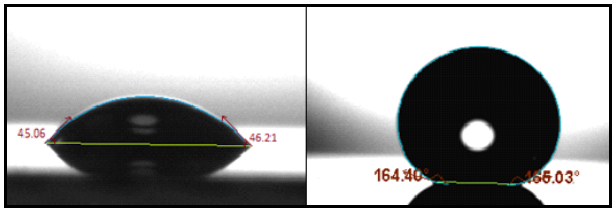

Fig. 3. Contact angle measurements on hydrophilic (left) and hydrophobic (right) Au-BSi substrates.

3. LDI-MS Results and Discussion

Both silicon nanostructure and Au nanolayer are contributing with their specific properties for the novel substrate. These properties enable the LDI acquisition of rich mass spectral data with a minimal interfering background. The black silicon nanostructure provides a biologically inert environment to which sample molecules can adhere without being contaminated. Also, black silicon absorbs the laser energy of the spectrometer and transforms it into energy necessary for desorption and ionization of molecules. The gold nanolayer plays two important roles: first, it helps the ionization and desorption processes of the analytes and second, the Au clusters peaks that appear in the spectra are used for spectrum calibration. It has been previously demonstrated that nano-sized gold layer is affected by the laser wavelength and interacts with the molecules to be ionized, thus guiding the ionization and desorption processes.

The MS images of imprinted fingerprint and mouse brain tissue are represented in Fig.4. The gold-coated black silicon substrate has successfully discriminated between ions of different polarity as they have adhered to their specific selective area. In the case of the fingerprint, the top half region was functionalized with hydrophilic terminations and the bottom half with hydrophobic terminations. To demonstrate the functionality of the selective regions, we represented the distribution of the hydrophilic ion *m/z* 284.34, which is uneven throughout the selective surface, as expected. In the case of the brain tissue, we mapped the concentration of the *m/z* 274.87 ion, which has adhered to the hydrophilic area of the surface (left side), suggesting that the ion is a hydrophilic metabolite.

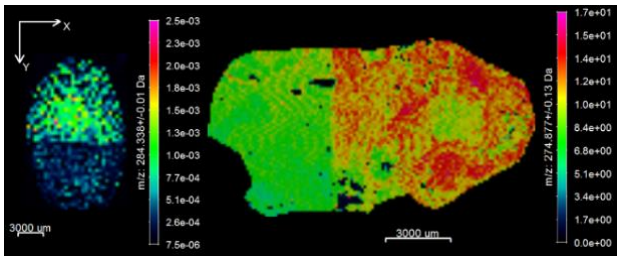

Fig. 4. Mass spectrometry imaging of fingerprint (left) and mouse brain tissue imprint (right) on the gold-coated black silicon substrate, with the color intensity scale.

4. Conclusion

Selective detection of hydrophobic or hydrophilic metabolites is possible with the help of our novel nanostructured gold-coated black silicon functional surfaces. We successfully differentiated between hydrophilic and hydrophobic molecules of imprinted fingerprints and mouse brain tissues. The nanostructured gold-coated black silicon substrates assisted in the ionization/desorption processes, facilitating detection in the low molecular mass range without interfering background signal.

Acknowledgments

The authors want to acknowledge the financial support of the Spanish Ministry of Economy and Competitivity through project TEC2015-69076-P and SAI´s pre-doctoral grant No. BES-2016-076483.

References

[1] T. Northen, O. Yanes, M. Northen et al. Clathrate nanostructures for mass spectrometry, *Nature* 7165, 1033-1036 (2007); doi: 10.1038/nature06195

[2] Y. Chen, G. Luo, J. Diao et al., M. Mouse, D. Duck, Laser desorption/ionization from nanostructured surfaces: Nanowires, nanoparticle films and silicon microcolumn arrays, *Journal of Physics: Conference Series* 1, 548-554 (2007); doi: 10.1088/1742-6596/59/1/117

[3] J. Gao, M. De Raad, B. Bowen et al., Application of Black Silicon for Nanostructure-Initiator Mass Spectrometry, *Analytical Chemistry* 3, 1625-1630 (2016); doi: 10.1021/acs.analchem.5b03452

Maximizing quality and information from NMR profiling data through the exploitation of information coming from metabolite signal parameters

Daniel Cañueto

1Metabolomics Platform, IISPV, DEEEA, Universitat Rovira i Virgili, Campus Sescelades, Carretera de Valls, s/n, 43007 Tarragona, Catalonia, Spain,)

Improving classification by harnessing the potential of 1H-NMR signal chemical shifts

(Manuscript pending publication)

Metabolomics studies use 1H-NMR spectra to quantify metabolite concentrations. Nevertheless, there is much more information available in a spectrum not used by now in metabolomics studies, such as the chemical shift of metabolite signals. This information may be helpful to enhance the discrimination of samples. Here, we demonstrate the potential of chemical shift to reach a much higher quality in sample characterization and discrimination. We applied the collection of the chemical shifts of metabolite signals in two public metabolomics study datasets. The accuracy in the classification of samples of smokers or of ulcerative colitis patients improves up to 20 percentage points thanks to the use of chemical shift information (Figure 1). Improved classification can be explained by the pH imbalance characteristic of the condition studied in both datasets. The high range of diseases characterized by pH imbalance suggests great potential in the use of chemical shift information to enhance the diagnostic and predictive properties of NMR.

Maximizing the NMR automatic profiling quality through prediction of expected metabolite signal parameters

(Manuscript submitted)

Automatic approaches to profile NMR data are compromised by multiple sources of variability present in complex matrices. These sources give variability to the parameters of metabolite signals, forcing profiling algorithms to relax their criteria (and, therefore, reducing their effectiveness). To maximize the quality of lineshape fitting during NMR profiling, it is necessary to restrict as much as feasible the possible value ranges in the parameters during lineshape fitting; therefore, it is necessary to create spectrum-specific value ranges for each parameter. This can be done if signals parameters are predicted with the information achieved during a first profiling iteration (Figure 2). The results of the study showed that the prediction of signal parameters values through the use of the information collected during a first profiling iteration helps maximize the profiling performance. In addition, our study also presents a new quality indicator based on the information generated by our machine-learning based pipeline. This new quality indicator provides higher-quality information than current approaches (e.g., lineshape fitting error) to improve the detection of suboptimal quantifications and to enable the detection of wrong annotations, two current bottlenecks in metabolomic studies.

rDolphin: a GUI R package for proficient automatic profiling of 1D 1H-NMR spectra of study datasets

(Manuscript published)

Adoption of automatic profiling tools for 1H-NMR-based metabolomic studies still lags behind other approaches in the absence of the flexibility and interactivity necessary to adapt to the properties of study data sets of complex matrices. To provide an open source tool that fully integrates these needs and enables the reproducibility of the profiling process. rDolphin incorporates novel techniques to optimize exploratory analysis, metabolite identification, and validation of profiling output quality.The information and quality achieved in two public datasets of complex matrices are maximized. rDolphin is an open-source R package (http://github.com/danielcanueto/rDolphin) able to provide the best balance between accuracy, reproducibility and ease of use.

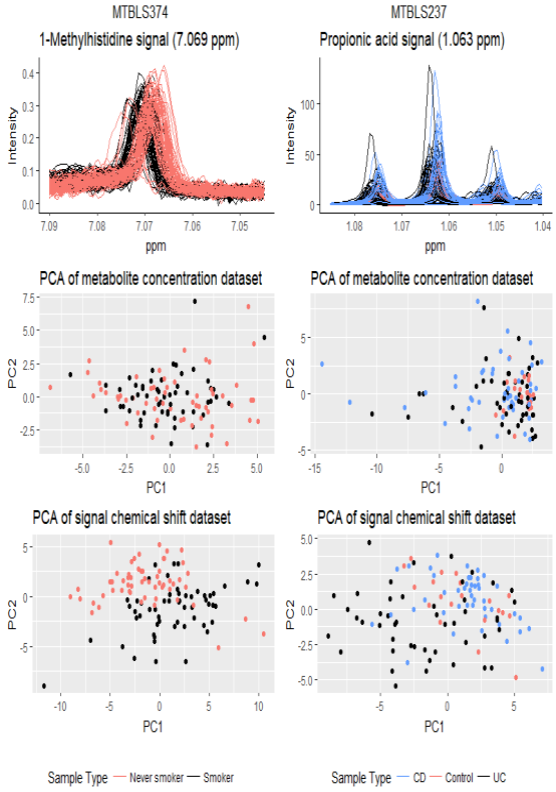

Figure 1: The samples are better differentiated by the location of the signals (parametrized by the chemical shift in ppm) than by their intensity (top). This pattern is observed in multiple signals in the dataset. As a result, the PCA of the collected chemical shifts of signals shows much better separation of samples than the PCA of the collected quantification of metabolite concentrations.

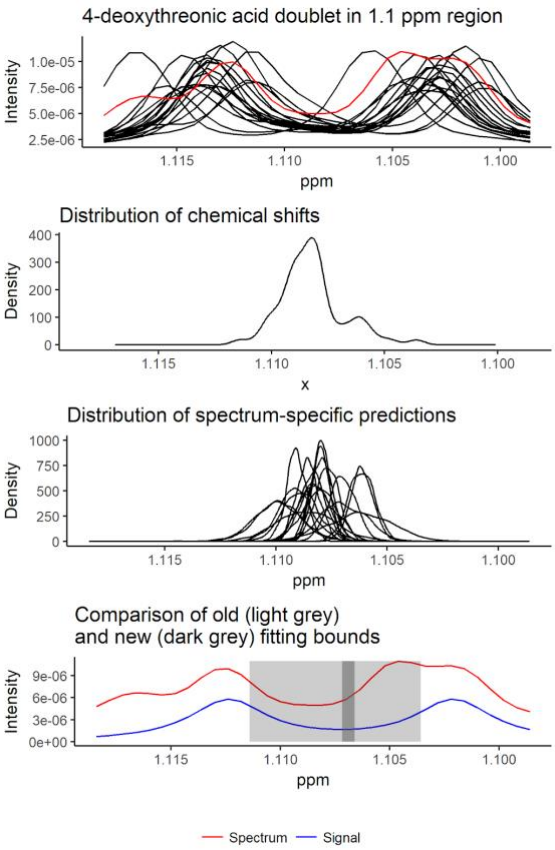

Figure 2: The signal parameter prediction pipeline enables a strict and accurate reduction in the bounds to use during lineshape fitting. The figure shows a very difficult signal fitting found with the 4-deoxythreonic acid signal in human urine matrix. The chemical shift variability present in this signal (a) forces lineshape fitting algorithms to consider a wide range of possible chemical shift values during the fitting (b). This wide compromises the right assignment of the doublet center when other signals appear adjacent to the signal to fit (d). The chemical shift prediction generates spectrum-specific chemical shift possible distributions (c). These distributions are very strict and can help generate much narrower fitting bounds (d)

$Al_xGa_{1-x}N$/AlN/GaN and DH- $Al_xGa_{1-x}N$/GaN HEMTs threshold voltage model

Wondwosen Eshetu Muhea *[1], Nawel Kermas[1], Fetene Mulugeta Yigletu[2], Roger Cabré[1], and Benjamin Iñiguez[1]

[1] Department of Electrical, Electronics, and Automation Engineering, Universitat Rovira i Virgili, Tarragona, Spain

[2] School of Electrical and Computer Engineering, AAIT, Addis Ababa, Ethiopia

Abstract

Physics based models for calculating the threshold voltage (V_{th}) of GaN-based high electron mobility transistor (HEMT) is proposed. Assuming that the 2DEG in III-V heterostructures originate from donor like surface states, an analytical expression for ϕ_b is derived based on the condition of charge neutrality across the barrier layer and applied to develop V_{th} model. Furthermore, the V_{th} models are implemented in the physics-based $I-V$ model previously proposed by our group for AlGaN/GaN HEMTs and tested with devices of different geometry. Excellent agreement is obtained between the model and experimental data of the drain current and transconductance of the devices over a full range of bias conditions.

1. Introduction

Hitherto physics-based models developed for GaN HEMTs account for the polarization effect in a unified threshold voltage (V_{th}) equation. However, this expression fails to accurately predict the parameter for GaN-based HEMT devices with Al concentration x over 0.15 [1]. In this work, we have presented a threshold voltage model that properly accounts for the polarization effect for $Al_xGa_{1-x}N$/[AlN]/GaN device.

2. Model derivation

The device band diagram is depicted in Fig.1. The potential drop across the AlGaN and AlN layers, V_{AlGaN} and V_{AlN}, can be expressed using Poisson's equation as

$$\frac{V_{AlGaN}}{d_{AlGaN}} = \frac{\sigma_{AlGaN}}{\varepsilon} - \frac{qn_s}{\varepsilon} \quad (1)$$

$$\frac{V_{AlN}}{d_{AlN}} = \frac{\sigma_{AlN}}{\varepsilon} - \frac{qn_s}{\varepsilon} \quad (2)$$

where, V_{AlGaN}, V_{AlN}, σ_{AlGaN}, and σ_{AlN} are the potential drop across the AlGaN and AlN layers and polarization induced charge in both layers respectively, n_s is the 2DEG density, d_{AlGaN} and d_{AlN} are thickness of the AlGaN and AlN layers, ε is the permittivity which is considered here as the same for both layers for simplicity.

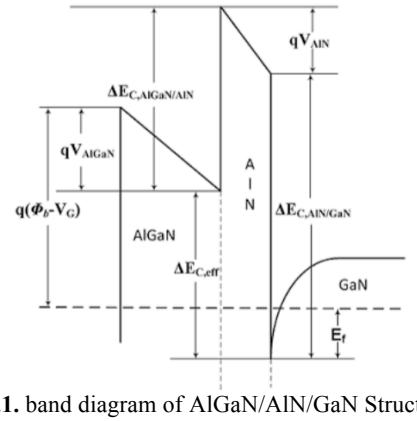

Fig.1. band diagram of AlGaN/AlN/GaN Structure.

Applying basic geometry rule on Fig.1, with V_G=0 and neglecting E_f, the Schottky barrier height (ϕ_b) can be expressed as

$$q\phi_b = qV_{AlGaN} + qV_{AlN} + \Delta E_{ef} \quad (3)$$

where, $\Delta E_{ef} = \Delta E_{AlN/GaN} - \Delta E_{AlGaN/AlN}$. $\Delta E_{AlGaN,AlN}$ and $\Delta E_{AlN,GaN}$ are the band offsets at the AlGaN/AlN and AlN/GaN interfaces respectively. Moreover, it has been shown in [2] that the origin of 2DEG in GaN based HEMTs is the donor-like surface states located at barrier layer surface. Therefore, n_S can be calculated as

$$n_s = n_0(q\phi_b - E_d) \quad (4)$$

where n_0 is donor state density per unit area per unit energy and E_d is the energy level below which the donor states are located. Solving (1), (2), (3) and (4) simultaneously gives

$$q\phi_b = \frac{\Delta E_{ef} + \frac{q^2 d n_0 E_d}{\varepsilon} + \frac{q}{\varepsilon}(\sigma_{AlGaN} d_{AlGaN} + \sigma_{AlN} d_{AlN})}{\left(q^2 n_0 d / \varepsilon\right) + 1} \quad (6)$$

Based on the physics of heterojunctions, and considering the effect of the gate bias (V_G), an analytical expression for the 2DEG density is derived as

$$n_s = (\varepsilon/qd)(V_G - V_{th} - E_f) \quad (7)$$

where, n_s is the 2DEG density, $d = d_{AlGaN} + d_{AlGaN}$. d_{AlGaN} and d_{AlN} are thickness of the AlGaN and AlN layers respectively, E_f is the Fermi level, V_G is the applied gate voltage. V_{th} corresponds to the polarization dependent threshold voltage which is expressed as

$$V_{th} = \phi_b - \frac{\Delta E_{ef}}{q} - \left(\frac{\sigma_{AlGaN} d_{AlGaN}}{\varepsilon} + \frac{\sigma_{AlN} d_{AlN}}{\varepsilon}\right) \quad (8)$$

3. Results

The above V_{th} and ϕ_b models are incorporated in *I-V* model for GaN HEMTs presented in [3], and one AlGaN/AlN/GaN device was simulated (Fig. 2 and Fig. 3). Excellent fit is obtained for the device characteristics and this validated the models proposed in this work. Furthermore, we have adapted the V_{th} and *I-V* models presented in [1] and [3] respectively, for the first time, for double channel (DH) AlGaN/GaN device and good agreement is achieved between the model generated and experimental data of the device characteristics (Fig.4 and Fig.5).

7. Conclusions

We have presented a Schottky barrier and threshold voltage model for AlGaN/AlN/GaN and DH-AlGaN/GaN HEMTs. A good level of accuracy is obtained between the model and experimental data.

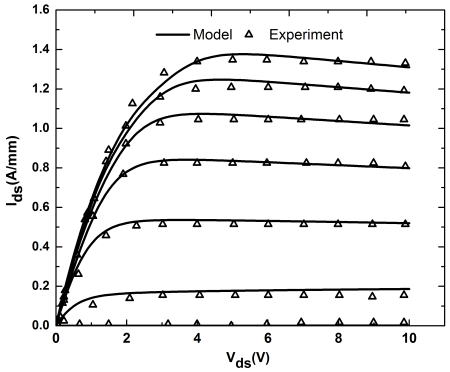

Fig.2. output characteristics of AlGaN/AlN/GaN structure (experimental data from [4]).

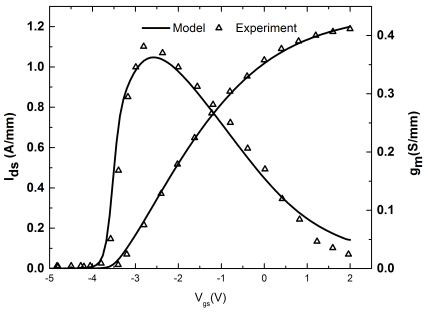

Fig.3. Transfer characteristics of AlGaN/AlN/GaN structure (experimental data from [4]).

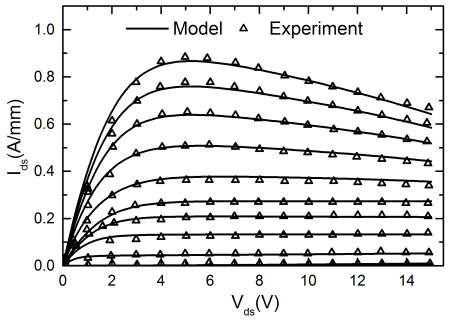

Fig.4. output characteristics of DH-AlGaN/GaN structure (experimental data from [5]).

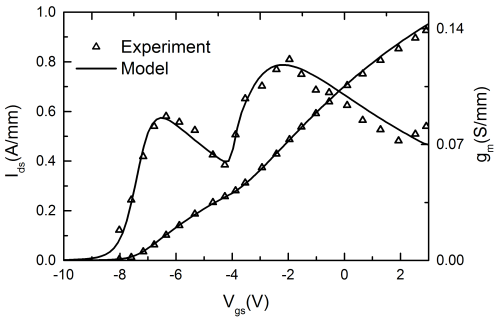

Fig.5. Transfer characteristics of DH-AlGaN/GaN structure (experimental data from [5]).

References

[1] Muhea, W. E., Yigletu, F. M., Cabré-Rodon, R., & Iñiguez, B. "Analytical Model for Schottky Barrier Height and Threshold Voltage of AlGaN/GaN HEMTs with Piezoelectric Effect". *IEEE Trans. on Electron Dev.*, pp. 901-907, 2018.

[2] Nitin Goyal and Tor A. Fjeldly, "Effects of strain relaxation on baresurface barrier height and two-dimensional electron gas in Al_xGaN_{1-x}/GaN heterostructures", *Material Research Society, Spring Meeting, San Francisco*, Vol. 1538, USA, April 2013.

[3] F. M. Yigletu, S. Khandelwal, T. A. Fjeldly, and B. Iñiguez, "Compact Charge-Based Physical Models for Current and Capacitances in AlGaN/GaN HEMTs", *IEEE Trans. on Electron Dev.*, vol. 60, pp. 3746- 3752, November 2013.

[4] Wang, X. L., Cheng, T. S., Ma, Z. Y., Hu, G. X., Xiao, H. L., Ran, J. X., & Luo, W. J. "1-mm gate periphery AlGaN/AlN/GaN HEMTs on SiC with output power of 9.39 W at 8 GHz". *Solid-state elect.*, Vol. 51, pp. 428-432. 2007.

[5] Chu, R., Zhou, Y., Liu, J., Wang, D., Chen, K. J., & Lau, K. M. "AlGaN-GaN double-channel HEMTs". *IEEE Trans. on elect. devices*, Vol. *52*, pp. 438-446.2005.

Carrier Kinetics Identification in Semiconductor Polymer Based Perovskite Solar Cells by Femtosecond Transient Absorption Spectroscopy

J. Jiménez-López[1, 2]; B.M.D. Puscher[3]; W.Cambarau[1]; E. Palomares[1, 4]; D. M. Guldi[3]

[1]Institute of Chemical Research of Catalonia (ICIQ), Barcelona Institute of Science and Technology (BIST), Avda. Països Catalans 16, 43007, Tarragona, Spain.
[2]Department d'Enginyeria Electrònica, Elèctrica I Automàtica, Universitat Rovira i Virgili, Avda. Països Catalans 16, 43007, Tarragona, Spain.
[3]Department of Chemistry and Pharmacy, Friedrich-Alexander-Universität Erlangen-Nürnberg, Egerlandstr. 3, 91058, Erlangen, Germany.
[4]ICREA, Passeig LLuis Companys 28, 08018, Barcelona, Spain.

Abstract

Femtosecond Transient Absorption Spectroscopy (fs-TAS) is a useful technique which allows to make studies on the kinetics at very fast time scales (up to the femtosecond timescale ~ 10^{-15} s). In this work, we have used this technique to identify and analyze carrier kinetics in lead halide perovskite solar cells.

Also, we have identified charge transfer processes between the photoactive material, perovskite, and both charge extraction layers, TiO_2 as Electron Transporting Material (ETM), and a series of semiconducting polymers that act as hole transporting materials (HTM) in Perovskite Solar Cells.

1. Introduction

Since 2009, the first time that lead halide perovskite was applied as light sensitizers in solar cells[1]; there has been some kind of revolution in the field of photovoltaics, with more than 3000 papers published last year on perovskite solar cells.

These great efforts have supposed power conversion efficiencies (PCE) bigger than 22%[2] by different strategies in the solar cell fabrication, especially in the perovskite preparation step.

Even though these great efficiencies have been achieved in less than 10 years, there are a lot of physical insights that need to be understand, as it could be charge generation, ionic movement, charge transport or charge recombination. For this purpose, researchers have used a variety of techniques, optical (transient absorption spectroscopy[3,4], or time resolved photoluminescence[5]), electrical (transient techniques[6] or impedance spectroscopy[7]), or even computational simulations and modelling[8,9].

Here, using femtosecond transient absorption spectroscopy, we have study charge carrier processes in methylammonium lead iodide (MAPI) perovskite. Additionally, we have studied charge transfer processes, both for electrons to the electron transporting material, the TiO_2 layer; and holes to the hole transporting material, which in this case have been a series of semiconducting polymers (PTB7, P3HT, and PCPDTBT) compared with the reference material, spiro-OMeTAD small molecule.

Finally, we have tried to disseminate why these semiconducting polymers, widely used as donor materials in organic solar cells, they do not work as efficient in perovskite solar cells. It seems that we found a carrier pathway, which suppose a carrier loss at the MAPI/HTM interface.

2. Results and discussion

From the fs-TAS results on MAPI films (fig. 1), it is easy to appreciate two ground state bleaching (GSB) signals, which correspond to the two bands observed at 480 and 760 nm in the UV-Vis spectra, and that have been related to the depopulation of two valence bands. Also, there is a big photoinduced absorption (PIA), between the two GSB signals as well as in the near-IR region, that has been associated with changes in the refraction index. Finally, it has to be remarked the positive signal observed at early stages around 780 nm. This signal has been assigned to the existence of hot carriers in the sample, before they relax to the conduction band edge. The presence of these hot carriers will be commented in depth.

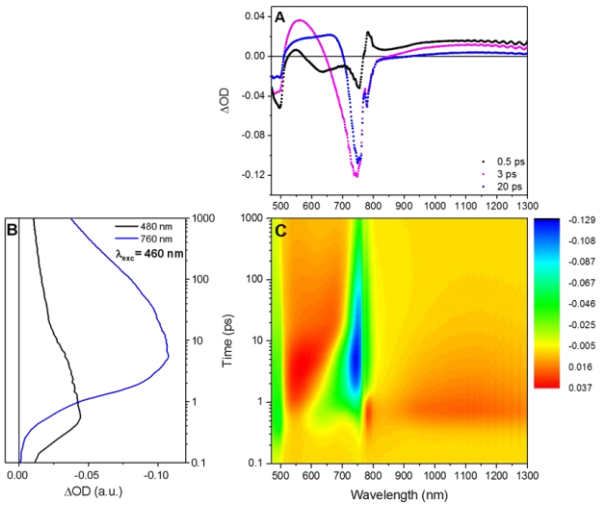

Fig. 1. Fs-TAS spectra in the visible and NIR (c) of MAPI films following λexc = 460 nm. Differential absorption spectra (a) shown in c) with different time delays: 0.5 ps (black spectrum), 3 ps (purple spectrum), and 20 ps (blue spectrum). Time absorption profiles (b) of the spectra shown in c): 480 nm (black spectrum) and 760 nm (blue spectrum).

After identifying the characteristic signal corresponfing to the MAPI perovskite, we obtain the spectra for the films with TiO_2/MAPI or MAI/HTM (HTM = spiro-OMeTAD, PTB7, P3HT, and PCPDTBT). In the visible range, the signals assigned to the perovskite are the most prominent ones, while for the near-IR region, different peaks appear for every material, related with the presence of charges in that material (fig. 2). So, we have identified charge injection signals into the different ETM and HTMs through their polaronic signature in the IR region.

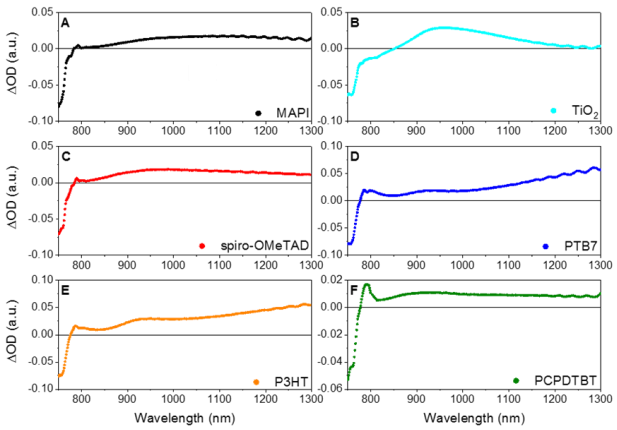

Fig. 2. Comparison of the differential absorption spectra in the NIR of the different MAPI films (MAPI (a), TiO_2/MAPI (b), and MAPI/HTM; HTM = spiro-OMeTAD (c), PTB7 (d), P3HT (e), or PCPDTBT (f)) at 1.2 ps with λexc = 460 nm.

Finally, we follow the kinetics at 780 nm, related with the hot carriers. The formation of the GSB is delayed up to 8 ns for some of the polymers (P3HT and PCPDTBT), precisely the ones that exhibited lower PCE[10]. We hypothesize a possible carrier loss pathway, in which the hot carriers are injected in the MAPI/HTM interface, just to relax back to the conduction band edge of the perovskite. Compared with spiro-OMeTAD, with a higher LUMO level, acting as electron blocking layer, this behaviour is not observed.

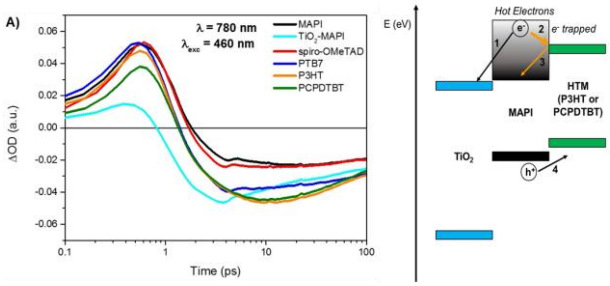

Fig. 3. (left) Kinetic traces at λ = 780 nm for MAPI, MAPI/TiO_2, and MAPI/HTM films. (right) Schematic representation of the interfacial charge transfer process suggested.

3. Conclusions

We have identified and analyzed fs-TAS spectrum of different lead halide perovskite films, identifying charge generation and charge injection processes into different charge extraction layers. Also, we have identified the corresponding signal to carriers in these charge extraction layers, found in the IR region of the spectra. Finally, we found a carrier loss pathway in some of the polymeric HTM that could explain their differences in PCE.

References

(1) A. Kojima et al., *J. Am. Chem. Soc.* **2009**, *131* (17), 6050–6051.
(2) NREL Efficiency Records Chart.
(3) Manser, J. S.; Kamat, P. V. *Nat. Photonics* **2014**, *8* (9), 737–743.
(4) P. Piatkowski, *Phys. Chem. Chem. Phys.* **2015**, *17*, 14674–14684.
(5) M.J.P. Alcocer et al., *Science* **2014**, *342* (2013), 341–344.
(6) N.F. Montcada et al., *ACS Energy Lett.* **2017**, *2* (1), 182–187.
(7) I. Zarazua et al., *J. Phys. Chem. Lett.* **2016**, *7* (24), 5105–5113.
(8) A.M.A. Leguy et al., *Nanoscale* **2016**, *8* (12), 6317–6327.
(9) G. Grancini et al., *Nat Phot.* **2015**, *9* (10), 695–701.
(10) J. Jiménez-López et al., *Sci. Rep.* **2017**, *7* (1), 6101.

Scaling correlation between DG & GAA MOSFETs

Kerim Yılmaz[1,2,⋆], Ghader Darbandy[1], Benjamín Iñíguez[2], François Lime[2] and Alexander Kloes[1]
[1]NanoP, TH Mittelhessen University of Applied Sciences, Giessen, Germany,
[2]DEEEA, Universitat Rovira i Virgili, Tarragona, Spain,
⋆e-mail: kerim.yilmaz@ei.thm.de, phone: +49 641 309 1965

***Abstract*—For compact modeling it is a challenge to analytically describe cylindrical gate-all-around (GAA) MOSFETs in 3-D with the simplest symmetric double-gate (DG) MOSFET in 2-D. It gets more complicated when short-channel effects play a role for nanoscale devices. We present a way to predict the center and surface potential (Φ_C and Φ_S) as well as the subthreshold swing (S_{sth}) and the drain-induced barrier lowering (DIBL) for a given device dimension and in case of intrinsic channels. For this aim only the channel length has to be scaled. We compare 2-D DG with 3-D GAA MOSFET simulation data from Technology Computer Aided Design (TCAD) for these four device properties to prove the introduced scaling theory.**

I. Introduction

For an ideal subthreshold swing and to reduce the DIBL effect in short channel devices, it is necessary to surround the complete channel with gate material. As a consequence the electrostatic control of the gate electrode in GAA MOSFETs is much better than in DG MOSFETs. By cutting a cylindrical GAA MOSFET of radius R lengthwise through the center we get a 2-D DG MOSFET of thickness $t_{ch} = 2R$ (see Fig. 1). This means, if we know the electrostatic behavior of the 2-D structure, we can trace back to the 3-D structure due to the rotational symmetry. By considering the subthreshold region the most important values, which are needed are position and value of Φ_C and Φ_S. Earlier evanescent-mode analysis [1] predict that DG MOSFETs can be scaled to 53 % larger channel length than GAA MOSFETs. TCAD simulations show us that a fixed scaling factor of 1.53 is not usable for all device dimensions. In addition, Φ_C and Φ_S need different scaling factors. Therefore, we derive an analytical expression which shows a dependence on the channel thickness $t_{ch} = 2 \cdot R$ and oxide thickness t_{ox}.

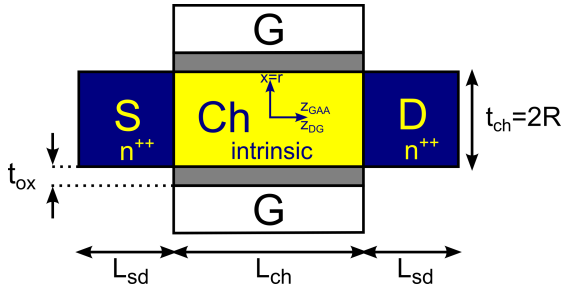

Figure 1. Sketch of an n-i-n type silicon DG MOSFET with its parameters: The source/drain S/D region is highly n-doped ($N_{sd} = 10^{20}/cm^3$) and $L_{sd} = 10\ nm$ long. The channel is intrinsic and its length ($L_{ch} = 1.5R, 2R, 2.5R, 3R, 3.5R, 4R, 5R, 6R$) is radius-dependent ($R = 4, ..., 10\ nm$). The gateoxide is made of the high-κ material HfO_2 ($t_{ox} = 1\ nm$).

II. Derivation of a device dimensions dependent scaling factor

Yan et al. [2] and Suzuki et al. [3] derived equations for the so-called natural length λ.

$$\text{Yan et al.:}\quad \lambda^S_{DG} = \sqrt{\kappa\ t_{ox} R} \tag{1}$$

$$\text{Suzuki et al.:}\quad \lambda^C_{DG} = \sqrt{\kappa\ t_{ox} R \cdot \left(1 + \frac{R}{2\ \kappa\ t_{ox}}\right)} \tag{2}$$

where $\kappa = \epsilon_{ch}/\epsilon_{ox}$, ϵ_{ch} and ϵ_{ox} are the dielectric constant of Si and HfO_2, R is the half channel thickness and t_{ox} is the gate oxide thickness. Both assume the electrostatic potential Φ from gate to gate as a parabolic function. Yan et al. solve the Laplace equation along the surface and Suzuki et al. along the center, where most of the leakage current flows. Based on Yan et al.'s theory the ideal subthreshold factor remains the same, if the device is designed maintaining $\alpha = \frac{L_G}{2\lambda}$ where L_G is the gate length. Auth et al. [4] derived the cylindrical natural length along the center of a device:

$$\lambda^C_{GAA} = \sqrt{\kappa\ t_{ox} R \cdot \left(\frac{R}{t_{ox}} \ln\left(1 + \frac{t_{ox}}{R}\right) + \frac{R}{2\ \kappa\ t_{ox}}\right)\frac{1}{2}} \tag{3}$$

In this paper, we derive the missing cylindrical natural length along the surface of a device. The main difference to the derivation done by Auth et al. [4] is to eliminate Φ_C instead of Φ_S so that the equation for the potential $\Phi(r, z)$ is

$$\Phi(r,z) = \Phi_S(z) - \frac{\Phi_g - \Phi_S(z)}{2\kappa \ln\left(1 + \frac{t_{ox}}{R}\right)} + \frac{\Phi_g - \Phi_S(z)}{2\kappa R^2 \ln\left(1 + \frac{t_{ox}}{R}\right)} r^2 \tag{4}$$

where Φ_g is the gate potential. Now the solution of the Poisson's equation at the surface is

$$\frac{\partial^2}{\partial z^2}\Phi_S(z) - \frac{(\Phi_S(z) - \Phi_g)}{(\lambda^S_{GAA})^2} = \frac{qN_a}{\epsilon_{ch}} \tag{5}$$

where N_a is the channel doping concentration (here: $N_a = 0$) and λ^S_{GAA} is

$$\lambda^S_{GAA} = \sqrt{\kappa\ t_{ox} R \left(\frac{R}{t_{ox}} \ln\left(1 + \frac{t_{ox}}{R}\right)\right) \cdot \frac{1}{2}}. \tag{6}$$

In all four cases the potential drops exponentially along the channel as $\Phi(r, z) \propto \exp(\pm z/\lambda)$. To get the same potential profile along the surface and center we compare the corresponding exponents using the equations (1), (6) and (2), (3).

Thus, we get the scaling factor for the channel length:

$$z^S_{DG} = \sqrt{2} \cdot \sqrt{\frac{t_{ox}/R}{\ln\left(1+\frac{t_{ox}}{R}\right)}} \cdot z^S_{GAA} \quad (7)$$

$$z^C_{DG} = \sqrt{2} \cdot \sqrt{\frac{1+\frac{R}{2\kappa\ t_{ox}}}{\frac{R}{t_{ox}}\ln\left(1+\frac{t_{ox}}{R}\right)+\frac{R}{2\kappa\ t_{ox}}}} \cdot z^C_{GAA} \quad (8)$$

In equation (8), the second addend in the numerator and denominator are dominant over the first addend for $R >> t_{ox}$. This results in

$$z^C_{DG} \approx \sqrt{2} \cdot z^C_{GAA} \quad (9)$$

Furthermore, Oh et al. [1] hold the view that a parabolic approximation of Φ differs widely from that of the sinusoidal solution and derive a potential $\Psi^\star$ for DG and GAA MOSFETs, which satisfies the Laplace equation. We simplify these equations due to the fact that source and drain are equally doped and consider them without any bias:

$$\Psi^\star_{DG} \approx \Phi_C \cdot \cos\left(\frac{x}{\lambda_{DG}}\right) \cdot \cosh\left(\frac{z_{DG}}{\lambda_{DG}}\right) \quad (10)$$

$$\Psi^\star_{GAA} \approx \Phi_C \cdot J_0\left(\frac{r}{\lambda_{GAA}}\right) \cdot \cosh\left(\frac{z_{GAA}}{\lambda_{GAA}}\right) \quad (11)$$

J_0 is the Bessel function of order zero. By fulfilling the boundary condition at the channel/oxide interface and assuming $R >> t_{ox}$ for the same channel thickness ($t_{ch} = 2R$) it follows $z^S_{DG} \approx \frac{\lambda^S_{DG}}{\lambda^S_{GAA}} \cdot z^S_{GAA} \approx 1.53 \cdot z^S_{GAA}$. In addition we compare both equations (10), (11) along the center of a device by a first order Taylor polynomial without any regard to the boundary conditions at the channel/oxide interface:

$$\cos\left(\frac{x}{\lambda_{DG}}\right) \approx 1 - \frac{x^2}{2\lambda^2_{DG}} \overset{!}{\approx} 1 - \frac{r^2}{4\lambda^2_{GAA}} \approx J_0\left(\frac{r}{\lambda_{GAA}}\right) \quad (12)$$

Accordingly, equation (9) follows from $\lambda_{DG} = \sqrt{2}\lambda_{GAA}$.

III. Simulation Data and Conclusions

In the first place we realized that the sinusoidal solution of the potential gives better results at the channel/oxide interface than the parabolic ansatz. On the other hand we need a device dimensions dependent scaling factor, which is achieved with the parabolic solution. As a conclusion, combining both leads to the best solution. Thus, we obtain two different scaling factors for the surface and center potential:

$$z^S_{DG} = 1.53 \cdot \sqrt{\frac{t_{ox}/R}{\ln\left(1+\frac{t_{ox}}{R}\right)}} \cdot z^S_{GAA} \quad (13)$$

$$z^C_{DG} = \sqrt{2} \cdot \sqrt{\frac{t_{ox}/R}{\ln\left(1+\frac{t_{ox}}{R}\right)}} \cdot z^C_{GAA} \quad (14)$$

In Figs. 2-5 TCAD results for GAA-FETs with channel length L_{GAA} are compared to results for DG-FETs of which the channel length has been obtained by scaling L_{GAA} according to (13) or (14). Simulation data (without quantum confinement) show us that equation (14) only works for Φ_C (see Figure 2). Equation (13) works for Φ_S, DIBL and swing except for the channel length $L_{ch} = 1.5R$ (see Figures 3, 4 & 5). It is interesting to see that Φ_S is more important than Φ_C although the leakage current below threshold flows in the center. This needs further study.

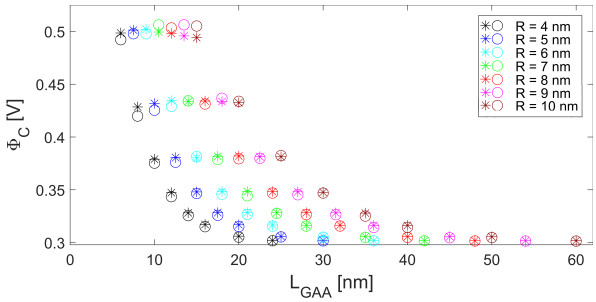

Figure 2. Relationship between Φ_C and L_{GAA} with various channel thickness. (○: GAA, ∗: DG, scaling by (14))

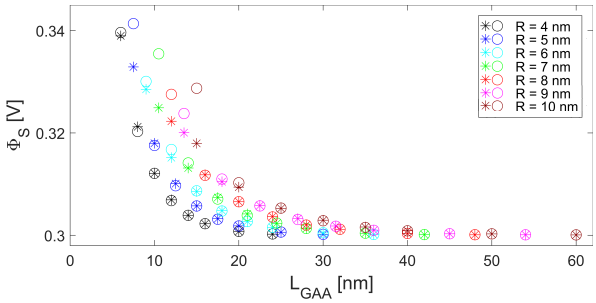

Figure 3. Relationship between Φ_S and L_{GAA} with various channel thickness. (○: GAA, ∗: DG, scaling by (13))

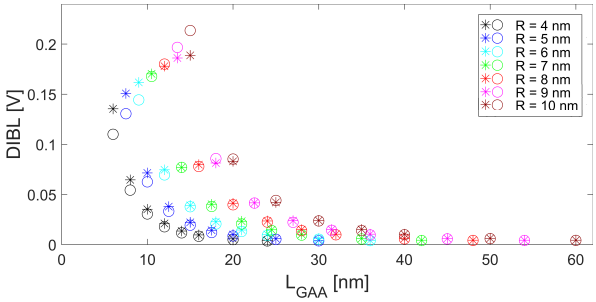

Figure 4. Relationship between DIBL ($\Delta V_{ds} = 0.9V$) and L_{GAA} with various channel thickness. (○: GAA, ∗: DG, scaling by (13))

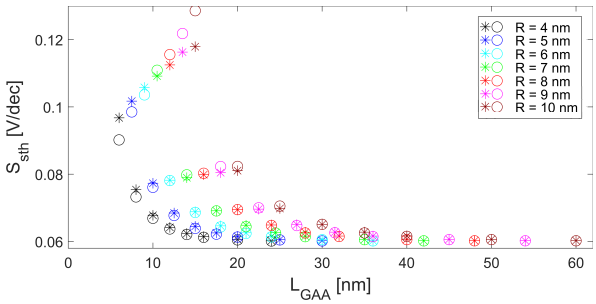

Figure 5. Relationship between swing at $V_g = 1V$ gate bias and L_{GAA} with various channel thickness. (○: GAA, ∗: DG, scaling by (13))

References

[1] S.-H. Oh, D. Monroe, and J. Hergenrother, *IEEE Electron Device Lett.*, vol. 21, no. 9, pp. 445–447, 2000.

[2] R. H. Yan and A. Ourmazd and K. F. Lee, *IEEE Trans. Electron Devices*, vol. 39, no. 7, pp. 1704–1710, Jul. 1992.

[3] K. Suzuki, T. Tanaka, Y. Tosaka, H. Horie, and Y. Arimoto, *IEEE Trans. Electron Devices*, vol. 40, no. 12, pp. 2326–2329, Dec. 1993.

[4] C. P. Auth and J. D. Plummer, *IEEE Electron Device Lett.*, vol. 18, no. 2, pp. 74–76, Feb. 1997.

WO_3 Nanowires Decorated with Nickel Oxide Nanoparticles for H_2S Detection

Navarrete E.[1], Bittencourt C.[2], Umek P.[3], Llobet E.[*1]

[1]MINOS-EMaS, Universitat Rovira i Virgili, Avda. Països Catalans, 26, 43007 Tarragona, Spain,

[2]Chimie des Interactions Plasma – Surface (ChIPS), Research Institute for Materials Science and Engineering, Université de Mons, Avenue Copernic 1, 7000 Mons, Belgium,

[3]Jožef Stefan Institute, Jamova cesta 39, 10000 Ljubljana, Slovenia.

Correspondence: eduard.llobet@urv.cat; Tel.: +34 977 558 502

Abstract

Single-step or two-step aerosol assisted chemical vapor deposition methods have been used to grow single crystalline tungsten oxide nanowires loaded with different concentrations of nickel oxide nanoparticles. Working temperatures and nickel loadings were studied and optimized to achieve the optimal working conditions for detecting hydrogen sulfide. Morphology, crystalline structure, composition, sensing properties and mechanisms will be presented and discussed in detail. The two-step method allows for controlling Ni loading in a wide range while keeping constant particle size.

1. Introduction

Global emissions of gas pollutants have exponentially risen in the past decades. Developing stable, highly sensitive and selective inexpensive sensors has been a major driver in the development of nanosized metal oxides gas sensors. Here we focus on the growth, through aerosol assisted chemical vapor deposition, of n-type WO_3 nanowires loaded with p-type nickel oxide nanoparticles. The objective is to achieve both chemical and electronic sensitization effects to achieve sensitive and potentially selective H_2S metal oxide sensors [1]. The effect of nickel oxide nanoparticles can enhance the sensor response through a reversible sulfurization mechanism. Different routes are explored to effectively achieve a wide range of Ni loading, so optimization can be envisaged.

2. Experimental

Two approaches were used to grow the nickel loaded tungsten oxide wires. The one step methodology consisted on mixing 50 mg of $W(CO)_6$ as WO_3 organic precursor with 2.5 mg or 5 mg of $Ni(acac)_2$ as organic precursor for nickel nanoparticles in a solution of acetone: methanol (ratio 3:1). Once the deposition is finished the sensors were annealed inside a muffle heated at 5 ºC/min up to 500 ºC and hold for 120 minutes, to remove the carbon impurities found due to the solvents and the precursors used. The two step methodology consists of growing in first place the nanowires forest, perform the annealing step described above and subsequently a second AACVD process is performed to load the nickel mixing 2.5 mg or 5 mg $Ni(acac)_2$ in 10 ml of methanol. Finally, the sensors are placed inside the muffle to perform a second annealing. Through this methodology a set of 5 different types of sensors were obtained: pure WO_3, a single step low Ni-loaded or high Ni-loaded WO_3, and a double step low or high Ni-loaded WO_3. These are labelled as WO_3, 1LC, 1HC, 2LC and 2HC, respectively. The structure, morphology and composition of sensors were characterized via XRD, E-SEM, HRTEM and XPS.

Sensors were exposed to a continuous flow of different concentrations of H_2S, NO_2, CH_4 and ethanol under dry and humidified conditions. The effect of sensor operating temperature was studied too.

3. Results

Material characterization

Fig 1 shows a well-defined nanowire forest with nickel nanoparticles covering their tips. Also, HRTEM shows their high crystallinity. XRD revealed a quasi-stoichiometric WO_3 with a P-1 space group belonging to a triclinic structure fitting well with the JPCDS 73-0305. The chemical composition (derived from XPS) of a few samples is summarized in Table 1.

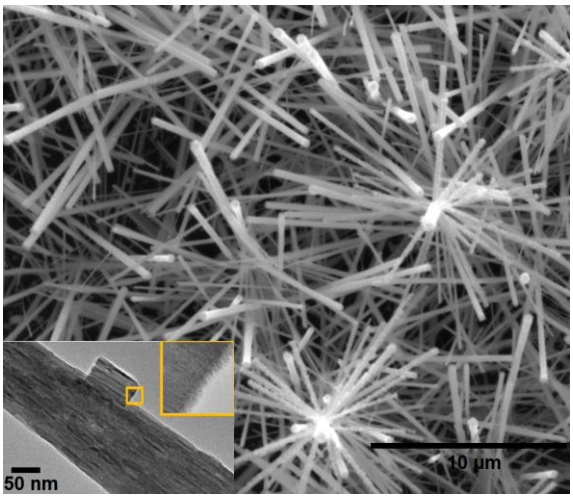

Fig.1. ESEM an HR-TEM image from WO_3 2Ni/HC.

Tab. 1: XPS quantitative analysis for Ni/HC sensors.

	W wt%	O wt%	Ni wt%
WO_3	25.0	75.0	-
1Ni/HC	22.0	76.0	**2.0**
2Ni/HC	20.0	65.0	**15.0**

Despite using the same quantity of nickel organic precursor, the 1 step methodology revealed a poor loading in contrast with the two steps methodology which is more efficient and results in a higher nickel-loading in the nanowires forest surface.

Gas sensing results

The optimal operating temperature was determined for the different sensors and gases tested. Highly Ni-loaded tungsten oxide nanowires are very sensitive to hydrogen sulfide. Employing the 2-step synthesis process, highly Ni-loaded nanowires are 5-fold more sensitive to H_2S than pure WO_3 nanowires. In addition, the optimal working temperature is decreased from 250 ºC to 150 ºC. This sensor is far more responsive to hydrogen sulfide than to any of the other species tested. Fig. 2 shows these results. Furthermore, the 2Ni/HC sensor was tested under humid conditions. At 35 %R.H. the response increases towards low H_2S concentrations, lowering the detection limit down to ppb level. Responsiveness, however, decreases at high hydrogen sulfide concentrations. This behaviour can be due to hydroxyl groups present at the surface, which compete with oxygen for surface sites, decreasing the available reactive oxygen for H_2S at higher concentrations.

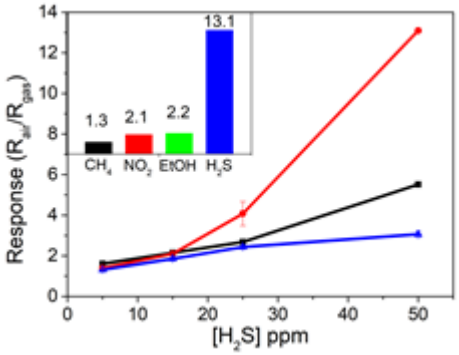

Fig. 2: Response towards H2S of 2Ni/HC (red) 1Ni/HC (black) and WO3 (blue) sensors at their optimal working temperature. Inset: Response of the 2Ni/HC sensor for the different species tested.

Gas sensing mechanism

The reaction mechanism involved in H_2S sensing relies on oxygen surface species [2].

$O_2^-{}_{(ads)} + e^- \rightarrow 2O^-{}_{(ads)}$ (150 to 400 ºC) (1)
$H_2S + 3O^- \rightarrow SO_2 + H_2O + 3e^-$ (2)

The nickel nanoparticles suffer a sulfurization which can be partially reversible through the following mechanism [3]:

$NiO(s) + H_2S(g) \rightarrow NiS(s) + H_2O(g)$ (3)
$3NiS(g) + 2H+(aq) \rightarrow Ni_3S_2(s) + H_2S(g)$ (4)
$Ni_3S_2(s) + 7/2O_2(g) \rightarrow 3NiO(s) + 2SO_2(g)$ (5)
$Ni_3S_2(s) + 9/2O_2(g) \rightarrow 2\ NiSO_4(s) + NiO(s)$ (6)

4. Conclusions

The AACVD method has been employed successfully to grow WO3 nanowires loaded efficiently with nickel oxide nanoparticles increasing significantly sensor response towards H_2S. A study to determine the optimal working temperature and nickel loading has been carried out. Full details will be shown at the conference.

5. References

[1] C. Wang, L. Yin, L. Zhang, D. Xiang and R. Gao, Metal Oxide Gas Sensors: Sensitivity and Influencing Factors. Sensors 10(3), 2088–2106(2010)

[2] D. V. Ahire, G. E. Patil, D. D. Kajale, V. B. Gaikwad and G. H. Jain, Chapter 10: Nanostructured Nickel Oxide by Hydrothermal Route for Gas Sensing Applications. In Sensing Technology: Current Status and Future Trends I, Smart Sensors, Measurement and Instrumentation 7 (pp. 181-193)(2013)

[3] A. T. Atimtay, D. P. Harrison, (2013). Desulfurization of Hot Coal Gas. Berlin: Springer Berlin.

Compact Modeling of Gate Capacitance in Organic Thin Film Transistors

H. Cortes-Ordonez[1], B. Iniguez[1]

[1] Department of Electric, Electronic and Automatic engineering of Universitat Rovira i Virgili (e-mail: harold.cortes@urv.cat)

Abstract

In this abstract we target the compact capacitance modeling of organic thin film transistor (OTFTs) that works from depletion to accumulation regime taking into account the frequency dependence. The parameters used in the model are calculated through unified model and parameter extraction method (UMEM). We study the effect related to the density of localizated states. Finally, we analyze the experimental derivative of the gate capacitance and we demonstrate that our model predicts it with a high degree of accurate.

1. Introduction

In the past years, substantial research has been made on Organic TFT modeling [1], giving emphasis to develop an accurate *I-V* model for these devices. However, little attention has been given to model the C-V characteristics of the device [2] [3] [4] [5] [6] [7].

Regarding *C-V* modeling, there are few models of capacitance in accumulation regime; other models apply different function for the accumulation regime and the subthreshold regime [8]. Also, there are capacitance models which consider the frequency dependence. These models can be used for low, medium and high frequencies [9]. Nevertheless, to the best of our knowledge, there is no capacitance model that works over a wide range of frequencies and valid up to the first capacitance derivative using a analytical expression.

In this document, we present a compact capacitance model developed for OTFTs valid from depletion to accumulation regime with continuous and smooth transition as well as the first capacitance derivative. This model take into account the mobility and current from low to high frequencies. The compact capacitance model uses UMEM parameter extraction procedure presented in [2]; parameters are extracted from *I-V* data.

The compact capacitance model developed is used to analyze the effect of the parameter related to the density of states (DOS) in the capacitance. In accordance to [8], OTFTs shows a high crystallinity degree when this parameter is close to 0.

The capacitance derivative has been considered as a method to extract V_T and V_{FB} in crystalline field effect transistors (Equivalent to the second derivative method) [10] [11] [12] [13]. Here we study it in OTFTs and from it we discuss the information provides regarding V_T, V_{FB} and the operating regimes in OTFTs. We demonstrate that our model reproduces it very well.

2. Capacitance Model

Capacitance model develop in this work is based in [9] with specific improvements in depletion regime. The OTFTs used in the measurement were top gate bottom contact multifingers with L = 20µm and W = 7980 µm.

The measurements were taken at three different frequencies: low frequency of 500Hz, medium frequency that equals to 1 kHz and at high frequency of 10 kHz. The equipment used for take this measurements is AGILENT 4284A LCR METER available in IMEP-LAHC Grenoble laboratories. As it can be seen in the Fig.1, the non-linear drain function current model generated data is in excellent agreement with experimental data.

At low frequency, the capacitance model is reproduces from depletion to accumulation regime the measurement data very well as shown in Fig.2 .A good agreement between the experimental and model generated data is obtained at medium(1kHz) and high frequency(10kHz). This validates the capacitance model presented in this work.

3. Study of γ parameter

The γ study was carried out assuming the same OTFT device used for validate the compact capacitance model shown above. It analyzed the behavior of γ taking into account the Q_{CH} model and the accumulation regime of C_{TOT} existing after V_{GS}=20V.To analyze this, we vary the value of γ between 0 to 1, being them the typical values of this parameter in OTFTs.

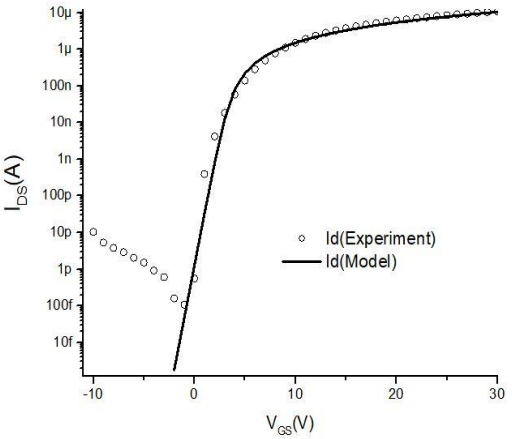

Fig.1. Modeled and experimental drain to source current (I_{DS}) as function of V_{GS}.

Firstly, Q_{CH} is analyze through two different studies. The first one, we took Q_{CH} model development above for later change γ between 0 to 1 in three different V_{GS} values.

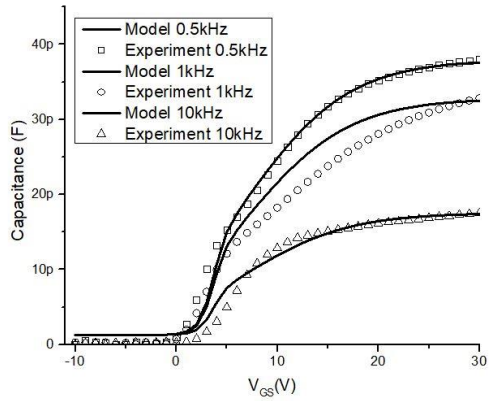

Fig.2. Modeled and experimental capacitance at low (500Hz), medium (1 kHz) and high (10 kHz) frequencies.

To analyze C_{TOT}, we plotted it in the accumulation regime vs γ parameter with different values of V_{GS}, in this case V_{GS}=20V, V_{GS}=25V and V_{GS}=30V. As you can see in Fig.3, when γ parameter is fixed, it do a affect in C_{TOT} in this way.

When the capacitance take the value of the dielectric capacitance (C_i) when V_{GS} reaches the accumulation regime. The ideal value of γ parameter in OTFTs is close to 0. We can note it because in γ=0 and γ=0.332 the capacitance hold on the same value.

4. Capacitance Derivative

We apply the first derivative to both our OTFT model and measurements features. The derivative was applied to OTFT capacitance data and the three targeted frequencies. Our model reproduces reasonably well the experimental results including the position of the observed two peaks.

In Fig.4, we analyzed the derivative of the gate capacitance at medium frequency (1 kHz). The agreement between model and experimental data is quite good, including the position of the two peaks

7. Conclusion

Our capacitance model reproduces a good agreement in all studies realized.

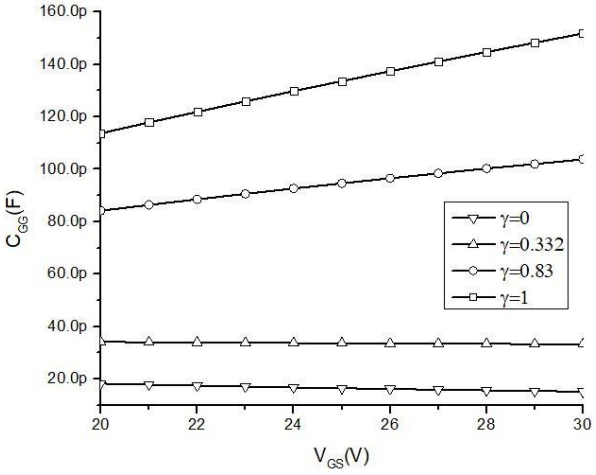

Fig.3. Gate capacitance vs V_{GS} with different γ

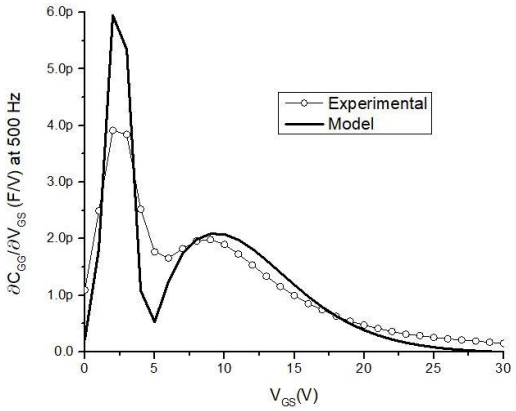

Fig.4. First derivative of C_{TOT} vs V_{GS} at 500 Hz.

References

[1] O. Marinov, M. J. Deen, and B. Iniguez, "Performance of Organic thin-film transistors," Journal of Vacuum Science & Technology B: Microelectronics and Nanometer Structures Processing, Measurement, and Phenomena, vol. 24, no. 4, pp. 1728–1733, 2006.

[2] M. Estrada, A. Cerdeira, J. Puigdollers, L. Resendiz, J. Pallares, L. Marsal, C. Voz, and B. Iniguez, "Accurate modeling and parameter extraction method for organic tfts," Solid-state electronics, vol. 49, no. 6, pp. 1009–1016, 2005.

[3] G. Horowitz and P. Delannoy, "An analytical model for Organic-based thin-film transistors," Journal of Applied Physics, vol. 70, no. 1, pp. 469–475, 1991.

[4] O. Marinov, M. Deen, and B. Iniguez, "Charge transport in organic and polymer thin-film transistors: recent issues," IEE Proceedings-Circuits, Devices and Systems, vol. 152, no. 3, pp. 189–209, 2005.

[5] E. Calvetti, L. Colalongo, and Z. M. Kovacs-Vajna, "Organic thin film transistors: a dc/dynamic analytical model," Solid-State Electronics, vol. 49, no. 4, pp. 567–577, 2005.

[6] M. Fadlallah, W. Benzarti, G. Billiot, W. Eccleston, and D. Barclay, "Modeling and characterization of organic thin film transistors for circuit design," Journal of applied physics, vol. 99, no. 10, p. 104504, 2006.

[7] L. Li, H. Marien, J. Genoe, M. Steyaert, and P. Heremans, "Compact model for organic thin-film transistor," IEEE Electron Device Letters, vol. 31, no. 3, pp. 210–212, 2010.

[8] A. Castro-Carranza, M. Estrada, J. C. Nolasco, A. Cerdeira, L. F. Marsal, B. Γn´ıguez, and J. Pallar`es, "Organic thin-film transistor bias-dependent capacitance compact model in accumulation regime," IET circuits, devices & systems, vol. 6, no. 2, pp. 130–135, 2012.

[9] A. Castro-Carranza, M. Estrada, A. Cerdeira, J. C. Nolasco, J. S´anchez, L. F. Marsal, B. Γniguez, and J. Pallar` es, "Compact capacitance model for otfts at low and medium frequencies," IEEE Transactions on Electron Devices, vol. 61, no. 2, pp. 638–642, 2014.

[10] T. Rudenko, R. Yu, S. Barraud, K. Cherkaoui, and A. Nazarov, "Method for extracting doping concentration and flat-band voltage in junctionless multigate mosfets using 2-d electrostatic effects," IEEE Electron Device Letters, vol. 34, no. 8, pp. 957–959, 2013.

[11] T. Rudenko, R. Yu, S. Barraud, K. Cherkaoui, P. Razavi, G. Fagas, and A. Nazarov, "On the mobility behavior in highly doped junctionless nanowire soi mosfets," in Advanced Materials Research, vol. 854. Trans Tech Publ, 2014, pp. 35-43.

[12] T. Rudenko, V. Kilchytska, N. Collaert, S. De Gendt, R. Rooyackers, M. Jurczak, and D. Flandre, "Specific features of the capacitance and mobility behaviors in finfet structures," in Solid-State Device Research Conference, 2005. ESSDERC 2005. Proceedings of 35th European. IEEE, 2005, pp. 85–88.

[13] T. Rudenko, A. Nazarov, I. Ferain, S. Das, R. Yu, S. Barraud, and P. Razavi, "Mobility enhancement effect in heavily doped junctionless nanowire silicon-on-insulator metal-oxide-semiconductor field-effect transistors," Applied Physics Letters, vol. 101, no. 21, p. 213502, 2012.

Effect of Schottky Barrier Contacts on Measured Capacitances in Tunnel-FETs

A. Farokhnejad[1,2,✠], M. Schwarz[1], M. Graef[1], F. Horst[1,2], B. Iñíguez[2], F. Lime[2] and A. Kloes[1]
[1]NanoP, TH Mittelhessen University of Applied Sciences, Giessen, Germany
[2]DEEEA, Universitat Rovira i Virgili, Tarragona, Spain
✠atieh.farokhnejad@ei.thm.de

***Abstract*—The influence of Schottky barriers at $NiSi_2$ contacts of Si Planar p-TFETs on Ultrathin Body [1] is analyzed in terms of deviations between measurements, TCAD simulations and a proposed compact model for the intrinsic capacitances in TFETs presented in [2]. A theory for the reason of the deviations for the intrinsic capacitances is evolved and discussed. Additionally, TCAD simulations are performed to support the theory.**

Keywords—Tunnel-FET; AC model; intrinsic capacitances; Schottky barrier; TCAD simulations.

I. Introduction

Recently tunnel field-effect transistors (TFET) are in the center of the attractions to be the surrogate of the standard MOSFET. This ever increasing interest owes to their feasibility to overcome the 60 mV/dec subthreshold slope limitation of the standard MOSFETs [3]. In order to perceive the working principle of TFETs and also making circuit simulations using multiple TFETs possible, simulations as well as models which show all aspects of the device are required.

In our previous work [2] a compact model for intrinsic capacitances in TFETs was introduced. Results were compared with measured data of a p-type fabricated device as well as TCAD simulations. In all measured data it could be seen that the gate-source capacitances (C_{gs}) in on-state increase and gate-drain capacitances (C_{gd}), after a certain bias start to decrease. In ambipolar-state same effect could be seen. That is to say, capacitances C_{gd} increase rather than stay steady and capacitances C_{gs} slightly sink (see Fig. 1).

It was expected by including the effect of parasitic resistances [4] and also voltage drop in the channel, this effect would be seen in the model as well. Actually, considering these effects has caused some changes in the correct direction but there is still room to improve it. Therefore, in this work the focus is exclusively laying on this effect and factors which give cause for increase and decrease of capacitances.

II. Small Signal Analysis including Schottky Contacts

In [2] to compensate the unexpected increase and decrease of capacitances, the effect of source and drain parasitic resistances is included in the model. Considering transconductance (g_m) and output conductance (g_{ds}) and their crucial influence on capacitances showed that the effect of parasitic resistances needs to be calculated for on and ambiplolar-state separately. In the measured TFETs $NiSi_2$ is used as contact material. Despite $NiSi_2$ has a mid-gap work function with respect to silicon, high doping of the semiconductor should result in an ohmic contact due to tunneling of carriers through the Schottky barrier (see Fig. 2). But at drain side the doping in TFET often is reduced to suppress the ambipolar current. This lowers the small signal conductance of the contact. Because the tunneling barrier in the TFET is the bottleneck for the current, having a voltage drop of nearly V_{ds}, the voltage across the Schottky barriers at the contacts is almost zero. At this bias the small signal conductance of the Schottky barrier can come into the same order of magnitude as g_m and g_{ds} of the TFET (see Fig. 3).

In on-state it is assumed $C_{gd} >> C_{gs}$. Furthermore, analytical calculations based on the results in [2] and [4] show, that the main impact comes from the drain, therefore the focus in a first attempt is set on the drain Schottky barrier. Considering this assumption, the capacitances affected by parasitic resistances in on-state are defined as

$$C'_{gd} = C_{gd} - C_{gd}\frac{g_{ds}}{g_d} \tag{1}$$

$$C'_{gs} = C_{gs} + C_{gd}\frac{g_m}{g_d}. \tag{2}$$

g_d represents the parasitic small signal conductance of Schottky barrier at drain terminal (see Fig. 2).

TCAD simulations of a TFET structure including two Schottky barriers at source and drain showed poor convergence. However, during the study of this effect convergence has been improved slightly and a few results have been won. They show results which are offering a tendency, but not in total agreement with the theory and analytics. Nevertheless, to calculate g_d, Schottky diodes for a low bias with different drain doping concentrations have been simulated in TCAD. Comparing the resulted current with measured data showed that the current flowing In Schottky diode with drain doping lower than $1 \times 10^{19} cm^{-3}$ is in the same range as in the p-type TFET (see Fig. 3). The transconductance and output conductance are calculated as

$$g_m = \frac{\partial I_{ds}}{\partial V_{gs}} \qquad g_{ds} = \frac{\partial I_{ds}}{\partial V_{ds}}. \tag{3}$$

In ambipolar-state it is assumed that $C_{gs} >> C_{gd}$ and g_s is the parasitic small signal conductance of Schottky barrier at source terminal.

$$C'_{gd} = C_{gd} + C_{gs}\frac{g_m}{g_s} \tag{4}$$

$$C'_{gs} = C_{gs} - C_{gs}\frac{g_{ds}}{g_s}. \tag{5}$$

III. VERIFICATION AND CONCLUSION

The pattern which measured TFET capacitances show are not visible in TCAD simulations without Schottky barriers at source/drain (dotted curves in Fig. 4.c). So, it is assumed parasitic small signal resistances of Schottky barriers at source and drain have effect on intrinsic capacitances. This assumption has led to eq. (1), (2), (4) and (5). Regarding the Schottky diode simulations shown in Fig. 3, it is considered $g_d = 1e^{-6}(\Omega\mu m)^{-1}$.

To verify this theory, current curves of a Double-Gate n-TFET are simulated in TCAD and from them g_m as well as g_{ds} corresponding to each drain voltage are calculated. C_{gd} and C_{gs} in the on-state are obtained from AC simulations. Considering the effect of Schottky barrier C'_{gd} and C'_{gs} are calculated by applying eq. (1) and (2) and compared with the corresponding simulations without the consideration of Schottky barrier and the result is depicted in Fig. 4.

By including the effect of Schottky barrier on capacitances, C'_{gd} decreases and C'_{gs} increases. At $V_{ds} = 0.1$ V decrement in C'_{gd} is stronger than at $V_{ds} = 0.3$ V and it is similar to what measurements show. The reason is that for smaller V_{ds}, as it is shown in Fig. 4.b, g_{ds} has higher value and therefore, parasitic small signal resistances of Schottky barrier affect C_{gd} stronger.

It can be seen, including the effect of Schottky barrier on capacitances, simulations are improved and show a similar pattern as in measured data.

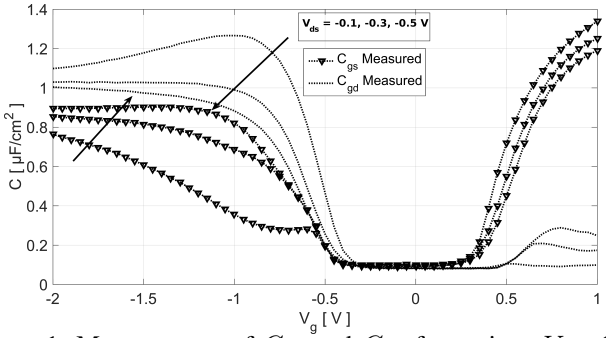

Figure 1: Measurement of C_{gs} and C_{gd} for various V_{ds}. C_{gs} of p-type device in its on-state increases as well as C_{gd} in ambipolar-state.

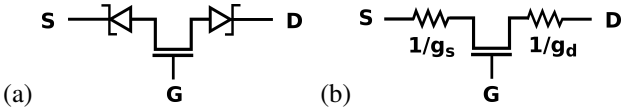

Figure 2: Schematic of p-type device a) considering Schottky diodes and b) small signal conductances of Schottky barriers at source and drain.

ACKNOWLEDGMENTS

This project was supported by the German Federal Ministry of Education and Research under contract No. FKZ 13FH010IX5 and Spanish Ministry of Economy and Competitiveness through project GREENSENSE TEC2015-67883- R. We would like to thank Keysight Technologies for the license donation and support of the software IC-CAP and AdMOS GmbH for support. We also thank FZ Juelich, PGI9-IT for their cooperation and providing us measurements data.

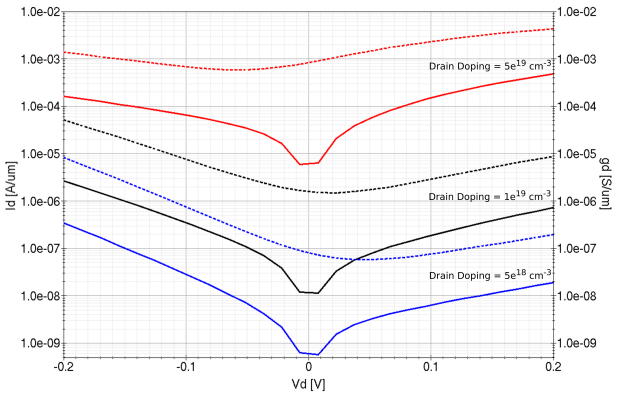

Figure 3: Schottky diodes to estimate the small signal conductance of the Schottky barriers at source/drain of TFET are simulated. Solid lines show the current as a function of the voltage across the Schottky barrier. Dotted curves represent the small signal conductance of corresponding diodes.

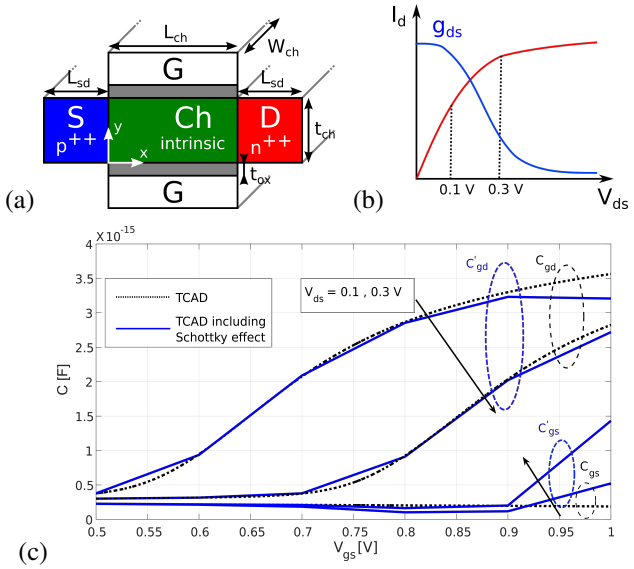

Figure 4: a) Double-Gate n-type TFET structure in TCAD. b) Sketch of the output characteristic and g_{ds}. c) TFET Capacitances simulated in TCAD. Blue solid lines show simulations including Schottky barrier effect. $L_{ch} = 22$ nm, $t_{ch} = 10$ nm, $W_{ch} = 1$ μm and $t_{ox} = 2$ nm. Oxide material is HfO_2.

REFERENCES

[1] C. Liu, Q. Han, S. Glass, G. V. Luong, K. Narimani, A. T. Tiedemann, A. Fox, W. Yu, X. Wang, S. Mantl, *et al.*, "Experimental I–$V(T)$ and C–V Analysis of Si Planar p-TFETs on Ultrathin Body," *IEEE Transactions on Electron Devices*, vol. 63, no. 12, pp. 5036–5040, 2016.

[2] A. Farokhnejad, M. Graef, F. Horst, C. Liu, Q. Zhao, B. Iñíguez, F. Lime, and A. Kloes, "Compact modeling of intrinsic capacitances in double-gate tunnel-fets," in *Ultimate Integration on Silicon (EUROSOI-ULIS), 2017 Joint International EUROSOI Workshop and International Conference on*, pp. 140–143, IEEE, 2017.

[3] A. C. Seabaugh and Q. Zhang, "Low-Voltage Tunnel Transistors for Beyond CMOS Logic," *Proceedings of the IEEE*, vol. 98, no. 12, pp. 2095–2110, 2010.

[4] T. Smedes and F. Klaassen, "Influence of Channel Series Resistances on Dynamic MOSFET Behaviour," *Solid-State Electronics*, vol. 37, no. 2, pp. 251–254, 1994.

Inkjet Printed ZnO Layer for Polymer Based Organic Solar Cells Applications

J. G. Sánchez[a], V. S. Balderrama[b], S. I. Garduño[c], E. Osorio[d], A.Viterisi[a], M.Estrada[e], J. Ferré-Borrull[a], J. Pallarès[a]* and L. F. Marsal[a]*

[a]Departament d'Enginyeria Electrònica Elèctrica i Automàtica, Universitat Rovira i Virgili, 43007 Tarragona, Spain.
[b]Cátedra-CONACYT, Center for Engineering and Industrial Development, 76125 Querétaro, México.
[c]Cátedra-CONACYT, Centro de Investigación y de Estudios Avanzados del I.P.N, 07360 Ciudad de México, México.
[d]Cátedra-CONACYT, Universidad de Quintana Roo, División de Ciencia e Ingeniería. 77019, Quintana Roo, México.
[e]Centro de Investigación y de Estudios Avanzados del I.P.N, 07360 Ciudad de México, México.
Corresponding authors e–mail: lluis.marsal@urv.cat and josep.pallares@urv.cat

Abstract

We studied the effects of zinc oxide (ZnO) layers deposited by inkjet printing (IJP) on the performance of inverted polymer solar cells based on Poly[4,8-bis(5-(2-ethylhexyl)thiophen-2-yl)benzo[1,2-b;4,5b']dithiophene -2,6-diyl-alt-(4-(2-ethylhexyl)-3-fluorothieno[3,4-b]thiophene-)-2-carboxylate-2-6-diyl)]thieno[3,4-b]-thiophene/benzodithiophene (PTB7-Th) and the [6,6]-phenyl-C71-butyric acid methyl ester ($PC_{70}BM$). Similar devices were fabricated with ZnO layer deposited by different techniques for comparison. All devices were characterized by electrical and photophysical methods. The results show that non-geminate recombination in devices with ZnO-IJP is governed by deep trap states. Moreover, the electron injection and extraction have an influence on the shunt resistance of these devices. The performance of device made with ZnO-IJP compare very favourably with that of devices made from ZnO layer deposited using different techniques.

1. Introduction

Polymer solar cells (PSCs) have been extensively studied due to their low cost and large scale fabrication.[1,2] In the last years, PSCs with inverted architecture (iPSCs) have attracted much attention due to they are a promising long-lasting alternative to improve the stability of PSCs.[3] In iPSCs, metal oxide such as molybdenum oxide, vanadium oxide, nickel oxide or tungsten oxide are used as hole transport layer due to they provide a lower ohmic contact resistance.[4] On the other hand, the poly [(9,9-bis (30-(N,N-dimethyl-amino)propyl)-2,7-fluorene)-alt-2,7-(9, 9-dioctylfluorene)] (PFN), zinc oxide and titanium oxide, and are used as the electron transport layer.[5] Among these, zinc oxide (ZnO) has attracted much interest due to its high transparency, high air-stability, high electron mobility, and the possibility to be deposited from a solution at room temperature by several coating methods.[6] Spin-coating is the most commonly used method of thin-film deposition since it yields films with relatively high uniformity and well-controlled thickness. Nonetheless, this deposition technique is not compatible with large-scale continuous process such as roll-to-roll (R2R) processing. On the other hand, inkjet printing (IJP) is a very promising technique for the large-scale production of i-PSCs and commercialization due to its compatibility with R2R process, the possibility of patterning without any chemical processes (i.e. wet etching of photoresist) and the reduction of material (solution) wasting.[7] Herein we describe the fabrication and electrical characterization of ZnO-IJP layers as ETL for iPSCs. The iPSCs devices were based on active layers composed of PTB7:Th and $PC_{70}BM$. Similar devices were fabricated with ZnO as ETL deposited by spin coating (ZnO-SC) and thermal evaporation (ZnO-TE) as control. The results of photophysical measurements combined with ideality factor analysis demonstrated that recombination kinetics are governed by different mechanisms in IJP-made devices with respect to SC and TE–made devices. Impedance Spectroscopy results reveal that devices made from ZnO-IJP exhibit a similar charge transport resistance compared to devices with ZnO-SC, while devices with ZnO-TE show the highest charge transport resistance.

2. Experimental and Results

The iPSCs were fabricated on indium tin oxide (ITO) glass substrates with a nominal shhet resistance of 10 Ω/□.The substrates were cleaned in acetone, ethanol and isopropanol using an ultrasonic bath and dried at 100 °C followed by UV-ozone treatment. Subsequently, the ITO substrates were coated with ZnO (~40 nm) by either inkjet printing, spin coating or thermal evaporation as described above. The blend solution was prepared by dissolving PTB7-Th and $PC_{70}BM$ (1:1.5

w/w) in chlorobenzene and 1,8-diiodooctane (97:3 by volume) with a concentration of 25 mg mL-1. The blend solution was left stirring overnight, and further aged for 48h in the dark under nitrogen atmosphere. The blend solution was spin-coated on top of ZnO at 800 rpm for 30 s to obtain an active layer 100 nm-thick. The samples were transferred to a vacuum chamber and 5 nm of V_2O_5 and 100 nm of Ag were deposited by thermal evaporation on top of the active layer at $7x10^{-7}$ mbar. The active area for all devices was 9 mm^2. Figure 1 shows the normalized open circuit voltage (V_{OC}), short circuit current density (J_{SC}), fill factor (FF) and power conversion efficiency (PCE) of iPSCs with ZnO-IJP, ZnO-SC and ZnO-TE as ETL. The devices made from ZnO-IJP show the highest V_{OC}, while the devices with ZnO the lowest one. Devices with ZnO-SC exhibit the highest J_{SC}, FF and PCE. The PCE and JSC of iPSCs with ZnO-IJP is ~20% less than those of devices with ZnO-SC. Devices with ZnO-IJP and ZnO-SC exhibit similar FF. Figure 2 shows the resistance data extracted from the fitting of IS measurements for devices using ZnO-IJP, ZnO-SC and ZnO-TE. The resistances values of ZnO is similar in iPSCs with ZnO-IJP and ZnO-SC. In both devices, the resistance decreases as the applied voltage increases. These high values of resistance at low voltages (from 0 V to 0.2 V) suggest that shunt resistance losses are mainly caused by the hole- and electron-transport layers. Moreover, at high voltages (from 0.7 V to 1 V) the ZnO layer of iPSCs with ZnO-IJP and ZnO-SC exhibit lower resistance values that that of devices with ZnO-TE.

3. Conclusions

In this work, we investigated the use of an inkjet printed ZnO layer as ETL in iPSCs based on PTB7-Th:$PC_{70}BM$. The performance of iPSCs compares very favourably to that obtained on similar iPSCs using spin coated and thermally evaporated ZnO layers. Photophysical studies has brought substantial evidence of a modification of the band structure properties of the active layer, triggered by the ZnO type of under-layer the active layer is deposited on to. As such, the active layer deposited on top of ZnO-IJP shows a higher density of deep trap states, than those deposited on top of ZnO-SC and ZnO-TE. Additional impedance spectroscopy measurements have demonstrated that electron injection and extraction have an impact on the shunt and series resistances of the ZnO-IJP-made and ZnO-TE-made devices, thus lowering the FF of both devices slightly. All in all, this study demonstrates that the ZnO-IJP layer deposited by inkjet printing can be successfully used for the fabrication of highly efficient i-PSCs on a large scale.

Acknowledgements

This work was supported by the Spanish Ministry of Economy, Industry and Competitiveness (MEIC) for grant numbers, TEC2015-71915-REDT and TEC2015-71324-R (MINECO/FEDER), by the ICREA for the ICREA Academia Award, by the Catalan authority for project AGAUR 2017 SGR 1527 and the CONACYT Project 237213 in Mexico.

Figure 1 Normalized V_{OC}, J_{SC}, FF and PCE of iPSCs with ZnO-IJP (orange), ZnO-SC (purple) and ZnO-TE (blue) used as ETL. Inset: The architecture of fabricated devices.

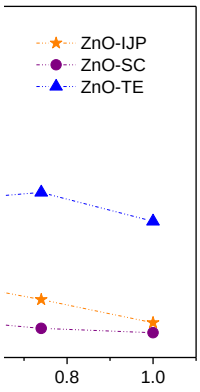

Figure 2 Resistance data extracted from the fitting of IS measurements for devices using ZnO-IJP (stars), ZnO-SC (circles) and ZnO-TE (triangles).

References

[1] V. S. Balderrama, F. Avila-Herrera, J. G. Sanchez, J. Pallares, O. Vigil-Galan, L. F. Marsal, and M. Estrada, *IEEE J. Photovoltaics*, 6, 2, 491–497, 2016.

[2] V. S. Balderrama, M. Estrada, P. L. Han, P. Granero, J. Pallarés, J. Ferré-Borrull, and L. F. Marsal, *Sol. Energy Mater. Sol. Cells*, 125, 155–163, 2014.

[3] J. G. Sánchez, V. S. Balderrama, M. Estrada, E. Osorio, J. Ferré-Borrull, L. F. Marsal, and J. Pallarès, *Sol. Energy*, 150, 147–155, 2017.

[4] J. Meyer, S. Hamwi, M. Kröger, W. Kowalsky, T. Riedl, and A. Kahn, *Adv. Mater.*, 24, 40, 5408–5427, 2012.

[5] R. C. I. MacKenzie, V. S. Balderrama, S. Schmeisser, R. Stoof, S. Greedy, J. Pallarès, L. F. Marsal, A. Chanaewa, and E. von Hauff, *Adv. Energy Mater.*, 6, 4, 1501742, 2016.

[6] J D. Lee, T. Kang, Y. Choi, S. Oh, *J. Phys. Chem. Solids*, 105, 66-71, 2017.

[7] M. Singh, H. M. Haverinen, P. Dhagat, and G. E. Jabbour, *Adv. Mater.*, 22, 6, 673–685, 2010.

Relation of empirical parameters in the UMEM mobility model with a-IGZO TFT physical parameters

Y. Hernández-Barrios[1], A. Cerdeira[1], M. Estrada[1], B. Iñiguez[2]

[1]SEES, Depto. de Ingeniería Eléctrica, CINVESTAV-IPN, Av. IPN 2208, CP 07360, México City, México.
[2] Departament d'Enginyeria Electrònica, Elèctrica i Automàtica (DEEEA), Universitat Rovira i Virgili, 43007 Tarragona, Spain.

Abstract

The empirical parameters used in the mobility UMEM model for amorphous thin film transistor are related with physical device parameters considering an effective carrier density that takes into account the effect of the free and localized charge. An approximate expression to represent the variation of the surface potential with the gate voltage is presented and validated using numerical solutions. Using this expression, the UMEM mobility empirical parameters μ_o and V_{AA}, calculated as μ_{oc} and $V_{AAc,}$ are expressed through device physical parameters, the gate voltage (V_f) at which the Fermi level reaches the bottom is also calculated. Results were validated with fabricated a-IGZO TFTs.

1. Introduction

The first amorphous oxide semiconductor thin film transistor (AOSTFT) was presented by Nomura et al., in 2004 [1].

There are several publications associated to the study of the a-IGZO band structure and the distribution of localized states (DOS), concluding that the localized states in a-IGZO is usually less than $1x10^{20}$ $cm^{-3}eV^{-1}$ depending of the technology used [2-6].

At the same time, the Unified Model and Extraction Method (UMEM) has been proven to model satisfactorily these devices [7].

In this work, we found the relation of UMEM empirical parameters for modeling the mobility for the case of a-IGZO TFTs, when the free carrier charge can be in the order or greater than the localized and the approximations used for a-Si:H cannot be used [8].

2. Calculation of parameters used in the analysis

To obtain the analytical expressions to associate the mobility model empirical parameters with physical parameters of the devices, first, we solved numerically the free carrier, using the Boltzmann statistics.

$$n_{free}(\varphi_s) = N_C \cdot e^{\frac{\varphi_s - \varphi_f}{\varphi_t}}, \qquad (1)$$

where N_C is the effective density of states in the conduction band, φ_f is the Fermi potential and φ_t is the thermal potential:

Form [8], we used and calculated numerically, the expression for the localized carrier density, for the case when the characteristic temperature T_t is above 300 K (i.e. tails in a-IGZO):

$$n_{loc}(\phi_s) = g_{ato}\phi_{tt} e^{\frac{\phi_s - \phi_f}{\phi_{tt}}} e^{\frac{\phi_s - \phi_f}{\phi_{tt}}} \int_0^{} \frac{1}{1 + z^{\frac{T_t}{T}}} dz \qquad (2)$$

At the same time, the effect of the free and localized carrier densities was represented as an effective carrier density as follows:

$$n_{total}(\phi_s) = n_{free}(\phi_s) + n_{loc}(\phi_s) = N_{eff} e^{\frac{\phi_s - \phi_f}{\phi_{eff}}}, \qquad (3)$$

The following equation is an empirical expression to represent the variation of the surface potential with the gate voltage, which was validated with the numerical calculations, see Fig. 1:

$$\phi_s = 2\phi_{eff} \ln\left[\frac{C_{ox}}{\sqrt{2q\varepsilon_s N_{eff}\phi_{eff} e^{\frac{-\phi_f}{\phi_{eff}}}}} (V_g - V_t) \right] \qquad (4)$$

The next equation is the field effect mobility defined in [8], but in this case, we define it using the effective carrier density as:

$$\mu_{FEc} = \mu_{0c}\left[\frac{n_{free}(\phi_s)}{n_{tot}(\phi_s)}\right] = \mu_{0c}\left[\frac{(N_C / N_{eff})^{\frac{1}{\gamma}} C_{ox}}{\sqrt{2q\varepsilon_s N_{eff}\phi_{eff}}}\right]^{\gamma} (V_g - V_t)^{\gamma} \qquad (5)$$

where the UMEM γ parameter is extracted using:

$$\gamma = 2\left(T_{eff} / T - 1\right), T_{eff} = (T + T_t)/2 \qquad (6)$$

Substituting (6) in (5) and comparing (5) with the expression for mobility used in UMEM, the parameter V_{AA} can now be calculated as:

$$V_{AAc} = \frac{\sqrt{2q\varepsilon_s N_{eff}\phi_{eff}}}{(N_C / N_{eff})^{\frac{1}{\gamma}} C_{ox}} \qquad (7)$$

where q is the electron charge, ε_s is the a-IGZO dielectric constant and C_{ox} is the capacitance per unit

area of the dielectric.

After calculating V_{AAc}, the expression for mobility in UMEM, when V_g-V_t=1, can be equated to:

$$\mu_1 = \mu_0 / V_{AA}^{\gamma} = \mu_{0c} / V_{AAc}^{\gamma} \quad (8)$$

and the value of μ_{0C} can be calculated from (8).

Finally, the V_f gate voltage, can be calculated using (4) and (7) as:

$$V_f = \frac{\sqrt{2q\varepsilon_s N_{eff}\phi_{eff}}}{C_{ox}} + V_t = V_{AAc}\left(N_C / N_{eff}\right)^{\frac{1}{\gamma}} + V_t, \quad (9)$$

where V_t is the threshold voltage.

Fig. 1 shows that, in the region where the gate voltage is near or above V_f, the approximated expression (4) fits very well the calculation of the surface potential using the complete numerical calculation.

3. Results

Parameters	Device 1.	Device 2.
W (µm)	900	80
L (µm)	30	40
t_{ox} (nm)	200	90
ε_i	5.2	20
ε_s	9	9
C_{ox} (nF/cm^2)	23	197
V_t (V)	-0.219	4.61
γ	0.49	0.52
φ_f (mV)	125	65
g_{ato} (cm^{-3})	1.6x10^{19}	1.66x10^{19}
T_t (K)	445	457
T_{eff} (K)	373	378
μ_1 (cm^2/Vs)	2.2	2.1
V_f (V)	7.9	5.6
N_{eff} (cm^{-3})	4.28x10^{18}	4.32x10^{18}
V_{AAc} (V)	5.87	0.73
μ_{oc} (cm^2/Vs)	5.1	1.75

Table 1. Geometrical, physical and extracted parameters of the devices, using the presented procedure.

Fig .1. Surface potential vs. gate voltage, calculated using the empirical expression (4), as well as calculated numerically, using the total carrier density and the effective carrier density (3).

4. Conclusions

An analysis to relate the UMEM mobility model parameter μ_{0C} and V_{AAc} with physical device parameters for a-IGZ, is presented. An approximated expression to reproduce the variation of the surface potential on the gate voltage is presented. This expression as well as the representation of the total charge density as an effective charge density allows to calculate the above mentioned model parameters. A simple expression to determine V_f is also presented.

Acknowledgements:

This work was supported by Conacyt projects 237213 and 236887 in Mexico, the H2020 program of the European Union under contract 645760 (DOMINO), by contract “Thin Oxide TFT SPICE Model” (T12129S) with Silvaco Inc., by ICREA Academia 2013 from ICREA Institute and the Spanish Ministry of Economy and Competitiveness through project TEC2015-67883-R (GREENSENSE).

References

[1] Nomura K, et.al Room-temperature fabrication of transparent flexible thin-film transistors using amorphous oxide semiconductors. Nature 2004; 432, 488.

[2] Kamiya T, Nomura K, Hosono H. Electronic structure of the amorphous oxide semiconductor a-InGaZnO4-x: Tauc-Lorentz optical model and origins of subgap states. Phys. Status Solidi A 206 2009; 5, 860.

[3] Kamiya T, Hosono H. Material characteristics and applications of transparent amorphous oxide semiconductors. NPG Asia Mater. 2010; 2, 15.

[4] Jeong J, et.al. Meyer-Neldel Rule and Extraction of Density of States in Amorphous Indium-Galium-Zinc-Oxide Thin-Film Transistor by Considering Surface Band Bending. Japanese Journal of Applied Physics 2010; 49, 03CB02.

[5] Kim S.C, Kim Y.S, Kanicki J. Density of states of short channel amorphous In–Ga–Zn–O thin-film transistor arrays fabricated using manufacturable processes. Jpn. J. of Appl. Phys. 2015; 54, 051.

[6] Sallis S, et.al. Origin of deep subgap states in amorphous indium gallium zinc oxide: Chemically disordered coordination of oxygen. Applied Physics Letters 2014; 104, 232108.

[7] Cerdeira A, Estrada M, Garcia R, Ortiz-Conde A, Garcia-Sanchez F.J. New Procedure for the extraction of basic a-Si:H TFT model parameters in the linear and saturation regions. Solid State Electronics 2011; 45, 1077.

[8] Shur M, Hack M. Physics of amorphous silicon based alloy field-effect-transistors. Journal of Applied Physics 1984; 55, 3831-3842

Gas sensing properties of carbon nanotubes decorated with iridium oxide nanoparticles

J. Casanova-Cháfer, E. Navarrete and E. Llobet

MINOS-EMaS, Universitat Rovira i Virgili, 43007, Tarragona, Spain

1. Abstract

The properties of Iridium oxide (IrO_2) decorated Multi-Wall Carbon Nanotubes (IrO_2-MWCNTs) are studied for detecting nitrogen dioxide and ammonia vapors. IrO_2 nanoparticles were synthetized using a hydrolysis and acid condensation growth mechanism, and subsequently employed for decorating the sidewalls of carbon nanotubes. Decorated MWCNTs films were deposited onto SiO_2/Si substrates for achieving chemoresistive gas sensors. NO_2 and NH_3 gases were detected under different experimental conditions. Higher and more stable responses towards NH_3 and NO_2 were observed for iridium-oxide nanoparticle decorated MWCNT material, compared to bare MWCNT material. Raman Spectroscopy was employed to study the nanomaterials and the optimal operating temperatures were determined.

2. Introduction

Carbon nanotubes were discovered by Sumio Iijima in 1991 and since then, this material has been widely used in chemoresistive gas sensors due to their remarkable sensitivity towards chemicals present in the local environment. Carbon nanotubes present suitable properties to be used in gas sensing applications due to their electronic, physical and chemical properties, such as high surface area to volume ratio, nanometer-sized and high carrier mobility. However, some sensing properties (e.g. sensitivity, selectivity and reproducibility) can be enhanced by the functionalization of their external sidewalls. Different options are well-known, such as grafting functional groups onto the carbon nanotubes surface or decorating them with metal or metal oxide nanoparticles. Here we explore the improvements obtained by loading MWCNTs with IrO_2 nanoparticles. While the use of IrO_2 has been reported for electrochemical sensing and catalysis, little information is available on its use for chemoresistive gas sensing.

3. Material characterization

Iridium oxide (IrO_2) nanoparticles were synthetized using the method proposed by Zhao[1] and attached onto MWCNTs surface via an impregnation technique. MWCNTs had undergone a cold plasma treatment to graft carbonyl and carboxyl functional groups to their surface. This helps attaching iridium oxide nanoparticles to nanotubes. Raman measurements revealed the MWCNTs decoration with IrO_2 (Figure 1), showing the well-known CNTs bands (D, G, 2D, 2iTO) and the IrO_2 active modes (E_g, B_{2g} and A_{1g}) previously reported in other works[2].

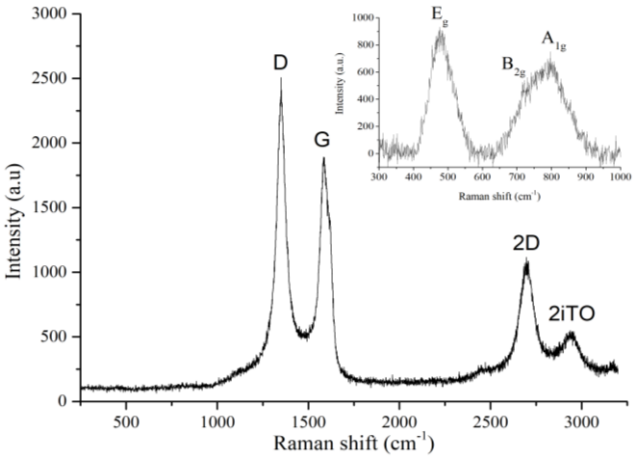

Figure 1. Raman spectra of MWCNTs with a zoom in the 300-1000 cm^{-1} region (in the inset) corresponding to iridium oxide nanoparticles.

4. Gas sensing results

NH_3 and NO_2 gas sensing measurements were performed at ppm and ppb levels, respectively, showing a suitable, improved sensitivity, stability and reproducibility of the response (see Figure 2) for iridium oxide doped MWCNTs. In case of NH_3 detection, a significant increase in response (6-fold) for doped MWCNTs was observed.

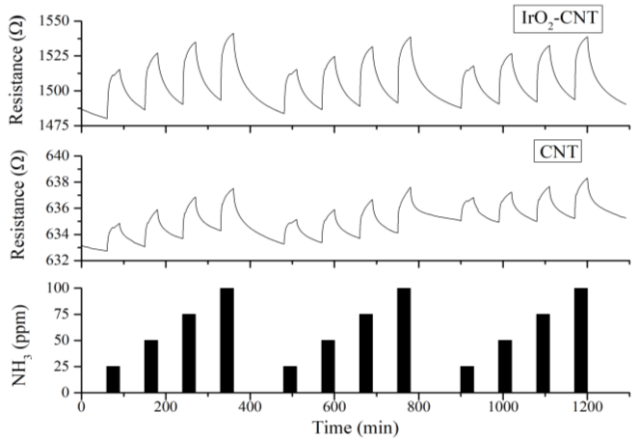

Figure 2. Example of the resistance response obtained for NH_3 detection at 100ºC. It can be observed The higher response, better reproducibility and higher stability of IrO_2-MWCNT can be observed.

In addition, different temperatures were tested, and while IrO_2-MWCNTs presented higher response than bare MWCNTs for all the temperatures studied, the best operating temperature was found to be 100ºC. (Figure 3).

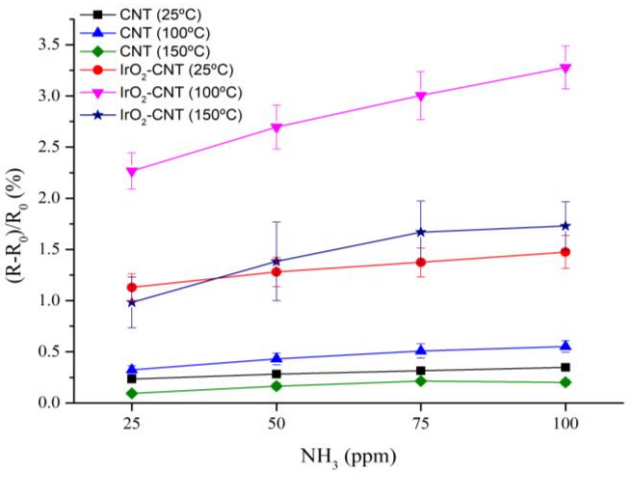

Figure 3. Response obtained for 25, 50, 75 and 100 ppm of NH_3 at room temperature, 100 and 150ºC. The graph shows a higher response for IrO_2-MWCNTs material for every temperature tested. The best operating temperature was 100ºC for both, doped and undoped MWCNTs.

Moreover, it can be observed that a better sensitivity towards ppb levels or NO_2 (2-fold increase) was obtained for IrO_2-MWCNTs. The optimal NO_2 detection temperature was 150ºC (see Figure 2b). Additional characterization results that are currently underway will be shown, including TEM imaging of IrO_2-MWCNTs, the study of the detection of additional gas species and the effect of ambient moisture on sensor response.

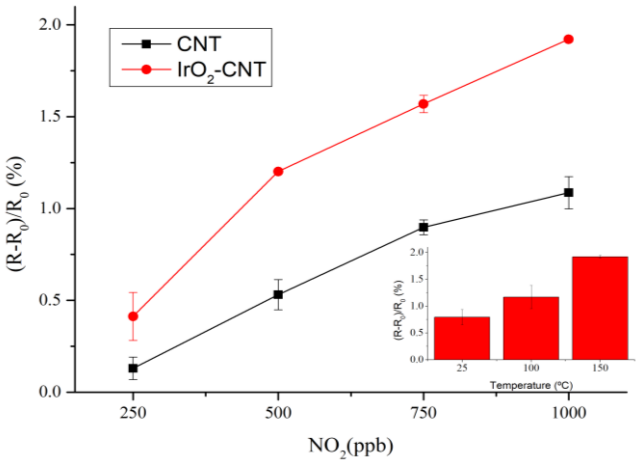

Figure 4. NO_2 gas sensing results. IrO_2-MWCNTs result in enhanced response. The best operating temperature was 150ºC because the inset indicates that the highest response was observed at this temperature.

4. Conclusions

Our MWCNTs decorated with iridium oxide nanoparticles showed an enhanced gas sensing mechanism based on charge transfer between the metal oxide nanoparticle-carbon nanotube system upon the adsorption of gas molecules, especially to NH_3. In addition, different operating temperatures were tested, demonstrating that 100ºC is the best temperature to detect NH_3 based on higher chemical interactions between the doped IrO_2-MWCNTs and the gas molecules, meanwhile 150ºC have been show the best operating temperature to detect NO_2.

5. References

[1] Y. Zhao, "A high yield synthesis of ligand-free iridium oxide nanoparticles with high electrocatalytic activity", JPCL, pp. 402-406, 2011.

[2] A.V. Korotcov, "Raman scattering characterization of well-aligned RuO2 and IrO2 nanocrystals", J. Raman Spectrosc., pp. 737-749, 2007.

Electropolishing 1100 Aluminum Alloy for Solar Concentrators

Sara María Aguilar-Sierra[1*], Félix Echeverría E[1]

Centro de Investigación, Innovación y Desarrollo de Materiales – CIDEMAT, Universidad de Antioquia UdeA, Calle 70 No. 52-21, Medellín, Colombia
E mail: felix.echeverria@udea.edu.co *tel: (+574) 2196615 fax: (+574) 2191051*

Abstract

Aluminum sheets-based mirrors have been used in solar concentrating technologies due to its high mechanical properties, low density and low cost. Nonetheless, the reflectance percentages obtained by electropolishing aluminum alloys are not close to the reflectance values of the currently used evaporated films. Therefore, controlling key factors affecting electropolishing processes became essential in order to achieve highly reflective aluminum surfaces. This study investigated the effect of both the electropolishing process and previous heat treatment on the total reflectance of the AA 1100 aluminum alloy. An acid electrolyte and a modified Brytal process were evaluated. Total reflectance was measured by means of UV–Vis spectrophotometry. Reflectance values higher than 80% at 600 nm were achieved for both electrolytes. Optical microscopy and scanning electron microscopy images were used to microstructural characterization. The influence of heat treatment, previously to electropolishing, was tested at two different temperatures and various holding times. It was found that reflectance increases around 15% for the heat-treated and electropolished samples versus the non-heat-treated ones.

1. Introduction

The most used reflective surfaces for solar mirrors are made of either silver back low-iron glass or aluminum [1]. Glass is heavy and fragile and has environmental issues and pure aluminum exhibits high reflectance percentages but has poor structural properties. An aluminum alloy provides the needed mechanical properties at expenses of its reflectance and therefore, commonly requires a coating in order to improve its optical properties, adding labor costs. A low alloyed aluminum such as AA1100 can be considered as an alternative low-cost solution for solar mirrors by improving its reflective properties that can be achieved by means of electropolishing processes [2], [3].

Electrolytic polishing is used in order to obtain smooth and bright surfaces. In the case of aluminum, some suitable electrolytes polishing include those composed by acids such as perchloric acid, phosphoric acid, sulfuric acid, chromic acid, mixture of acids and also salts [4]. Also, there are the alkaline electrolytes and those composed for methanol and nitric acid [5].

Otherwise, it has also been well established that in order to obtain a smooth and reflective surface, it is necessary to consider metallurgical factors such as size and orientation of grains and chemical compositions that can lead to a multiple phase metal. In this paper, spectrophotometry UV-Vis, profilometry, SEM and EDS have been used to investigate the conditions under which the electropolishing process of the AA1100 aluminum alloy is improved and a high total reflectance is obtained, making practical its use for solar thermal applications.

2. Experimental Procedure

Commercial sheets of AA 1100 were used. Two electropolishing processes were evaluated. The acid bath consisted of 70 v/v sulfuric acid, 15 v/v phosphoric acid, 1 v/v nitric acid and 14 v/v distilled water [6]. The alkaline bath was composed by trisodium phosphate (150 g/l), aluminum sulphate (20 g/l) and sodium hydroxide (10 g/l) [7]. The total reflectance of electropolished samples was determined on at least three specimens of each condition by UV-Vis spectroscopy, using a Cary 100 spectrophotometer with integration sphere with an 8° edge.

The electropolished surface roughness was measured by profilometry using a DEKTAK XT (Bruker) profilometer.

To evaluate the effect of the heat treatment holding time on the reflectance of the electropolished samples, the aluminum samples were heat treated at 500 °C during 5 min, 15 min, 30 min, 1 h, 2 h, 4.5 h, 7.5 h and 14 h and then electropolished under the same conditions for 15 minutes using modified Brytal process. Additionally, a set of samples was heat treated at 345 °C for 5 minutes, in order to obtain a finer grain

structure. The microstructural characterization and the electropolished surfaces were observed by means of optical microscopy (OM) and scanning electron microscopy (SEM). The reflectance percentage of previously heat-treated electropolished samples was measured as described above.

3. Results and Discussion

Microstructural and superficial characteristics of the electropolished samples have a direct influence on reflectance response as it can be observed from Figure 1 where the total reflectance (R_T) curves of samples electropolished in both acid and modified Brytal electrolytes with and without previous heat treatment are illustrated. Curves corresponding to non-heat-treated samples for both electrolytes showed reflectance percentages around 70% in the visible range lower than those obtained for the samples previously heat-treated that were around 84%. The textured surfaces obtained after electropolishing non-heat-treated aluminum were generated probably due to second-phases acting as stress concentrators, making their surroundings more susceptible to dissolution and then leading to particle detachment.

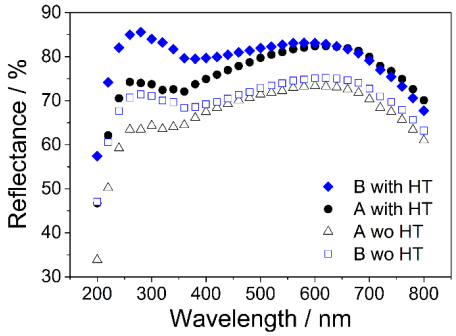

Fig.1. R_T spectra of samples with and without (wo) previous HT electropolishing in both acid (10 A/dm^2, 15 min) and modified Brytal (3 V, 15 min) electrolytes. A: Acid electrolyte and B: Modified Brytal process.

Figure 2 shows reflectance curves for samples with different heat treatments (HT) and electropolished in the Brytal electrolyte. These results reveal a clear increase in reflectance percentage of around 15% for heat-treated samples with respect to the untreated one. It also can be noted that HT either at lower temperature or with shorter holding times lead to higher reflectance of the aluminum surfaces after electropolishing. The amount of scattered and absorbed light by the surface is directly related to the number and size of those second-phase particles. Then, samples with more intermetallic compounds in the surface lead to light loses by scattered rays and consequently lower reflectance percentages.

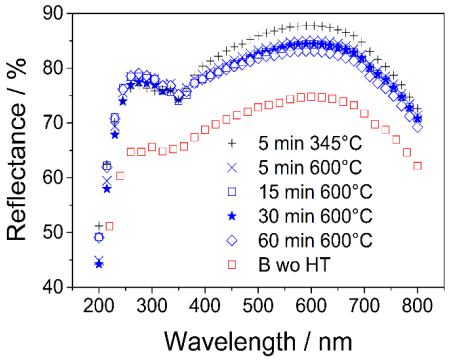

Fig.1. R_T spectra of samples with different HT and electropolished using modified Brytal procedure.

7. Conclusions

Two electropolishing electrolytes were successfully used to obtain highly reflective aluminum alloy AA 1100 surfaces. Although the modified Brytal process generated higher reflectance in the aluminum surfaces than the acid solution, the basic process involves about three times more energy consumption than the acid one. Second phases caused uneven dissolution process in the acid electrolyte generating a scalloped surface for the non-heat- treated samples and superficial localized iron-rich defects in the heat-treated ones. These surface defects rise light scattering and therefore reduces the total reflectance of the aluminum surface. The effect of a previous heat treatment on surface reflectance was clearly observed. A short and low-temperature heat treatment is enough to release stresses and to eliminate rolling marks. Larger times or higher temperatures increase precipitation of second-phase particles at the surface, resulting in light scattering and consequently diminishing total reflectance of the surface. Properly electropolished 1100 Al alloy is suitable as a reflective surface for solar thermal applications.

References

[1] A. García-Segura, A. Fernández-García, M. J. Ariza, F. Sutter, and L. Valenzuela, *Renew. Sustain. Energy Rev.*, vol. 62, pp. 453–467, 2016.

[2] T. Fend, G. Jorgensen, and H. Küster, *Sol. Energy*, vol. 68, no. 4, pp. 361–370, 2000.

[3] J. E. Hatch, *Properties of Pure Aluminum*. ASM International, 1984.

[4] S. Van Gils, S. Holten, E. Stijns, M. Vancaldenhoven, H. Terryn, and L. Mattsson, *Surf. Interface Anal.*, vol. 35, no. 2, pp. 121–127, 2003.

[5] M. Bauccio, *"ASM Metal Reference Book ASM International." Materials Park, USA*, Third Edit. 1993.

[6] Wood W G, "Metals Handbook," in *Suface Cleaning Finishing and Coating*, Vol 5., Materials Park, Ohio: American Society of Metals, 1982.

[7] P. Wernick, S., Pinner, R., Sheasby, *ASM International*, Fifth edit., GB, 1987, pp. 1-1273.

Carbon quantum dots as hole transport layer in HyLEDs.

Sofia Paulo,[1,2]* Eugenia Martinez-Ferrero [2], Emilio Palomares[1,3]

[1]Institute of Chemical Research of Catalonia (ICIQ). The Barcelona Institute of Science and Technology (BIST), Tarragona, Spain
[2]Fundació Eurecat, Mataró, Spain.
[3]Catalan Institution for Research and Advanced Studies (ICREA), Barcelona Spain.
* spaulo@iciq.es

Abstract

Under scale up point of view, the most widely used hole transport materials (HTMs) are PEDOT:PSS and molybdenum oxide inks. Although they present some issues when they are deposited by roll-to-roll or inject printing. PEDOT:PSS present poor charges injection carriers and PSS has to be added in order to improve the solubility. For the other hand, the high annealing temperature needed to deposit molybdenum oxide limits its applicability on flexible and textiles substrates.[1]
In order to solve these problems, a new family of carbon based quantum dots (CQDs) were synthetized. The low temperature annealing as well as the good solubility in non-chlorinated solvents make CQDs an excellent alternative to replace the above HTMs mentioned.

Here, we show the results that we obtained using CQDs as hole transport layer (HTL) in HyLEDs. This project was done with the collaboration of Eurecat under the supervision of Dra. Eugenia Martinez.

1. Introduction

Carbon based quantum dots have emerged the last decades as novel material to use in replacement of heavy metal based quantum dots for optoelectronic application as well as bioimaging and luminescent sensors. Since their discovery in 2004, graphene one of the carbon allotropes family have been extensively studied due to their possible application in the optoelectronic field because graphene and graphene oxide present a high carrier mobilities and thermal stability. However, one of the inconvenient to work with graphene is the scale up in high quality and reproducible manner. Some groups have published possible synthesis to help to resolve that problem but a further optimization is needed. For that reason carbon quantum dots (CQDs) as a carbon allotropes, may have the same carriers mobilities than graphene and they may be a possible alternative.
As we mentioned before, CQDs was used as HTL in inverted LEDs. ZnO was used as electron transport layer because metal oxides give a better robustness and air stability of such device. Poly[(9,9-dioctylfluorenyl-2,7-diyl)-co-(1,4-benzo-{2,10,3hiadiazole)] (F8BT) was used as emissive layer.

Our idea is try to find a new material that can be used as HTL and achieve all the requirements that we have discussed before such as good hole injection balance, lower annealed temperature in order to use in flexible substrate, environmental friendly, and easy processable. In addition, they can be used in scale-up process techniques as inject printing and roll-to-roll.

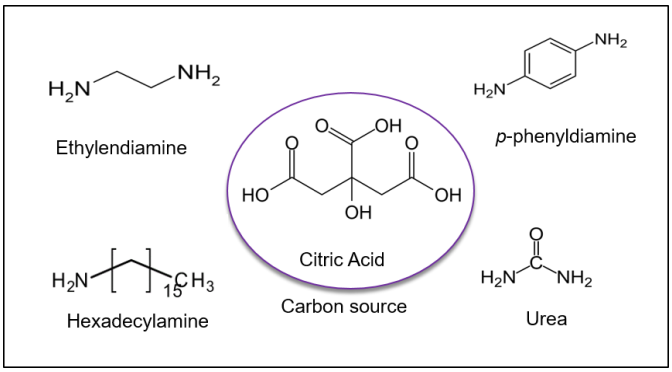

Figure 1. General Scheme for the synthesis of carbon based quantum dots.

2. Results

The synthesis of CQDs were carried out using two procedures described in the bibliography: Hot injection[2] and hydrothermal approach.[3] Our new hole transport layers were based on amines group (Figure 1), this kind of ligands were used in various applications such as LEDs, Perovskites solar cells[4], organic solar cells.

Devices were constructed using following procedure. ITO coated glass was washed in acetone and two time in isopropanol. ZnO NPs was spin coated on top of ITO at

5000 RPM 1min followed by annealed at 150ºC during 3hours. Then, F8BT (30mg/mL *p*-xylene) was deposited on top of zinc oxide at 2000 RPM during 1min followed by baked 155ºC during 30min. The different HTM were deposited by spin coating follow by an annealing at 110ºC during 10min. Finally, MoO_3 and Au were thermally evaporated on top of F8BT.

In figure 2 appears the final device structure with thickness of each layer measured by profilometer. F8BT used as emissive layer which present an emission band at 550nm. The annealing temperature of F8BT was 155ºC in order to achieve to the rubbery state from the glassy one reported in the bibliography. [5]

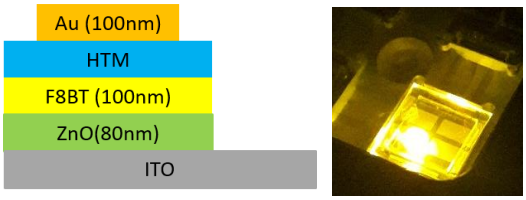

Figure 2. Description of a multilayer HyLED.

In order to improve the wettability, stability and increase their conductivity between the aqueous solution from CQDs and PEDOT:PSS deposit on top of F8BT, some amounts of 1- isopropanol (IPA) was added to the solution[6].

The energy level alignment and the hole mobilities (table 1) were measured to study how the charge injection and charge transport could influence the HyLEDs. Here we show the importance of energy band alignment between contacts' work-function and HOMO/LUMO of emitting layer.

In addition, the space charge limited current (SCLC) was measured to obtain the hole mobility. We did not observe any remarkable variation of the hole mobility changing the ligand length.

Hole transport material (HTM)	Band gap (eV)	HOMO/LUMO (eV)	Hole mobilities ($cm^2V^{-1}s^{-1}$)
Ethylendiamine	3.07	-5.52/-2.45	$2.41 \cdot 10^{-6}$
p-phenyldiamine	2.81	-5.12/-2.07	$1.50 \cdot 10^{-6}$
Hexadecylamine	3.36	-5.70/-2.34	$8.54 \cdot 10^{-5}$
Urea	2.93	-5.84/-2.90	$2.92 \cdot 10^{-6}$
MoO_3	2.80	-9.50/-6.70	$3 \cdot 10^{-3}$
PEDOT:PSS	3.00	-5.20/-2.20	$1.2 \cdot 10^{-2}$

Table 1. Electrochemical properties of CQDs in solution and hole mobilities of CQDs in films.

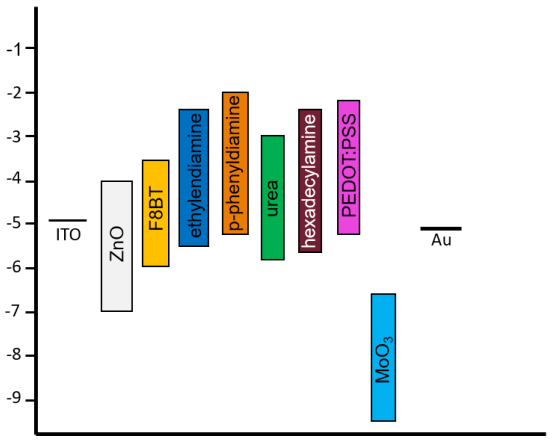

Figure 3. Level alignment of each material that we used to fabricate the devices.

In figure 4 shows our best results recorded using different HTM. The devices were measured in air.

a)

b)

Figure 4. HyLED device performance. a) Current density versus voltage (J-V). b) Luminance versus applied voltage (L-V).

Hole transport material (HTM)	Turn-on voltage V^a (V)	Max. Luminance (Cd/m^2)
PEDOT:PSS	6.10	2000
Ethylendiamine	4.90	70
p-phenyldiamine	10.18	13
Hexadecylamine	14.50	174
Urea	9.60	146
No HTM	15.20	2
MoO3	2.85	2600

Table 2. Optoelectronic results of HyLEDs devices using different HTM. V^a is the turn-on voltage at 0.1 Cd/m^2.

In table 2, where appears the optoelectronics results of HyLEDs using PEDOT:PSS, MoO_3 and Carbon Quantum dots as hole transport layer. The maximum luminance was 2600 Cd/ m^2 using molybdenum oxide evaporated as hole transport layer and a turn-on voltage 2.85V while, using PEDOT:PSS doped with IPA, the device achieved until 2000 Cd/m2 and a turn-on voltage at 6.10V.

Regarding general results using CQDs as HTL the optoelectronics results present lower luminance compared with MoO_3 and PEDOT: PSS. However, using ethylendiamine as capping ligand there is an enhancement of the turn-on voltage compared with PEDOT: PSS. Based on the hole mobilities results and the electrochemical levels it is quite clear the reasons of the optoelectronic results, nevertheless, one of the goals of this projects was to find a material than can be deposited by spin coating conditions.

Despite the device of CQDs-ethylendiamine presents better turn-on voltages, it does not present the higher efficiency. Using hexadecylamine 146 cd/m^2 and urea 174 cd/m^2 as capping ligand present higher luminance.

3. Conclusions

In summary, we present a proof of concept using carbon quantum dots as hole transport material in HyLEDs. The most remarkable results was obtained using CQD with ethylendiamine as capping ligand, as they present a lower turn-on voltage compared with PEDOT:PSS. Additional studies should focus on the optimization of the layer of carbon quantum dots as well as better controlled device fabrication.
Carbon quantum dots is an emerged material which their potential optoelectronic properties to use in many technological applications.

References

[1]Girotto, C.; Voroshazi, E.; Cheyns, D.; Heremans, P.; Rand, B. P.: "Solution-Processed MoO3 Thin Films As a Hole-Injection Layer for Organic Solar Cells", *ACS Applied Materials & Interfaces* 2011, 3, 3244-3247.
[2]Wang, F.; Pang, S.; Wang, L.; Li, Q.; Kreiter, M.; Liu, C.-y.: "One-Step Synthesis of Highly Luminescent Carbon Dots in Non-coordinating Solvents", *Chemistry of Materials* 2010, 22, 4528-4530.
[3]Zhu, S.; Meng, Q.; Wang, L.; Zhang, J.; Song, Y.; Jin, H.; Zhang, K.; Hongchen, S.; Wang, H.; Yang, B.: "Highly Photoluminescent Carbon Dots for Multicolor Patterning, Sensors, and Bioimaging" , 2013; Vol. 52.
[4]Paulo, S.; Stoica, G.; Cambarau, W.; Martinez-Ferrero, E.; Palomares, E.: "Carbon quantum dots as new hole transport material for perovskite solar cells", *Synthetic Metals* 2016, 222, 17-22.
[5]Martinez-Ferrero, E.; Grigorian, S.; Ryan, J. W.; Cambarau, W.; Palomares, E.:" Influence of the Molecular Weight and Size Dispersion of the Electroluminescent Polymer on the Performance of Air-Stable Hybrid Light-Emitting Diodes", *ACS Applied Materials & Interfaces* 2015, 7, 1078-1086.
[6]Pan, J.; Huang, Q.; Zhang, Y.; Chen, J.; Tao, Z.; He, C.; Zhou, K.; Lei, W.: "Application of Solvent Modified PEDOT:PSS in All-Solution-Processed Inverted Quantum Dot Light-Emitting Diodes", *Journal of Display Technology* 2016, 12, 1157-1161.

Novel Concept to Calculate the B2B Tunneling Probability based on an area equivalent WKB approach for a usage in TFET Compact Models

Fabian Horst[1,2,✠], Atieh Farokhnejad[1,2], Benjamín Iñíguez[2] and Alexander Kloes[1]
[1]NanoP, TH Mittelhessen University of Applied Sciences, Giessen, Germany,
[2]DEEEA, Universitat Rovira i Virgili, Tarragona, Spain,
✠e-mail: fabian.horst@ei.thm.de, phone: +49 641 309 1968

I. Introduction

The tunnel-field effect transistor (TFET) is handled to be the surrogate of the conventional MOSFET technology. Due to the band-to-band (B2B) tunneling based device current of TFETs, it is possible to achieve subthreshold slopes $< 60\,^{\mathrm{mV}}/_{\mathrm{dec}}$. In addition, the TFET is suitable for ultra-low power applications, since a reduction of the supply voltage does not influence the leakage current [1]. The B2B tunneling current or rather the tunneling probability T_{tun} is calculated with help of the transmission coefficient. In most cases the transmission coefficient for an arbitrary energy barrier shape is obtained by using the Wentzel-Kramers-Brillouin (WKB) approximation [2]. In this work a numerical robust model to calculate the transmission coefficient in TFETs with the help of an area equivalent WKB approach is introduced.

II. Modeling Approach

Calculating the tunneling probability by the WKB approximation in general is done as follows [2]:

$$T_{tun} \approx \exp\left(-2 \cdot \int_{x_1}^{x_2} \sqrt{\frac{2m^*}{\hbar^2}\Big[U(x) - E\Big]}\, dx\right), \quad (1)$$

with the effective carrier mass m^*, the reduced Planck constant $\hbar$, the energy shape along the x-axis $U(x)$ and the tunneling energy E. The aim of this work is to characterize the expression $U(x)$ by an area equivalent approach. Area equality means that the area of the tunneling barrier A_1, enclosed by the band structure, has the same size as an equivalent triangular with an area A_2 (see Fig. 1).

The calculation of the area A_1 requires a compact solution of the device's electrostatics and band structure. Here, the electrostatic potential solution of a double-gate (DG) TFET is used to calculate A_1 [3]. By using the triangular with the area A_2 to define the energy barrier height U_{bar} and a compact expression for the tunneling length l_{tun} [3], [4], the tunneling barrier shape is given by:

$$U(x) = -\frac{U_{bar}}{l_{tun}} \cdot x, \text{ with } \quad U_{bar} = \frac{2 \cdot A_1}{l_{tun}} = \frac{2 \cdot A_2}{l_{tun}}. \quad (2)$$

This project was supported by the German Federal Ministry of Education and Research under contract No. FKZ 13FH010IX5 and the Spanish Ministry of Economy and Competitiveness through project GREENSENSE (TEC2015-67883- R).

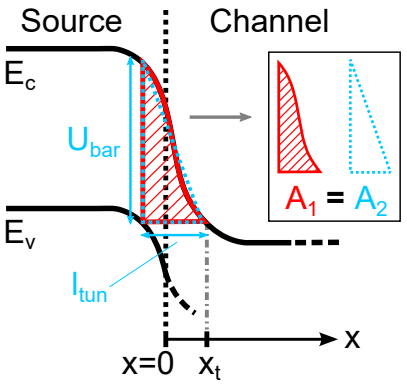

Figure 1. Schematic band structure of a TFET at the source-to-channel junction, showing the shape of the tunneling energy barrier at $x = x_t$.Furthermore, the enclosed area A_1 (red hatched area) as well as the area equivalent triangular (dashed area A_2) with its energy barrier height U_{bar} and the tunneling length l_{tun} are illustrated.

By inserting the expression for $U(x)$ in Eq. (1) and defining the integration limits of Eq. (1) as $x_1 = x_t - l_{tun}$ and $x_2 = x_t$, the tunneling probability is rewritten as:

$$T_{tun} = \exp\left(-2 \cdot \int_{x_t - l_{tun}}^{x_t} \sqrt{\frac{2m^*}{\hbar^2} \cdot \left(-\frac{U_{bar}}{l_{tun}} \cdot x\right)}\, dx\right), \quad (3)$$

whereby the tunneling energy E is chosen to be zero. Solving Eq. (3) leads to the well-known result for the WKB approximation applied to a triangular profile:

$$T_{tun} = \exp\left(-\frac{4}{3} \cdot \sqrt{\frac{2m^*}{\hbar^2} \cdot U_{bar}} \cdot l_{tun}\right). \quad (4)$$

The resulting closed-form tunneling probability allows for an implementation in TFET compact models.

III. Modeling Results & Verification

In order to validate the modeling approach, the expression for T_{tun} is implemented in an existing DG TFET compact model [3], [4] and compared to TCAD Sentaurus simulation data of an n-type Si DG TFET (see Fig. 2) as well as a quasi-2D modeling approach for the WKB approximation [5].

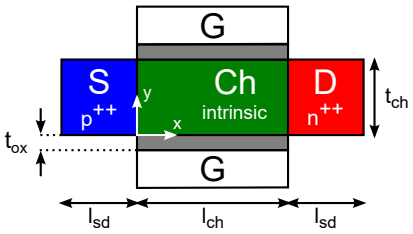

Figure 2. 2D device geometry sketch of an n-type Si DG TFET showing its structural parameters, defined as follows: $l_{ch} = 22\,\text{nm}$, $l_{sd} = 20\,\text{nm}$, $t_{ch} = 10\,\text{nm}$ and $t_{ox} = 2\,\text{nm}$. The S/D region is highly p/n-doped ($N_{s/d} = 10^{20}\,\text{cm}^{-3}$), the channel stays intrinsic. The gate oxide consists of HfO_2.

Since the compact solution for the band structure forms the base of calculating the area A_1 and T_{tun}, first of all the electrostatics is verified by TCAD simulation data. In Fig. 3 the modeled band structure at the channel's surface is compared to TCAD simulations and shows a good fit for various V_{gs} values at $V_{ds} = 0.7\,\text{V}$

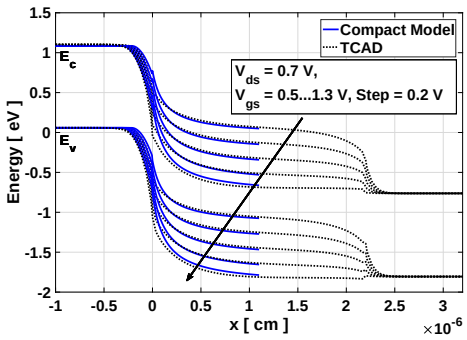

Figure 3. Modeling results for the band structure of the n-type DG TFET at the surface of the channel for various V_{gs}. The compact model (solid lines) is compared the TCAD data (dotted lines).

By using the band structure of the DG TFET and the equivalent area A_2 it is possible to calculate and visualize the triangular tunneling barrier. Fig. 4 illustrates the modeling results of Eq. (2) compared to the quasi-2D modeling approach at the surface of the channel. Simulations are performed for $V_{gs} = 0.9\,\text{V}$ and $V_{gs} = 1.5\,\text{V}$ at $V_{ds} = 0.7\,\text{V}$, whereby the effective mass is chosen to be $m^* = 0.252 \cdot m_0$ (TCAD: $m^* = 0.26 \cdot m_0$). In Fig. 4(a) it can be seen that the resulting $U(x)$ follows the shape of the band structure in a satisfying way. The quasi-2D approach shows a similar shape, whereby the tunneling barrier height U_{bar} is a bit underestimated. A smaller U_{bar} is causing a overestimated value for T_{tun}. At the second gate bias of $1.5\,\text{V}$ (see Fig. 4(b)) the model reproduces the tunneling barrier in good way and the quasi-2D approach overestimates the value of U_{bar}.

In order to verify the expression for the tunneling probability (Eq. (4)) with the help of TCAD simulations, T_{tun} is inserted into the equation to calculate the tunneling generation rate (TGR), published in [4]. The TGR defines the number of carriers generated per second in the conduction band of the channel by B2B tunneling. The modeling results of the TGR at the channel's surface for various V_{gs} at $V_{ds} = 0.7\,\text{V}$ are illustrated in Fig. 5 and compared to TCAD simulation data. Furthermore, the results of the TGR calculated with the quasi-2D approach are depicted in this figure as well. It can be seen that a horizontal displacement occurs in the modeled TGR for both compact model and quasi-2D approach. This x-offset has

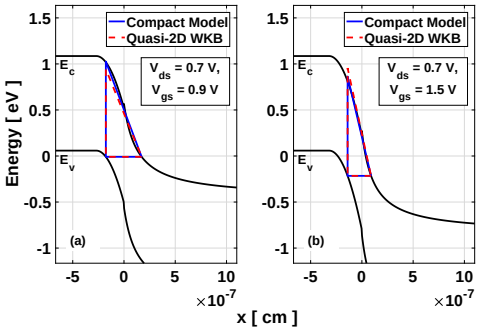

Figure 4. Resulting tunneling barrier at the channel's surface to calculate T_{tun} for (a) $V_{gs} = 0.9\,\text{V}$ and (b) $V_{gs} = 1,5\,\text{V}$ at $V_{ds} = 0.7\,\text{V}$. The compact model (triangular with solid lines) is depicted in comparison to the quasi-2D WKB approach (triangular with dashed lines).

little influence on the result of the integration along the x-axis to obtain the current density and at last the B2B tunneling current. Besides the occurring x-offset, the amount of the modeled TGR is predicted satisfactorily, whereby the quasi-2D approach overestimates the TGR and at last the current density. This leads to an additionally fitting parameter to scale down the overestimation, which can be avoided by the novel area equivalent compact modeling approach.

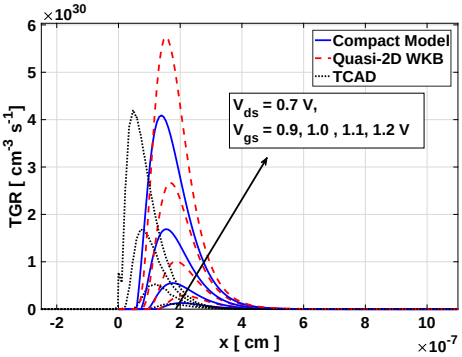

Figure 5. TGR at the channel's surface at $V_{ds} = 0.7\,\text{V}$ for various V_{gs}. Compact model (solid lines) is verified by TCAD simulations (dotted lines) and compared to the quasi-2D modeling approach (dashed lines).

Acknowledgment

We would like to thank Keysight Technologies for the license donation and support of the software IC-CAP and AdMOS GmbH for support.

References

[1] A. C. Seabaugh and Q. Zhang, "Low-voltage tunnel transistors for beyond CMOS logic," *Proceedings of the IEEE*, vol. 98, no. 12, pp. 2095–2110, Dec. 2010.

[2] S. M. Sze and K. K. Ng, *Physics of semiconductor devices*, 3rd ed. John Wiley & Sons, 2006.

[3] F. Horst, M. Graef, F. Hosenfeld, A. Farokhnejad, F. Hain, G. V. Luong, Q.-T. Zhao, B. Iñíguez, and A. Kloes, "Implementation of a DC compact model for double-gate Tunnel-FET based on 2D calculations and application in circuit simulation," in *2016 46th European Solid-State Device Research Conference (ESSDERC)*, Sep. 2016, pp. 456–459.

[4] F. Horst, A. Farokhnejad, B. Iñíguez, and A. Kloes, "An area equivalent WKB approach to calculate the B2B tunneling probability for a numerical robust implementation in TFET compact models," in *Accepted for Mixed Design of Integrated Circuits & Systems (MIXDES), 2018*, 2018.

[5] M. Graef, T. Holtij, F. Hain, A. Kloes, and B. Iñíguez, "A 2D closed form model for the electrostatics in hetero-junction double-gate tunnel-FETs for calculation of band-to-band tunneling current," *Microelectronics Journal*, vol. 45, no. 9, pp. 1144–1153, 2014.

Simulating the impedance spectroscopy of an hybrid perovskite solar cells via time-dependent 1D drift-diffusion model

Ilario Gelmetti,[a,b] D. Moia,[c] P. Calado,[c] P. Barnes,[c] E. Palomares[a,d]

[a] Institute of Chemical Research of Catalonia (ICIQ), Spain.
[b] Departament d'Enginyeria Electrònica, Elèctrica i Automàtica, Universitat Rovira i Virgili, Avda. Països Catalans 26, 43007 Tarragona, Spain.
[c] Department of Physics, Imperial College London, London SW7 2AZ, UK.
[d] ICREA, Passeig Lluís Companys, 23, Barcelona, Spain.

igelmetti@iciq.es

Abstract

Impedance spectroscopy is commonly used to analyse charge dynamics in optoelectronic devices. Its interpretation requires a close-to-complete understanding of the physical phenomena happening in the device under measurement. How an hybrid perovskite solar cell works is still under debate,[1] and because of this the usage of impedance spectroscopy technique is hindered. With drift-diffusion modelling[2] we match the measurements with one of the most likely hypothesis, allowing parameters extraction and supporting the validity of the hypothesis.

1. Background

A nice and effective model for time dependent, 1-dimensional drift-diffusion simulation of multilayer devices including multiple charge carriers (electrons, holes, ions) has been open sourced[3] and its use has been demonstrated on hysteresis,[2] transient ideality factor[4], space charge layer width estimation[5] of perovskite solar cells. This model is easily adaptable to simulate most kinds of time resolved electrical or optical experiment, as is impedance spectroscopy. Quite importantly for our study, this model implements two main types of recombinations: radiative and trap mediated Shockley-Reed-Hall (SRH) recombination.

In many of the literature articles on impedance spectroscopy of perovskite solar cells we found reports of giant capacitance under illumination[6] and inductive effects[7], this was explained[8] and modelled[9] with an important free charges accumulation at the perovskite-contacts interface. As this hypothesis is certainly an interesting possibility, hard to confirm or to confute, we looked for a better insight on the charge dynamics during impedance spectroscopy measurement using the aforementioned Driftfusion[3] model.

2. Simulation

In order to have an as-good-as-possible result, the simulation was designed to mimic the experimental setup. The applied AC voltage was simulated as single voltage points on a sinusoidal function, usually 20 periods were simulated obtaining the electrical current for 40 points each period, as represented in Fig. 1. This resulting current profile was used for extracting phase and amplitude via a demodulation method, which tries to be as close as possible to the internal mechanisms of a two-phase lock-in-amplifier. Additionally to the AC voltage, simulations included the application of a DC voltage and of an illumination generating free charges, either at open circuit or at short circuit conditions.

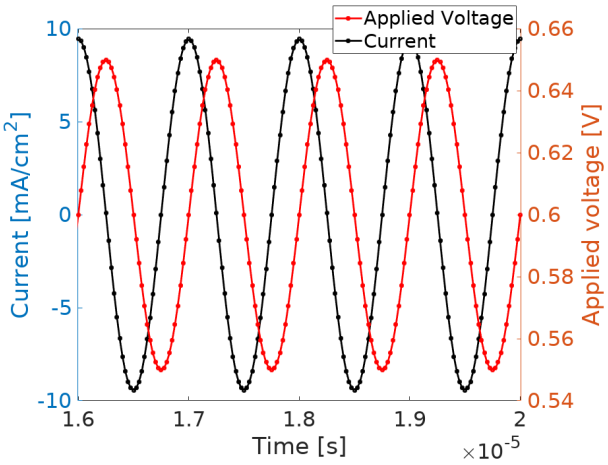

Fig. 1. Simulated current profile for a perovskite solar cell illuminated with 0.001 sun when a voltage oscillating from VOC - 50 mV and VOC + 50 mV at 1 MHz is applied.

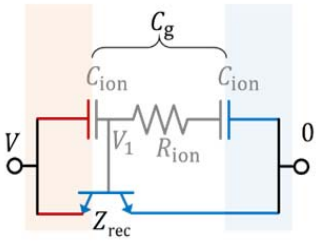

Fig. 2. Simplified equivalent electrical circuit. C_g is geometrical capacitance; C_{ion} is the double layer capacitance due to ions accumulation/depletion at the perovskite-contacts interfaces; Z_{rec} is the impedance of the interfacial charges recombination; R_{ion} is the resistance depending on the ionic mobility and concentration; V_1 is the potential applied to the base of the transistor due to the ions presence.

3. Results

We observed the appearance of the still-unexplained phenomena of the giant capacitance, as reported in Fig. 3, without observing the high interfacial concentration of free charges that was indicated as a possible cause[8]. This effect was observed both applying high DC voltages and applying illumination at open circuit, in accordion to the acquired experimental data. Thanks to the flexibility of the Driftfusion[3] simulation software we could have an insight on the charge dynamics during the impedance spectroscopy simulation. In this way we observed that the known influence of the ionic concentration profile on the charges recombination can explain the unexpectedly big out of phase current component. This can be represented as a bipolar junction transistor, as in Fig. 2, where the ionic accumulation drives the base of the transistor, causing electrical current variations. Ionic migration itself is equivalent to a parallel plate capacitor component where what accumulates at the interfaces, in a double layer fashion, is the ionic charge. This capacitance alone has a small contribution, but gets amplified by the mentioned transistor effect, resulting in an apparent giant capacitance.

4. Conclusions

With this work[10] (available as pre-print on Arxiv) we propose an equivalent electrical circuit for perovskite solar cells and other electrochemical devices including ionic species. This unleashes the full versatility of the impedance spectroscopy technique in the characterization of such a promising photovoltaic material.

References

(1) Pockett, A.; Eperon, G. E.; Sakai, N.; Snaith, H. J.; Peter, L. M.; Cameron, P. J. Microseconds, Milliseconds and Seconds: Deconvoluting the Dynamic Behaviour of Planar Perovskite Solar Cells. *Phys. Chem. Chem. Phys.* **2017**, *19* (8), 5959–5970.

(2) Calado, P.; Telford, A. M.; Bryant, D.; Li, X.; Nelson, J.; O'Regan, B. C.; Barnes, P. R. F. Evidence for Ion Migration in Hybrid Perovskite Solar Cells with Minimal Hysteresis. *Nat. Commun.* **2016**, *7*, 13831.

(3) Calado, P.; Gelmetti, I.; Azzouzi, M.; Hilton, B.; Barnes, P. R. F. Driftfusion https://github.com/barnesgroupICL/Driftfusion.

(4) Calado, P.; Burkitt, D.; Yao, J.; Troughton, J.; Watson, T. M.; Carnie, M. J.; Telford, A. M.; O'Regan, B. C.; Nelson, J.; Barnes, P. R. F. Identifying Dominant Recombination Mechanisms in Perovskite Solar Cells by Measuring the Transient Ideality Factor. *ArXiv* **2018**.

(5) Belisle, R. A.; Nguyen, W. H.; Bowring, A. R.; Calado, P.; Li, X.; Irvine, S. J. C.; McGehee, M. D.; Barnes, P. R. F.; O'Regan, B. C. Interpretation of Inverted Photocurrent Transients in Organic Lead Halide Perovskite Solar Cells: Proof of the Field Screening by Mobile Ions and Determination of the Space Charge Layer Widths. *Energy Environ. Sci.* **2017**, *131*, 6050.

(6) Juarez-Perez, E. J.; Sanchez, R. S.; Badia, L.; Garcia-Belmonte, G.; Kang, Y. S.; Mora-Sero, I.; Bisquert, J. Photoinduced Giant Dielectric Constant in Lead Halide Perovskite Solar Cells. *J. Phys. Chem. Lett.* **2014**, *5* (13), 2390–2394.

(7) Ghahremanirad, E.; Bou, A.; Olyaee, S.; Bisquert, J. Inductive Loop in the Impedance Response of Perovskite Solar Cells Explained by Surface Polarization Model. *J. Phys. Chem. Lett.* **2017**, *8* (7), 1402–1406.

(8) Zarazua, I.; Bisquert, J.; Garcia-Belmonte, G. Light-Induced Space-Charge Accumulation Zone as Photovoltaic Mechanism in Perovskite Solar Cells. *J. Phys. Chem. Lett.* **2016**, *7* (3), 525–528.

(9) Garcia-Rosell, M.; Bou, A.; Jiménez-Tejada, J. A.; Bisquert, J.; Lopez-Varo, P. Analysis of the Influence of Selective Contact Heterojunctions on the Performance of Perovskite Solar Cells. *J. Phys. Chem. C* **2018**.

(10) Moia, D.; Gelmetti, I.; Calado, P.; Fisher, W.; Stringer, M.; Game, O.; Hu, Y.; Docampo, P.; Lidzey, D.; Palomares, E.; et al. Ionic-to-Electronic Current Amplification in Hybrid Perovskite Solar Cells. *ArXiv* **2018**.

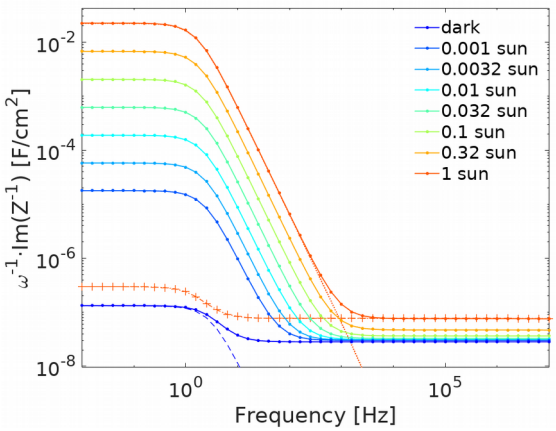

Fig. 3. Simulated apparent capacitance for a perovskite solar cell at various illuminations and open circuit conditions. Solid line: apparent capacitance; dashed blue line: capacitance due to ionic migration in the dark; line marked with plus: real capacitance due to accumulated charges in the device at 1 sun; dotted red line: capacitance measured due to non-accumulating recombination current.

Comparing performance of flexible and rigid substrates for In_2O_3 based gas sensors

M. Alvarado[1], E. Navarrete[1], J.L. Ramírez[1], A. Romero[1], E. Llobet[1]

1. Minos, Departament d'Enginyeria Electrònica, Elèctrica i Automàtica
Universitat Rovira i Virgili
Tarragona, Spain
miriam.alvarado@urv.cat

Abstract

Indium oxide was synthesized through an oxidation process starting form an ionic precursor compound. Synthesized indium oxide was used to fabricate gas sensors, under the same conditions, in two types of substrates; a rigid one, alumina, and a flexible one, polyimide (Kapton®). Half of those gas sensors were doped with silver nanoparticles, through sputtering, and tested by immersing them in a flow of NO_2 gas.

1. Introduction

Last technological advances have made possible to develop a variety of electronic components using printing technologies in different materials such as fabric, paper and plastics.

Thin polymeric films are extremely attractive as substrates. They can be made lightweight and inexpensive making possible to employ them in high-volume and low-cost commercial products. Polymer films are inherently plastic enabling a high degree of mechanical flexibility and conformability. A number of plastic films are available including thermoplastic amorphous polymers such as polycarbonate, polyether sulfone, and high-transition glass temperature materials (Tg) such as polyimide [1]. The polyimide has excellent physical, electrical and mechanical properties over a wide temperature range, -269 °C until 400 °C [2].

Indium oxide (In_2O_3) is a wide bandgap transparent semiconductor (with a direct band gap of about 3.6 eV and an indirect band gap of about 2.5eV). In_2O_3 in the bulk form has been widely used in solar cells and organic light emitting diodes. More importantly, In_2O_3 films have been successfully used as detectors of toxic gases, with detection levels down to 5 ppm for NO_2 [3].

In this work In_2O_3 has been deposited onto two different substrates. We employed alumina substrates with interdigitated Pt electrodes (IDE) and polyimide substrates with Ag IDE. NO_2 has been measured to compare the response and performance of In_2O_3 stenciled onto both substrates.

2. Experimental

A. Substrate preparation

A rigid alumina substrate was used with Pt IDE on one side and a heater on the other. The alumina substrates have length-width dimensions of 25.4 mm · 3.8 mm. The IDE have tracks 300 µm width and a gap between tracks of 300 µm. The heater is a Pt meander shaped track with a mean resistance of 8 Ω. The geometry of alumina IDE was replicated over a polymeric flexible film. A commercial high resistant adhesive coated polyimide foil (Kapton® 25 µm) has been used to fabricate the polymeric devices. Two layers of the polymeric film were stuck to one face of the alumina substrate. The IDE pattern was cut with a CO_2 laser over the outer layer. The parts belonging to the design were manually removed; obtaining the cut-out holes that will be filled with ink. Through stencil technique, Ag ink (DuPont 5064H silver conductor) was deposited onto the polyimide. The Ag ink was dried in an oven at 130 °C for 20 minutes. Later, the remaining parts of the polyimide outer layer were removed obtaining an Ag IDE over the polymeric film.

B. Material synthesis and methods

To obtain In_2O_3, commercial available indium chloride (Sigma Aldrich 99.8% purity) was used as precursor compound. In an analytical balance 40 mg of $InCl_3$ were weighted and placed in a ceramic crucible. The material was dispersed homogenously among the surface of the crucible in the minimum possible time as that compound starts to sublimate at 5 ºC. In order to oxidize the material it was placed inside a muffle where the oxidation process would occur. Typically a current of synthetic air is used in such process to increase the available oxygen but, in this particular case, the material was oxidized without any synthetic air flow in order to obtain a crystal oxide structure under low oxygen concentration. The temperature was increased progressively until it reached 400 ºC, and was kept at that temperature for 2 hours. Finally the material was left inside the muffle overnight to be gradually cooled at room temperature. Using an Agatha crucible, the material was placed inside and mashed softly until it turned into a homogenous yellowish dust.

The material obtained after the synthesis was characterized using environmental scanning electron microscope (E-SEM, Jeol 7600F), which had also an EDX detector to obtain semi-quantitative information of the material composition.

C. Sensor preparation

A set of four sensors were prepared using that approach; two alumina based sensors with platinum IDEs on top and a platinum heater on bottom; and two Kapton® (25 µm) based sensors with silver IDEs on top . An In_2O_3 paste was prepared using 25 mg of material dissolved in 0.5 µl of 1,2-propanediol and mixed. A

polymer mask was prepared, a 6 mm · 3.8 mm rectangle was cut with a CO_2 laser over a piece of polyimide film (Kapton 50 µm). Through the polymeric mask, a layer of material was placed on top of the IDEs as bridge contact and finally the sensors were stored overnight at 80 ºC inside an oven to fully evaporate the solvent.

One sensor of each pair was taken to a sputtering system to be doped with silver nanoparticles. The sputtering involved a 10 s deposition at 150 W in DC mode.

D. Gas sensing procedure

The sensors were placed inside an inert Teflon® chamber and connected to an external power source which would provide a constant voltage to the heaters. In this work we applied 3.2V/0.96A, 4.2V/1.1A and 5.1V/1.2A to reach the desired working temperatures, 150 ºC, 200 ºC and 250 ºC. The system flow was set to be constant during the whole analysis at 100 ml/min. Using a mass flow the concentration of the target gas (NO_2) was modified. The concentrations chosen for this work were 3, 5, 5.5 and 6 ppm of NO_2. For each temperature the pulses were performed as following: During one hour and a half synthetic dry air was applied in order to stabilize the sensors and then pulses of 30 minutes of gas alternated with pulses of 30 minutes of dry synthetic air were repeated.

3. Results and Discussion

The E-SEM imaging results of the In_2O_3 layer showed an amorphous material in which a dispersion of indium oxide octahedrons is dispersed and included among the whole surface. The octahedrons have several edge sizes comprising values from 1.25 up to 7.5 µm (Figure 1).

The sensors were tested against a flow of NO_2 at different concentrations levels.

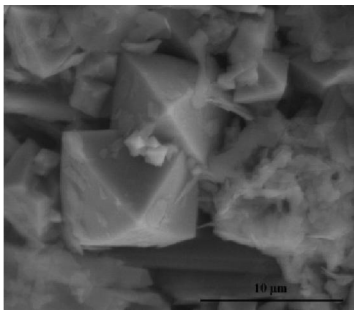

Fig.1. E-SEM image of two octahedrons fused.

Measurements revealed that the sensors responses decrease when the temperature is higher and the best response is obtained when the temperature was close to 150 ºC (power heating at 3.2V/0.96A). Kapton® high thermal resistance, several orders of magnitude higher than the alumina, turns into clear difference in thermal conditions for the same electric power supplied to their heaters. As all of them were tested at the same time under the same conditions, alumina sensors were able to reach the working temperature in a lower time giving a more stable and repetitive response (Figure 2). It can be also inferred from Figure 2 that silver nanoparticles do not improve significantly the alumina sensors response, even though at higher temperatures have slightly better response values.

Due to this difference Kapton® sensors could not reach the optimal working temperature during the experimental process even though, as it shown in Figure 3, they have also displayed a response towards the target gas. Therefore in order to work with these Kapton® based sensors it is important to increase the stabilization time to ensure that the optimal conditions have been reached. Otherwise, a different heater+IDE geometry should be designed to improve their thermal response (despite this would difficult the comparison).

4. Conclusions

The polyimide (Kapton®) is well-known as an inert substrate, when carrying out the measurements, the response observed belonged mainly to the active layer deposited over the Kapton®. This demonstrates the feasibility of manufacturing metal oxide gas sensors on transducers of this low-cost flexible material. The redesign of the geometry and electrical parameters that will produce working conditions comparable to the work point used in the devices used until the time is still outstanding.

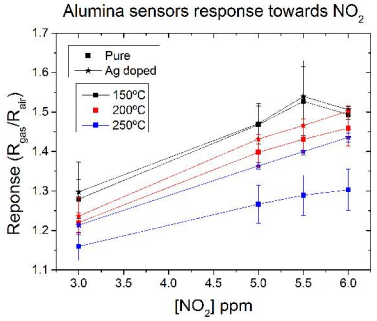

Fig.2. Alumina based sensors response at different temperatures and different NO_2 concentrations.

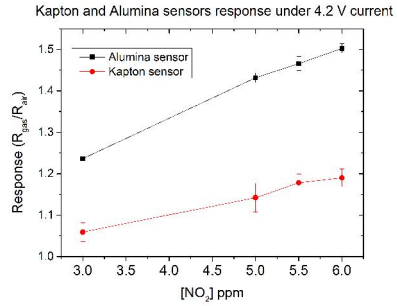

Fig.3. Kapton® based sensor response towards NO_2.

References

[1] Zardetto, V., Brown, T. M., Reale, A., & Carlo, A. Di. (2011). Substrates for Flexible Electronics : A Practical Investigation on the Electrical, Film Flexibility, Optical, Temperature, and Solvent Resistance Properties, 638–648. https://doi.org/10.1002/polb.22227

[2] DuPont 5064H Silver Conductor. MCM5064H. DuPont. November, 2011.

[3] Li, C., Zhang, D., Han, S., Liu, X., Tang, T., Lei, B., … Zhou, C. (2003). Synthesis, Electronic Properties, and Applications of Indium Oxide Nanowires. *Annals of the New York Academy of Sciences*, *1006*(2), 104–121. https://doi.org/10.1196/annals.1292.007

Measurement of NFC Sensor Tags Using Smartphones

Martí Boada Navarro - [marti.boada@urv.cat]

Abstract

The Internet of Things (IoT) has been spreading all over the world for all kinds of applications, from medical to agriculture, passing through civil engineering or environmental monitoring. However, the increasing number of devices which must be connected to the cloud, implies several technological challenges. One of these challenges is designing low-price battery-less devices able to sense data and send it to a database for its analysis and possible actions to be done based on it. Here is where Near Field Communication (NFC) can play an important role. NFC has become very popular for contactless payments, and the number of smartphones with this feature is increasing fast. The main aim of this work is to study the suitability of using NFC technology from any commercial smartphone to supply energy to passive tags with computational capability, getting the data from them, and send it to the cloud, thus avoiding batteries on the sensors, as well as Wi-Fi or Bluetooth chips which would imply a much higher power consumption and higher prices.

1. Introduction

Near Field Communication (NFC) is a subset of protocols within the RadioFrequency IDentification (RFID) technology. NFC is known for its application in payment systems, due the security that implies the short distance between the reader and the tag. However, the short distance brings with it other interesting features which have not been deeply studied yet. NFC standards are managed by the NFC Forum [1]. 5 different type tags are defined. The newest one (Type 5, also known as NFC-V), which is compliant with the ISO/IEC 15693 standard, has a new feature called energy harvesting (EH). The NFC chips with EH capability have an output pin which will deliver a rectified DC voltage obtained from the magnetic field received from the 13.56 MHz signal generated by the reader.

One of the main drawbacks of RFID systems, is the price of the readers. However, the number of commercial smartphones with NFC capability is increasing every day. Thus, bringing the opportunity

Some IoT applications need a constant connection to the cloud, however, there are other applications where the connectivity can be spontaneous. Is in those case where NFC may play an important role.

Soil moisture control is vital for agriculture and gardening in order to optimize the use of water as well as to deal with the specific needs of each crop. Furthermore, it is also important for other purposes such as civil engineering. There are many methods to measure the soil moisture [2]. The method used in this work is framed within the dielectric methods, which are based on the huge difference between the dielectric permittivity of the dried soil (between 3 and 6) and water (about 80). Thus, using the soil as the dielectric part we can indirectly measure the soil moisture content, which is often expressed as Volumetric Water Content (VWC), defined as the volume of water over the total volume.

This paper proposes a passive NFC tag consisting of a soil moisture sensor, which also includes a temperature sensor and a relative humidity sensor as a proof of concept of the use of the NFC energy harvesting capability.

2. System design

Fig. 1 shows the block diagram of the designed prototype.

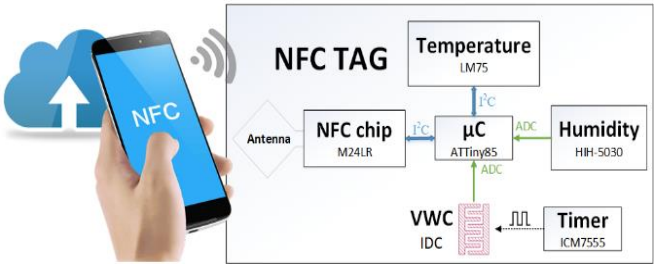

Fig. 1. Block diagram of the system.

The system core is composed of two main components. The first is an NFC/RFID chip M24LR04E-R, from ST Microelectronics, responsible of receiving and sending NFC Data Exchange Format (NDEF) messages as well as rectifying the RF signal to obtain a constant voltage output. This IC is an NFC-V, Type 5 tag, following the NFC Forum classification (ISO 15693 compliant). The second is a low-power Atmel 8-bit AVR ATTiny85 microcontroller, which is responsible of reading the sensor values through its analog and digital inputs, performing programmed operations with them, and writing the computed result into the NFC chip memory. The microcontroller clock frequency is reduced to 1 MHz to dismiss the current consumption up to 300 µA at 3 V.

Fig. 2 shows the prototype manufactured on a FR4 PCB that consists of an NFC antenna, the chipset with a connector that gives access to the microcontroller in order to program it, and the interdigital capacitor which will be sunk into the soil.

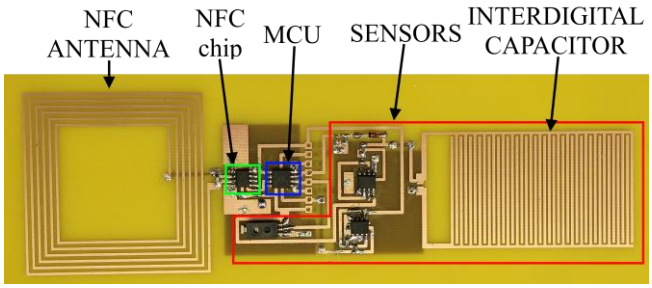

Fig.2. Designed PCB prototype with the antenna, the IDC and the chipset.

3. NFC Energy Harvesting

In order to ensure the communication between the reader and tag and assure enough power for the RF to DC conversion to feed the electronic circuitry, the goal is to maximize the power transfer from the reader to the tag. Then the power delivered to the tag IC (P_d) must be higher than a threshold power (P_{th}): $P_d > P_{th}$. To this end, the efficiency must be maximized. Modern mobiles often use metallic case, therefore special design is used to avoid the losses introduced by the metallic parts or batteries. Fig.2. shows the measured parameter S_{11} for a tag adjusted in the air with C_{tuning}=22 pF and the detuning due to the proximity of a mobile with metallic case at different distances between 1 mm and 12 mm.

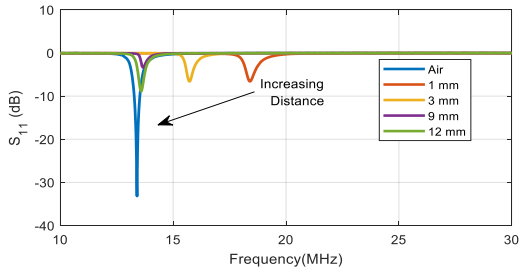

Fig.2. Measured S11 of the test antenna as a function of the frequency for different distance between the tag and mobile.

Fig.3 compares the measured H_{av} and the harvesting output voltage generated by two mobiles as a function of the tag to mobile distance.

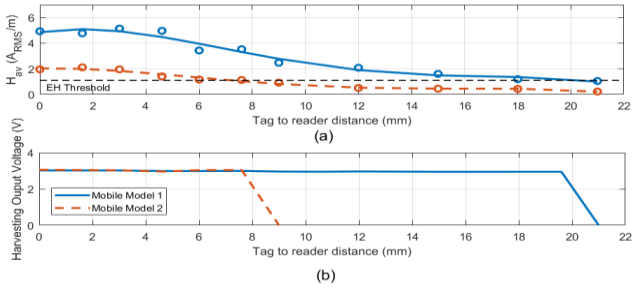

Fig.3. Average magnetic field received by the tag (a) and the rectified voltage (b) as function of the distance between the tag and the reader.

4. Measurements

In order to analyze the behavior of the sensor during the irrigation process a setup with 11 different pots, containing a blended mixture with different quantities of water, from dried soil to 50% of VWC have been set. The result is shown in Fig. 4.

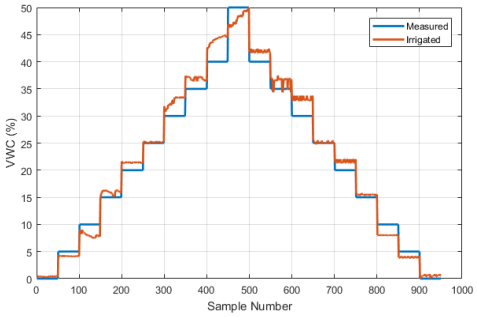

Fig.4. Computed VWC compared to the irrigated water.

An application that runs in Android smartphone (shown in Fig. 5) has been developed as proof of concept. Beyond the sensed data, the system allows to send more information to the reader, such as a link to a website, or it can make use of the user identifier (UID) of each tag to give additional information of that specific product. It also acts as a bridge sending the data to an IoT database.

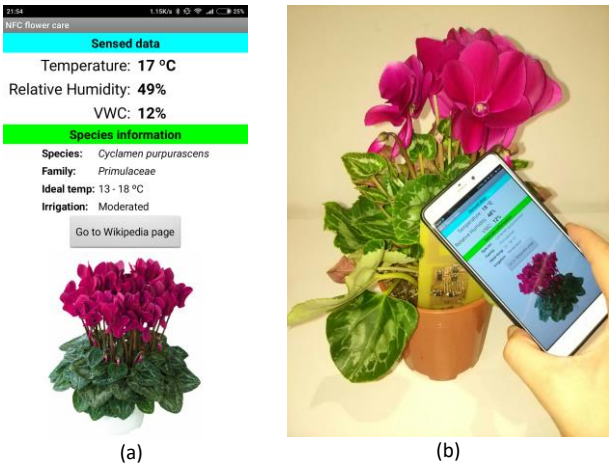

Fig.4. Image of the developed app graphic interface which uses the tag UID to retrieve the information of the plant (a) and the flower pot with the device on it being powered and read by the smartphone (b).

7. Conclusions

This work demonstrates the potential use of NFC to harvest battery-less tags with computational capability. It has been demonstrated that the rectified power generated from the magnetic field is stable enough to supply energy to a microcontroller and a set of chips, allowing carrying out both, analogue and digital communications successfully.

References

[1] NFC Forum: https://nfc-forum.org/

[2] Dobriyal, Pariva, Ashi Qureshi, Ruchi Badola, and Syed Ainul Hussain. "A review of the methods available for estimating soil moisture and its implications for water resource management", Journal of Hydrology, Vol. 458, pp 110-117, 2012.

Degradation of Inverted Polymer Solar Cells using InP-doped PFN as Electron Transporting Layer

A. Sacramento[1], S. Arias[1],V. S. Balderrama[2*], M. Estrada[1], M. Ramírez[1], L. F. Marsal[3,].

[1]Centro de Investigación y de Estudios Avanzados del Instituto Politécnico Nacional (CINVESTAV-I.P.N)
Av. Instituto Politécnico Nacional 2508, 07360 Ciudad de México, México
[2]Cátedra-CONACYT, Center for Engineering and Industrial Development (CIDESI),
Micro-Electro-Mechanical Systems Department (MEMS)
Av. Playa Pie de la Cuesta 702, Desarrollo San Pablo, 76125 Santiago de Querétaro, Querétaro, México
[3]Departament d'Enginyeria Electrònica Elèctrica i Automàtica Universitat Rovira i Virgili
Av. Països Catalans 26, 43007 Tarragona, Spain.
Corresponding author email: * victor.balderrama@cidesi.edu.mx

Abstract

The effects of InP Quantum Dots (QDs)-doped poly[9,9-bis (3 -(N,N-dimethylamino) propyl) - 2,7-fluorene)-alt-2,7-(9,9-dioctylfluorene)] (PFN) layer on the stability and degradation of inverted polymer solar cells based on thieno[3,4-b]-thiophene/benzodithiophene (PTB7) and [6,6]-phenyl-C71-butyric acid methyl ester ($PC_{70}BM$) is presented. Photovoltaic solar cells with inverted structure, using PFN with different InP QDs concentrations (PFN:0 mg/ml InP, PFN:0.22 mg/mL InP and PFN:0.5 mg/mL InP) as electron transporting layer (ETL), were fabricated, after which the degradation of their electrical characteristics under air environment is analyzed. It was observed that the degradation of their performance parameters is 5 times faster than devices without QDs.

1. Introduction

During the last few years, Organic Solar Cells (OSCs) have been extensively researched in order to increase their power conversion efficiency (PCE), which although less than silicon ones, have already reached up to 11 % [1]. Materials, such as Calcium (Ca) and the poly-(3,4-ethylene dioxythiophene):poly-(styrenesulfonate) (PEDOT:PSS) are commonly used as electron transporting layers (ETL) and hole transporting layer (HTL), respectively, in a conventional structure [1]. However, it is well known, that the hygroscopic nature of the PEDOT:PSS and the rapid oxidation of the Ca under air environment can degrade rapidly the active layer, and in consequence, devices have low stability and rapidly degraded. The degradation of the electrical performance of OSCs is a phenomenon that involves chemical and physical processes taking place inside the device, due to the absorption of water and oxygen molecules [3]. The short operation lifetime and rapid degradation of the OSCs are part of their main disadvantages, that need more study, in order to improve their performance, life-time and long term stability. It is common, that metal oxides (e.g. vanadium oxide (V2O5), nickel oxide (NiO) and molybdenum oxide (MoO3)), are used as HTL and zinc oxide (ZnO), PFN, titanium oxide (TiO_2) as ETL in an inverted structure. [4]. On the other hand, Semiconductor Nanocrystals (also known as Quantum dots, QDs) have been considered as promising materials to be analyzed for the next generation of solar cells [5], due to their electronic and optical properties, which are dependent of their size, morphology and composition. [6] In recent years, QDs have been used in the fabrication of optoelectronic devices, such as photodetectors, light emission devices and photovoltaic cells. [7]

In this work, we present the degradation study of the electrical properties of inverted organic solar cells with different concentrations of InP QDs-doped PFN, used as ETL.

2. Experimental and Results

The OSCs were fabricated under N_2 environment on precleaned, patterned ITO glass substrate (10 Ω/square). The PFN interlayer material was dissolved in methanol and mixed with a small amount of acetic acid (2 $\mu l \cdot mL^{-1}$) and different concentrations of InP QDs (PFN:0.22 mg/ml InP and PFN:0.5 mg/ml InP), and its solution (concentration, 2 $mg \cdot mL^{-1}$) was spin-coated on top of the precleaned ITO substrate at 3500 r/min, obtaining a thickness of 10 nm. The PTB7:$PC_{70}BM$ active blend, with a weight ratio of 1:1.5, was dissolved in chlorobenzene (CB) and 1,8-diiodooctane (DIO) (CB:DIO = 97:3 by volume). The blend solution was deposited on top of a PFN layer by spin coating at 800 r/min for 30 s, obtaining the thickness of 100 nm. The anode buffer layers of the cells, consisted of 5 nm of

V_2O_5 and 100 nm of Ag, deposited by thermal evaporation at 1.5×10^{-5} torr at a rate of 0.18 nm/s and 0.1–0.3 nm/s respectively, on top of the active layer. The active area for the devices was 0.09 cm^2, as defined by the geometric overlap between ITO and Ag layers. The devices were measured under air environment during all the degradation process.

The devices were classify into three groups: A (Without InP QDs); B (0.22 mg/ml InP QDs) and C (0.5 mg/ml InP QDs). Afterwards all devices were transferred to ambient conditions, exposed in air environment and kept under dark during all degradation process time of each group of devices (2496 h for A OSC group, 573 h for B OSC group and 551 h for C OSC Group). The three groups of devices were not encapsulated.

Figure 1 shows a typical degradation of J-V characteristics under illumination for A OSC group. The performance parameters obtained from the J-V measurements during all degradation process for A, B and C OSC groups were normalized according the initial values (measured at the initial time of the degradation process). These normalized behaviors, current density (Jsc), open circuit voltage (Voc), fill factor (FF) and power conversion efficiency (PCE) are presented in Figure 2.

Figure 1. Illuminated J-V curves of inverted PTB7:$PC_{70}BM$ solar cells of A OSC group (reference cells) for different degradation times under air environment during 2496 h.

3. Conclusions

Analysis showed, that OSCs with QDs in their electron transporting layer (PFN), degrade 5 times faster than devices without QDs due to the rapid fall of Jsc, FF and PCE. Devices without QDs showed the largest lifetime (2496 h) in comparison of devices with 0.22 mg/ml QDs InP (551 h) and 0.5 mg/ml QDs InP (573 h). Upon exposure to ambient conditions for several days, an s-shape emerged in the J-V curve under illumination for all groups of photovoltaic devices.

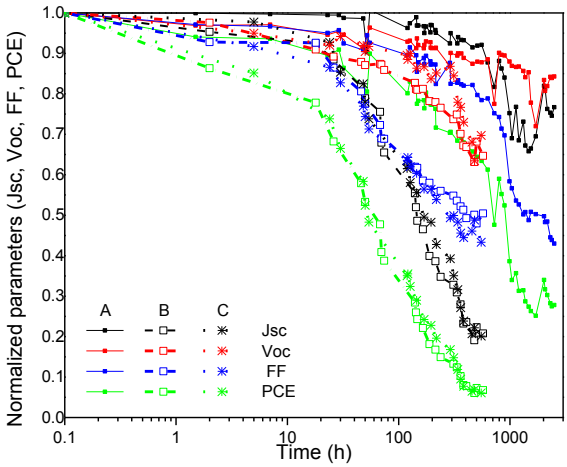

Figure 2. Normalized performance parameters of devices regarding to their initial values as a function of time. J_{SC} is the short current density, V_{OC} is open circuit voltage, *FF* is fill factor and *PCE* is power conversion efficiency. All the devices were measured under AM 1.5G spectrum condition (100mW/cm^2) in air environment.

Acknowledgements

This work was supported in part by CONACYT Project 237213 in Mexico. V. S. Balderrama specially acknowledges to CONACyT project "Cátedras CONACyT para Jóvenes Investigadores". We also acknowledge Ing. L. Abad for support during this work. We give thanks to the Spanish Ministry of Economy and Competitiveness (MINECO-FEDER TEC2015-71324-R) and TEC2015-71915-REDT in part by the Catalan Government 2017-SGR-1527, the ICREA under the ICREA Academia Award.

References

[1] M. A. Green, K. Emery, Y. Hishikawa, W. Warta, E. D. Dunlop, *'Solar Cell Efficiency Tables (Version 48)'*, Prog. Photovolt,: Res. Appl. Vol. 24, pp. 905–913, 2016.

[2] V. S. Balderrama, M. Estrada, P. L. Han, P. Granero, J. Pallarés, J. Ferré-Borrull, and L. F. Marsal, "Degradation of electrical properties of PTB1:PCBM solar cells under different environments," *Sol. Energy Mater. Sol. Cells, vol. 125*, pp. 155–163, 2014.

[3] M. Thambidurai, J. Y. Kim, Y. Ko, H. J. Song, H. Shin, J. Song, Y. Lee, N. Muthukumarasamy, D. Velauthapillai, C. Lee, 'High-Efficiency Inverted Organic Solar Cells with Polyethylene Oxide-Modified Zn-Doped TiO2 as an Interfacial Electron Transport Layer', Nanoscale, vol. 6, pp. 8585-8589, 2014.

[4] Walker, B., Choi, H., & Kim, J. Y. (2017). Interfacial engineering for highly efficient organic solar cells. Current Applied Physics, 17(3), 370-391.

[5] S. Emin, S. P. Singh, L. Han, N. Satoh, A. Islam, 'Colloidal Quantum Dot Solar Cells', Solar Energy, vol. 85, pp. 1264-1282, 2011.

[6] T. Nann, W. M. Skinner, 'Quantum Dots for Electro-Optic Devices', ACS Nano, vol. 5, pp. 5291-95, 2011.

[7] G. H. Carey, A. L. Abdelhady, Z. Ning, S.M. Thon, O. M. Bakr, E. H. Sargent, 'Colloidal Quantum Dot Solar Cells', Chemical reviews, vol. 115, pp. 12732-12763, 2015.

MIS structures and TFT using HIZO and HfO_2 layers both deposited by room temperature RF sputtering.

I. Hernandez[1*], S. I. Garduño[1], M. Estrada[1**]

[1]Centro de Investigación y de Estudios Avanzados del Instituto Politécnico Nacional (CINVESTAV-I.P.N)
Av. Instituto Politécnico Nacional 2508, 07360 Ciudad de México, México
Corresponding authors email: *ihernandezl@cinvestav.mx and **mestrada@yahoo.com

Abstract

Metal-Insulator-Semiconductor (MIS) structure and Thin-Film Transistors (TFTs) using (HfO_2) as dielectric and Hafnium-Indium-Zinc-Oxide (HIZO) as semiconductor, both deposited by room temperature radio frequency (RTRF) magnetron sputtering, are fabricated and characterized using Capacitance-Voltage (C-V) and Current-Voltage (I-V). The HfO_2 dielectric constant was 20 at 1 kHz, the charge carrier concentration of the HIZO was in the range of 5 x 10^{17} cm^{-3} and the interface trap density at flat band was smaller than 8.4x10^{11} cm^{-2}. Results obtained of HIZO TFTs show that they work in the operating voltage range below 2 V, with mobility values above 4 cm^2/Vs.

1. Introduction

The Amorphous oxides semiconductor thin film transistors, (AOSTFTs) have attracted much attention in recent years, due to the highly improved electrical characteristics that they present with respect to amorphous silicon technology [1,2,3]. Blends of amorphous Hafnium-Indium-Zinc-Oxide HIZO and more quaternary compounds of oxide semiconductors as semiconductor layers, provide better electrical parameters and stability than first studied ZnO layers [1,2,3]. Their relatively high mobility values (> 5 cm2/V·s). and stability [4], using low temperature and relatively low-cost processing techniques, allowing their application as switching and/or driving elements in flat-panel displays [2]. They can also be obtained over large areas with uniformity due to its amorphous structure.

However, there is still much work to do to understand the behavior of AOSTFTs fabricated with these materials and learn how to optimize the technological aspects of their fabrication. The characteristics of the semiconductor and dielectric layers strongly depend on the deposition methods used, as well as thermal annealing processes [5].

On the other hand, the use of high-k dielectrics allows the reduction of the operating voltage of the TFT. and contributes to decrease the power consumption. Hafnium oxide (HfO_2) has been used as high-k gate insulator material for this objective.

For the above reasons, in this work, we study the characteristics of MIS structures, and TFTs using HfO_2 as dielectric and HIZO as semiconductor layer respectively, deposited both by RTRF magnetron sputtering. The Capacitance-Voltage (CV) method was used to analyze the characteristics of each layer as well as of the interface between them and predict the operation of TFTs using the same materials and interface. The electrical characteristics of HfO_2/HIZO TFTs fabricated on the same substrate as the MIS structures are also presented.

2. Experimental part

MIS capacitors were fabricated on corning glass substrate. Subsequently, molybdenum (Mo), 150 nm thick, was deposited by RTRF magnetron sputtering as bottom contact. As the dielectric layer, 150±5 nm layer of HfO_2 was deposited by RTRF magnetron sputtering, with 5.7 W/cm^2 of power density at 20 mTorr in argon (Ar). As semiconductor layer, 35±2 nm of HIZO were deposited by RTRF magnetron sputtering with 3.9 W/cm^2 of power density at 8 mTorr in Ar, using a HfO_2:In_2O_3:ZnO target with the ratio of 0.3:1:1 at mol % and 99.98 % of purity. As passivator layer, 400nm of PMMA were deposited by spin-coating. Finally, 200 nm of Mo were deposited by RTRF magnetron sputtering as top contact. All layers were patterned using standard lithography. Thin film Transistors with different channel lengths and widths were also fabricated with the same process on the same substrate, see Fig. 1. Layer thickness was measured by ellipsometry. Capacitance-voltage (CV) and current-voltage (IV) curves were obtained using the Agilent E4980A LCR meter and Keythley measurement system, respectively.

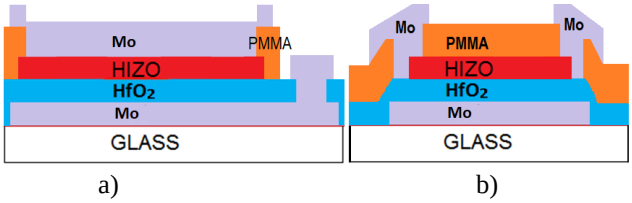

Fig.1. a) MIS structure and b) AOSTFT

3. Results and Discussion

Fig. 2 shows CV curves corresponding to MIS structure, measured in the interval between −2 and 2 V, starting from depletion to accumulation, at different frequencies of the AC signal of the LCR meter. It is seen that devices with this MIS structure can operate in a voltage range below 5 V. Fig. 2 also shows the reduction of the capacitance in accumulation (Caccum), that can be explained by the reduction of k_i with frequency. In addition, the fact that in amorphous oxide semiconductor materials, the carrier response time of the traps, can be high enough, and carriers cannot follow the measurement signal at high frequencies. The simulation of this effect due to the presence of the bulk distribution of localized states, was reported in [6].

Fig.2. CV curves measured at different frequency values of the AC measurement signal of the MIS structure.

From CV measurements, the dielectric constant of the HfO_2 was determined as 20, at 1 kHz. This value is within the reported values, is still sufficiently high to be used to reduce the operating voltage range in TFTs. The flat band voltage is 1.3V. The charge carrier concentration in the HIZO layer was in the order of 5×10^{18} cm^{-3}. The interface trap density at flat band voltage (Nss) was smaller than 8.41×10^{11} cm^{-2}. Fig. 2 also shows modeled curve for 10 kHz. The above mentioned parameters were obtained from the CV curve using the standard method for MIS structures [26].

Fig. 2 also shows a hysteresis loop of less than 1.6 V at 1 kHz, for the CV curves swept in both directions, which can be due to the behavior of the dielectric dipoles of the HfO_2. This is not too high, since the polarizability of a dielectric increases as its k_i increases but must be taken into account when designing applications using these devices.

Fig. 3 shows the output characteristic of an AOSTFT with W=150 µm and L=40 µm, confirming the reduction of the voltage operation range to less than 2 V, VT in the order of 0.5 V and mobility higher around 5 cm^2/Vs. The breakdown voltage for all samples was above 6 V.

Fig.3. Output characteristic of an HfO_2/HIZO TFT.

4. Conclusions

MIS structures using HfO_2 and HIZO layers were fabricated, both deposited by room temperature RF magnetron sputtering, were characterized by CV method, obtaining a relative dielectric constant of 20 at 1 kHz. The charge carrier concentration of the HIZO layer was in the range of 5×10^{17} cm^{-3}. The interface trap density at flat band was smaller than 8.4×10^{11} cm^{-2}. The frequency dispersion of Caccum obtained for MIS structures is observed in this amorphous oxide semiconductor. Fabricated HfO_2/HIZO TFTs presented good electrical characteristics in the operation voltage range below 2 V and mobility higher around 5 cm^2/Vs.

Acknowledgements

This work was supported in part by CONACYT Project 237213 in Mexico. S. I. Garduño specially acknowledges to CONACyT project “Cátedras CONACyT para Jóvenes Investigadores”. We also acknowledge Ing. L. Abad for support during device fabrication and M. C. A. Tavira of Laboratorio de Rayos X of Sección de Electrónica del Estado Sólido, in México.

References

[1] E. Fortunato, P. Barquinha, R. Martins. Oxide Semiconductor Thin-Film Transistors: A review of Recent Advances, Advanced Materials, Vol. 24, Issue 22, 2012, pp. 2945-2986.

[2] H. Kumomi, T. Kamiya, H. Hosono. Advances in Oxide Thin-Film Transistors in Recent Decade and Their Future, ECS Transactions, Vol. 67, Issue 1, 2015, pp. 3-8.

[3] K. Nomura K. Nomura, T. Kamiya, H. Hosono, Hosono, Room-temperature fabrication of transparent flexible thin-film transistors using amorphous oxide semiconductors, Nature 432 (2004) 488–492.

[4] C.-J. Kim, S. Kim, J.-H. Lee, J.-S. Park, S. Kim, J. Park, E. Lee, J. Lee, Y. Park, J. H. Kim, S. T. Shin, U-I. Chung. Amorphous hafnium-indium-zinc oxide semiconductor thin film transistors, Applied Physics Letters, Vol. 95, Issue 25, 2009, pp. 1-3.

[5] L. X. Qian, P. T. Lai. Improved Performance of InGaZnO Thin-Film Transistor With HfLaO Gate Dielectric Annealed in Oxygen, IEEE Transactions on Device and Materials Reliability, Vol. 14, Issue 1, 2014, pp. 177-181.

[6] I. Hernandez, C.A. Pons-Flores, I. Garduño, J. Tinoco, I. Mejia, M. Estrada. Characterization of MIS structures and thin film transistors using RF-sputerred HfO2/HIZO layers, Microelectronics Reliability, Vol. 75, Issue 1, 2017, pp. 9-13.

Compact Modeling of Non-Linear Contact Resistance in Staggered and Coplanar Organic Thin-Film Transistors

Jakob Pruefer[1,2,✠], Benjamin Iñíguez[2], Hagen Klauk[3], Alexander Kloes[1]

[1]NanoP, TH Mittelhessen University of Applied Sciences, Giessen, Germany
[2]DEEEA, Universitat Rovira i Virgili, Tarragona, Spain
[✠]jakob.pruefer@ei.thm.de

***Abstract*—In this paper a compact model for the contact resistance of the metal/semiconductor at source-semiconductor interface in organic thin-film transistors (OTFTs) is presented. The model covers the effects of non-linear current injection and a bias-dependent barrier lowering. These effects are caused by a missmatch between the work functions of contact and organic semiconductor and occur in linear regime of output characteristic. Finally, the model has been validated vs. measurements of fabricated devices.**

I. Introduction

A major advantage of organic materials is the possibility of producing flexible and large-area electronics. In addition, their solubility allows the use of inkjet printers, whereby the production costs are very low. But due to the low mobility of organic materials, a reduction of the channel length is necessary to achieve acceptable drain-source current values. As a result of short channel lengths, new effects such as the s-shape effect appear (Fig. 4(a)) in staggered [1] and coplanar [2] devices where the current is limited in linear regime. This current limitation is caused by the contact resistance which depends on the barrier between source contact and semiconductor. Finally, this contact resistance is dependent on the applied contact potentials, taking into account the Schottky barrier lowering effect.

II. Preliminaries

Prerequisite for this compact model is a not negligible barrier Φ_{B0} between source and semiconductor. Furthermore, this barrier is not constant because it depends on the electric field E_{sb} due to the Schottky barrier lowering effect:

$$\Delta\phi_B(E_{sb}) = \sqrt{\frac{qE_{sb}}{4\pi\epsilon_0\epsilon_r}}. \tag{1}$$

In the case of short channel lengths, the current limitation (s-shape effect) mainly occurs in the linear regime of an output characteristic, since the barrier resistance there is significantly higher than the channel resistance. With increasing V_{ds} the barrier is reduced according to (1) due to an increased electric field E_{sb} and the drain current I_{ds} is modulated by the channel resistance as in a long-channel device.

Therefore, the model assumes in the linear regime that the voltage drop along the channel is negligible, which results in a constant charge distribution in the accumulation channel (Fig. 1).

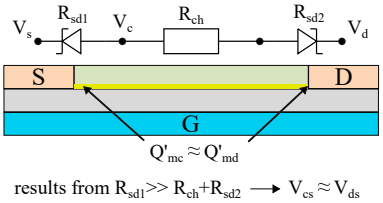

Figure 1: Schematic charge distribution of an n-type OFET in case of on-state ($V_{gs} > V_{T0}$) and linear regime ($V_{ds} << V_{gs} - V_{T0}$).

This approximation leads to a nearly equal charge carrier density at drain and source end of the channel $Q'_{mc} \approx Q'_{md}$. Finally, the general expression for $Q'_{md} = C'_{ox}(V_{gs} - V_{T0} - V_{ds})$ and a fitting parameter f_Q are used by the model, that results for Q'_{mc}:

$$Q'_{mc} = f_Q Q'_{md} = f_Q C'_{ox}(V_{gs} - V_{T0} - V_{ds}). \tag{2}$$

Fitting parameter f_Q accounts for the aforementioned approximation and allows to fit the charge density at the source end of the channel. Q'_{mc} is later required to solve the electric field E_{sb} at the barrier position.

III. Electric Field Solution

An analytical expression for the electric field at the barrier position between source and semiconductor is necessary to calculate the barrier height like in (1).

For the coplanar structure, the Schwarz-Christoffel transformation was used to obtain a conformal map of the examined area in the transistor (hatched area in Fig. 2).

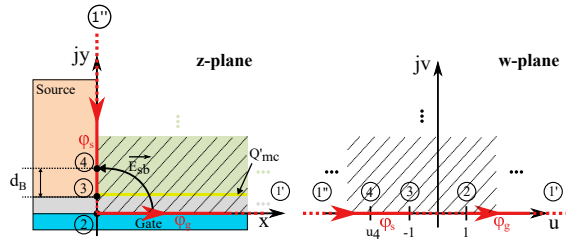

Figure 2: Schematic charge distribution of a n-type OFET in case of on-state and linear regime ($V_{ds} << V_{gs} - V_{T0}$).

This function transforms the complicated geometry from the z-plane into a simpler geometry in the w-plane, for which a solution has already been derived [3]:

$$P(w) = \varphi(w) + j\Xi(w) = \varphi_g + i\frac{\varphi_g - \varphi_s}{\pi}\text{acosh}(w). \quad (3)$$

This potential solution was used to derive an expression for the electric field $E_{sb}(d_B)$, where the fitting parameter d_B defines the distance between point 2 and point 4 along the y-axis (Fig. 2). The position of point 4 defines the point of the average E_{sb} of the injection area. The following expressions were derived for E_{sb}:

$$\text{coplanar: } E_{sb}(d_B) = \frac{2}{\pi} \cdot \frac{\varphi_g - Q'_{mc}/C'_{ox} - \varphi_s}{\sqrt{2d_B\frac{\epsilon_{sc}}{\epsilon_{ox}}t_{ox} + d_B^2}}. \quad (4)$$

In the case of a staggered structure, a 2D solution is not necessary, and can be approximated as a 1D problem (Fig. 3).

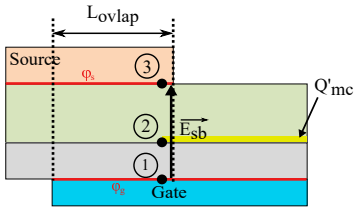

Figure 3: 1D treatment of a staggered structure.

Here, a mapping function is not required to determine a expression for E_{sb}:

$$\text{staggered: } E_{sb}(d_B) = \frac{\varphi_g - Q'_{mc}/C'_{ox} - \varphi_s}{\frac{\epsilon_{sc}}{\epsilon_{ox}}t_{ox} + t_{ox}}. \quad (5)$$

IV. Model Implementation

For the implementation, the current limitation of the barrier is modeled as a resistance, for which the well-known Schottky diode equation (in reverse mode) was used to calculate the respective current:

$$I_{inj} = tWJ_{s0}\exp\left(-\frac{q\Phi_{B0}}{\eta k_B T}\right)\exp\left(\frac{q\Delta\Phi_B}{\eta k_B T}\right), \quad (6)$$

whereby t is the effective injection length (staggered structure: $t = L_{ovlap}$), J_{s0} the current density, Φ_{B0} is the Schottky barrier height and η is a non-ideality factor of Schottky diode equation. Using the corresponding voltage $V_c = V_g - V_{T0} - Q'_{mc}/C'_{ox} - V_s$, the effective contact resistance of the barrier can finally be calculated as follows:

$$R_c = \frac{V_c}{I_{inj}} = \frac{(V_{gs} - V_{T0})(1 - f_Q) + f_Q V_{ds}}{tWJ_{s0}\exp\left(-\frac{q\Phi_{B0}}{\eta k_B T}\right)\exp\left(\frac{q\Delta\Phi_B}{\eta k_B T}\right)}. \quad (7)$$

Further the resistance is incorporated in a first order approximation into the effective mobility [4]:

$$\mu_{eff} = \mu/(1 + \mu\frac{W}{L}R_c Q'_{ms}). \quad (8)$$

V. Verification

In order to verify the compact model, the charge-based compact model of F. Hain [4] is used. For verification, measurement data of staggered and coplanar structures are available with a channel length of 2 µm and 5 µm respectively.

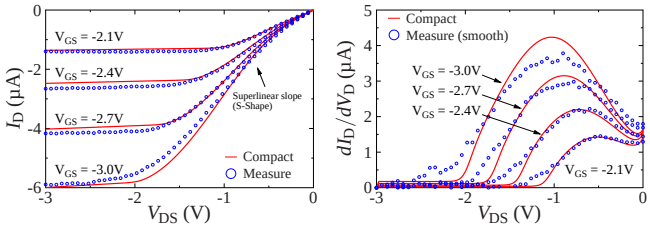

(a) Output characteristic (b) 1st derivative of Fig. 4(a)

Figure 4: Verification of staggered device with $L_{ch} = 2$ µm, $L_{ovlap} = 2$ µm, $t_{ox} = 5.1$ nm, $t_{sc} = 25$ nm, $W = 20$ µm and DNTT as material. [1]

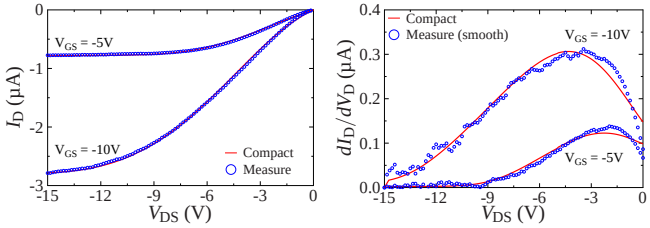

(a) Output characteristic (b) 1st derivative of Fig. 5(a)

Figure 5: Verification of coplanar device with $L_{ch} = 5$ µm, $t_{ox} = 150$ µm, $t_{sc} = 100$ µm, $W = 100$ µm and pentacene as material. [2]

Acknowledgments

The project is funded by the German Federal Ministry of Education and Research ("SOMOFLEX", No. 13FH0151IX6) and EU H2020 RISE ("DOMINO", No. 645760). We acknowledge ATLAS software donation by Silvaco and IC-CAP software by Keysight Technologies.

References

[1] F. Ante, D. Kälblein, T. Zaki, U. Zschieschang, K. Takimiya, M. Ikeda, T. Sekitani, T. Someya, J. N. Burghartz, K. Kern, *et al.*, "Contact resistance and megahertz operation of aggressively scaled organic transistors," *small*, vol. 8, no. 1, pp. 73–79, 2012.

[2] H. Klauk, G. Schmid, W. Radlik, W. Weber, L. Zhou, C. D. Sheraw, J. , A. Nicholas, and T. N. Jackson, "Contact resistance in organic thin film transistors," *Solid-State Electronics*, 2003.

[3] E. Weber, *Electromagnetic Fields: Theory and Applications: Volume I-Mapping of Fields*. John Wiley & Sons, 1960.

[4] F. Hain, M. Graef, B. Iñíguez, and A. Kloes, "Charge based, continuous compact model for the channel current in organic thin-film transistors for all regions of operation," *Solid-State Electronics*, vol. 133, pp. 17–24, 2017.

Design and control of a bidirectional DC/DC converter for an electric vehicle application

Catalina González Castaño, Enric Vidal Idiarte, Javier Calvente

Automatic Control and Industrial Electronics Group (GAEI). Universitat Rovira I Virgili. Avinguda dels Paisos Catalans, 26 Tarragona-Spain.
Email: catalina.gonzalez@urv.cat

Abstract

The aim of this work is the design and the implementation of a digital controller for a DC/DC bidirectional buck-boost converter prototype to regulate DC voltage in a powertrain of an electric vehicle. The DC-DC converter is required to perform two operations: first is keep the different rating voltage between the battery and the inverter, and second deliver power to the motor under acceleration and braking conditions. Thereby, the system works in traction mode to allow power delivered from the battery to the motor and in regenerative brake mode to recharge the battery when the vehicle brakes. A double closed loop digital control is designed to activate the MOSFETS for the DC/DC buck-boost converter, it is composed by multisample average current control and using a PI control method for the external loop. To validate the design output voltage variation reference are simulated in PSIM and implemented in Texas Instruments TMS320F28377S Digital Signal Control (DSC). The results indicate the good agreement with controller designed. Experimental results show its works properly in both modes, keeping the criteria design parameters.

1. Introduction

The DC/DC converter with inductor coupled at the input and the output has been widely used in systems that needs to charge and discharge backup batteries and can be applied in space, fuel cell, photovoltaic and telecom power systems [1], [2], [3], [4]. Therefore, for such applications, the principal function consists in regulate the output voltage of the converter with high stability and efficiency. Using coupled inductor is possible to get wide dc-dc conversion range [5]. On the other hand, one usable solution to eliminate the righthalf- plane (RHP) zero that have the most conventional DC/DC converters in continuous conduction boost mode is using a coupled inductor along with damping networks [2].

Different DC/DC converters topologies has been used to connected the battery with the motor inverter in a high voltage DC bus for Electric Vehicle (EV) application. With the aim to hold the battery rated voltage independent from the high voltage DC bus necessary to deliver power to the moto rand the optimization of vehicle operation. When the battery rated voltage is greater than (buck operation), equal to buck-boost operation), or less than (boost operation) the output voltage from the DC/DC converter. The operating principle are detailed in Figure 1, which consists in a battery and a DC/DC converter block that has as function to keep the different rating voltage between the battery and the inverter to deliver power to the motor. The present work propose a design and implementation to a bidirectional buck-boost converter with coupled inductor prototype studied in [2]. The design of converter was made taking into account the specifications of a powertrain emulator of an electric vehicle. Finally, experimental results are shown, which are developed using an active load in constant resistance mode. Proposed prototype works properly in buck and boost mode, and according with the criteria design, begin a good alternative to start with the application for an electric vehicle operation.

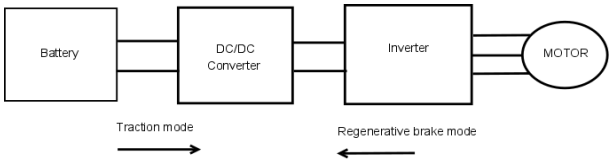

Fig 1. Block diagram of the DC/DC converter in traction system.

3. Buck-boost dc/dc converter with coupled inductor

The buck-boost converter is composed by a *RC* dumping network and a coupled inductor with turns ratio 1:1 and magnetic coupling coefficient $k = 0.5$, as is shown in Figure 2. The buck-boost cell works as follows: u_{1H} and u_{1L} are switched in complementary manner while u_{2H} is set at 1 and u_{2L} is set at 0, in boost mode. In this way, u_{2H} and u_{2L} are switched in complementary manner while u_{1H} is set at 1 and u_{1L} is set at 0, in buck mode. These activation signals are generated using a duty cycle for each operation mode, $d_1(t)$ and $d_2(t)$. This allows to operate in boost mode when Q_1 and Q_2 are switched with the duty cycle $d_1(t)$ and in buck mode when Q_3 and Q_4 are switched with the duty cycle $d_2(t)$.

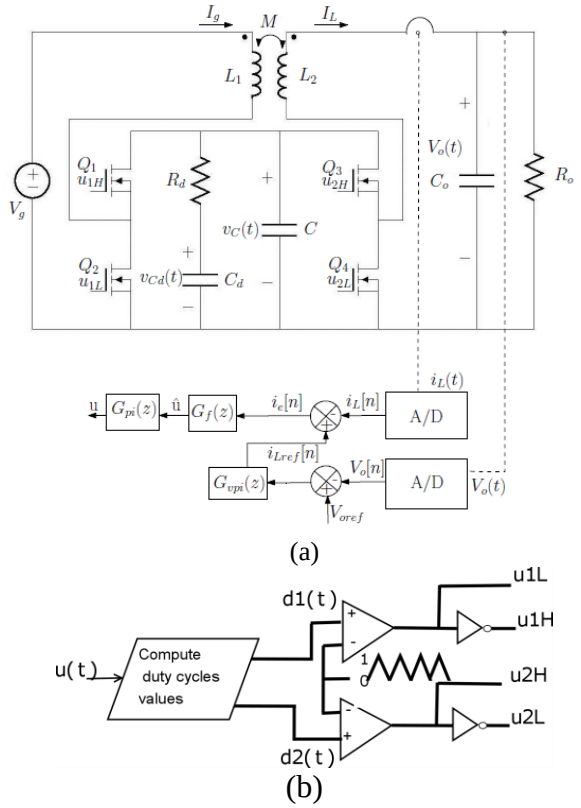

Fig 2. Diagram of: (a) buck-boost converter (b) switch signals generation.

The control method using to regulate the DC voltage output is a double loop, the internal loop is a current control mode and the external loop is a voltage control mode. Figure 2 shows the scheme of the system control; where the external loop determines the reference of the current output of the converter i_{Lref}, taking into account the value sensed of the output voltage. Therefore, the voltage loop generates the current reference. The scheme controller for the power converter consists in a voltage sensor. feedback and a current sensor; two analog-to-digital converter (A/D) that converts the sense signals to a digital number representing the value of the voltage or current. The converted digital value of output voltage is compared whit a reference voltage (V_{oref}) to produce the reference of the current control using a proportional-integral control ($G_{vpi}(z)$). The reference of the current (i_{Lref}) is then compared with the converted digital value of the output current. $G_f(z)$ is a ripple filter of the current with the aim to get the average current value from the error $i_e(n)$. $G_{pi}(z)$ is the transfer function of an integralproportional control that adjusts the cutoff frequency of the current loop to finally get the control variable u.

4. Experimental results

Experiments are carried out over a buck-boost converter prototype described in Figure 2. The selected components are summarized in Table I.

Component	Description
C	Polypropylene Capacitor, 4 x 0.33uF
R_d	Damping resistor, 5Ω, 20W,500V
C_d	Damping Capacitor Polypropylene 20uF, 700V
L_1=L_2	Couple inductor 270 uH
M	Mutual inductance of couple inductor 140 uH
C_0	Polypropylene Capacitor, 6 x 4.7uF

Table 1 Buck-boost cell components.

A direct voltage source is used as power supply for the buck-boost cell. The Enhanced Pulse Width Modulator (ePWM) module from Texas Instruments TMS320F28377S Digital Signal Control (DSC) has been used to generate the activation signals for the MOSFETs switch. Experimental results are showed in Figure 3.

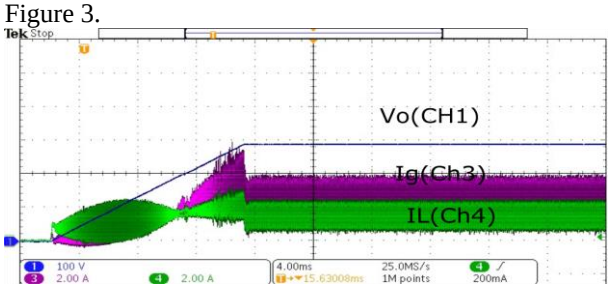

Fig 3. Experimental results with resistor of 200Ω and final output voltage in boost mode. CH3: input current Ig (2 A/div); CH4: current in the load Io (2 A/div); input voltage Vg = 200 V. CH1: output voltage Vo (100 V/div); time base 4 ms.

7. Conclusions

A bidirectional buck-boost converter with coupled inductor, is presented as an alternative to conventional converter topologies in electric vehicle application. A buck-boost cell has been design and validated. Such a prototype has proven to be a suitable for operation in buck and boost mode.

References

[1] S. Inoue and H. Akagi, "A bidirectional dc–dc converter for an energy storage system with galvanic isolation," *IEEE Transactions on Power Electronics*, vol. 22, no. 6, pp. 2299–2306, 2007.

[2] F. Mendez-Diaz, H. Ramirez-Murillo, J. Calvente, B. Pico, and R. Giral, "Input voltage sliding mode control of the versatile buck-boost converter for photovoltaic applications," in *Industrial Technology (ICIT), 2015 IEEE International Conference on*. IEEE, 2015, pp. 1053–1058.

[3] J. Zeng, W. Qiao, and L. Qu, "An isolated three-port bidirectional dc–dc converter for photovoltaic systems with energy storage," *IEEE transactions on industry applications*, vol. 51, no. 4, pp. 3493–3503, 2015.

[4] S.-J. Jang, T.-W. Lee, W.-C. Lee, and C.-Y. Won, "Bi-directional dcd converter for fuel cell generation system," in *Power Electronics Specialists Conference, 2004. PESC 04. 2004 IEEE 35th Annual*, vol.

[5] P. Liya and K. Aathira, "A coupled inductor buck-boost dc-dc converter with wide voltage conversion range," in *Circuit, Power and Computing Technologies (ICCPCT), 2014 International Conference on*. IEEE, 2014, pp. 708–713

NANOPOROUS ANODIC ALUMINA RUGATE FILTERS CHARACTERIZATION BY NUMERICAL MODELLING

F. BERTÓ-ROSELLÓ, L.K. ACOSTA, E. XIFRÉ-PÉREZ, J. FERRÉ-BORRULL, L.F. MARSAL*

Universitat Rovira i Virgili, Avinguda Països Catalans, 26, 43007, Tarragona, Spain

* lluis.marsal@urv.cat

Abstract

A numerical model for the optical properties of nanoporous anodic alumina-based rugate filters (NAA-RF) based on transfer matrix method (TMM) with the effective medium approximation (EMA) is developed. With a best fitting with measured data, a relationship between the geometrical parameters of the structure and the fabrication parameters is established. The design of optical nanostructures could take advantage of this knowledge for future applications.

1. Introduction

The optical, physical and chemical properties of nanoporous anodic alumina (NAA) have boosted the interest in this nanomaterial. In the last years, the NAA properties as biosensing platform for a very wide range of analytes also have gained importance [1]. NAA is produced by electrochemical etching of the aluminum in acidic electrolytes. Achieving a precise control of the fabrication conditions (electrolyte composition, anodization voltage or current, pH and temperature), the geometrical or structural parameters of the NAA (interpore distance (*dint*), pore diameter (*dp*) and pore length (*L*)) can be engineered in a wide range. Additionally, during the anodization the fabrication conditions can be varied in order to modulate the morphology of the pores. As an example, we point out the distributed-Bragg reflectors which can be obtained by the application of successive cycles with high and low anodization voltage [2,3]. Thus, engineering NAA properties is an important move towards its application to fields such as biosensing or photovoltaic energy conversion. A particularly important type of these engineered NAA-based structures is rugate filters. In these nanostructures, the cylindrical pores of NAA have a periodical oscillation of their diameter with the depth, becoming optically as a 1-D photonic crystal structure in which effective refractive index varies continuously and periodically with pore depth. NAA-RFs are produced by applying a sinusoidal anodization current (Eq. 1):

$$I(t) = I_0 + I_1 \sin\left(\frac{2\pi}{T}t\right) \quad (1)$$

where *I0* is an offset current (equivalent to the anodization current in constant current anodization), and *I1* and *T* are the amplitude and period of the sinusoidal component. The resulting pore diameter oscillation can be described by a modulation amplitude in the pore diameter (Δdp) and a modulation period along the pore length (Λ). The geometrical parameters *dint*, *dp*, Δdp and Λ influence the photonic crystal properties such as the position, width and strength of the stop bands.

In this work we develop a tool to numerically simulate the optical properties of NAA-RFs in order to relate the structural parameters with the fabrication parameters (*I0*, *I1* and *T*). In this sense, NAA-RFs were prepared at different fabrication conditions and their reflectance spectra were analyzed by means of the numerical model of the nanostructure. The knowledge of the dependence of the geometrical and optical properties with the fabrication parameters will permit to design further nanostructures and to simulate and predict its behavior in their applications.

2. Experimental and simulation details

The production of NAA-RFs was made with oxalic acid electrolyte, applying sinusoidal anodization profiles according to eq.(1) and following the procedures described elsewhere [4]. Reflectance spectra measurements were obtained from samples were prepared with *I0* = 2.5 mA, 3 mA, 3.5 mA, 4 mA and 5 mA, and with I1 = 2 mA and T = 200 s fixed. Figure 1 depicts a cross-section and top view SEM image of one of the samples. Figure 1.a illustrates the oscillating pattern in depth of the pore diameter. Nevertheless, the pore diameter (*dp*) and its variation in amplitude (Δdp) are difficult to assess from the picture. Figure 2 depicts the model we used for the NAA-RF pores: a pore morphology consisting in a sinusoidal variation of the pore diameter in depth and a modulation period (Λ) along the pore length. This morphology generates a modification in depth of the porosity that results in a modulation of the effective refractive index with the pore

depth (plotted in Figure 3.a). In order to calculate the reflectance spectra we apply the transfer matrix method considering a multilayered thin film model with constant refractive index for each layer. Thereby, we divided in 10 layers with constant index each period in the pore modulation, as illustrated in Figure 3.b. The effective refractive index of each layer is calculated using the Looyenga-Lifshitz-Landau (*3L*) effective medium approximation. The analysis of the reflectance spectra has been done by adjusting the geometrical parameters *dint, dp, Δdp* and Λ, in order to reach the best fit between the experimental and the calculated reflectance. In the computations, we established *dint* = 17 nm/mA· I0 +35 nm and Λ =302 nm/(mA·s)·T·I0, which are estimated from SEM top view pictures and cross-section pictures of prepared samples at the same average current. The value of the pore modulation amplitude was fixed to *Δdp* = 2 nm.

3. Results & discussion

The simulated results are summarized in Figure 4. Figure 4.a shows a comparison of the measured reflectance spectra (black line) for samples with different offset currents (I0) with the corresponding best fittings (red line). The measured spectra show the stop bands as a result of the oscillating variation of the refractive index in the NAA-RF. The central wavelength of each stop band increases for increasing *I0*. The numerical model is able to reproduce the experimental central wavelengths, although with higher calculated maximum reflectance. The reason for this difference is the imperfections in the experimental samples. Figure 4.b depicts the pore diameter obtained from the best fit for each *I0*. Simulation results indicates an increasing trend of *dp* with increasing *I0*, as it could be expected. Further analysis will be made in order to relate the pore modulation amplitude to the current modulation amplitude.

4. Conclusions

In conclusion, a numerical model of NAA-RF based on the effective medium approximation and the transfer matrix method has been developed. This model permits to analyse the measured reflectance spectra and the relationship of the fabrication parameters with the structural parameters of NAA-RF. The model is capable to determine key parameters such as average pore diameter, *dp*, and pore modulation amplitude, *Δdp*. This information could be important when designing further nanostructures and simulating and predicting their behaviour in future applications.

Acknowledgements

This work was supported in part by the Spanish Ministry of Economy and Competitiveness TEC2015-71324-R (MINECO/FEDER), the Catalan authority AGAUR 2014SGR1344, and ICREA under the ICREA Academia Award..

Figures

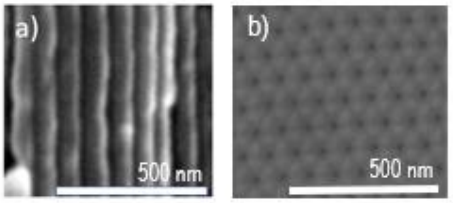

Figure 1. a) Cross-section SEM and b) top view SEM picture of one of the samples (Scale bar: 500nm).

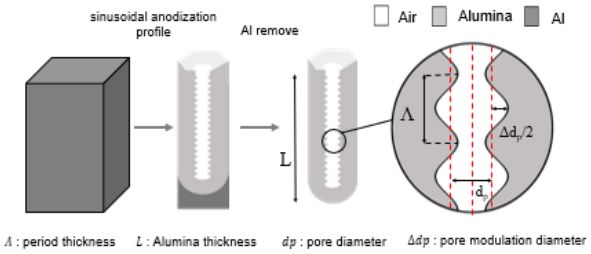

Figure 2. Model for the pore modulation.

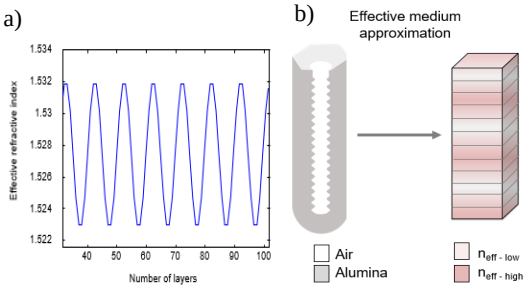

Figure 3. a) Resulting modulation of the effective refractive index with the depth and b) illustration of the division of one period in layers for the transfer matrix method.

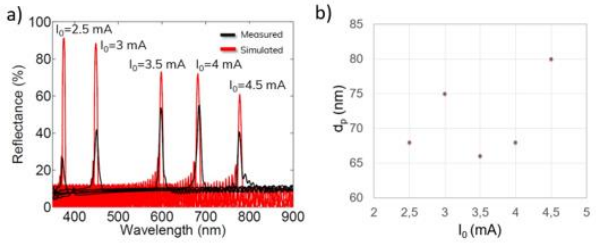

Figure 4. a) Measured reflectance spectra (black) and best fit simulations (red) and b) average pore diameter estimated from the best fit simulations.

References

[1] J. Ferré-Borrull et. al, Nanoporous Alumina: Fabrication, Structure, Properties And Applications; Santos, A., Losic, D., Eds.; Springer-Verlag Berlin, 2015, 185 – 217.

[2] M. M. Rahman, et al, ACS Appl. Mater. Interfaces 2013, 5, 13375−13381.

[3] T. Kumeria et al., Anal. Chem. 2014, 86, 1837-1844.

[4] G. Macias, J. Ferré-Borrull, J. Pallarès and L. F. Marsal, Nanoscale Res. Lett., 2014, 9, 315.

Bidirectional Isolated Low-Power DC-DC Converter for Balancing of Utility-Scale PV Systems

Md. Nazmul Hasan, Carlos Olalla and Luis Martinez-Salamero

Dept. of Electrical, Electronic and Automatic Control Engineering
Escola Tècnica Superior d'Enginyeria, Universitat Rovira i Virgili
mdnazmul.hasan@urv.cat

Abstract - **Differential power processing (DPP) architectures provide significant advantages in the balancing of series connected sources (such as batteries and photovoltaic (PV) systems) including improved efficiency, reduced power rating, and savings in size, weight and cost. Nonetheless, these systems require very simple control methods which must be inexpensive to realize, together with efficiencies above 90 % for the desired range of loads. This paper presents the architecture and control of a bidirectional isolated low-power DC-DC converter which can be used for submodule-level balancing of PV systems. The converter is capable of balancing a range of low-power mismatches with an hysteresis-based open-loop controller that allows burst mode operation in case of very light loads. Experimental results show power transfer efficiencies above 90 % for loads between 500 mW and 5 W.**

I. Introduction

Differential power processing (DPP) has been proposed as an alternative to microinverters and dc optimizers in order to mitigate the effects of mismatch in photovoltaic (PV) systems [1]–[5]. DPP architectures typically feature DC-DC converters named subMICs, which are connected at submodule level and replace bypass diodes. These converters provide a path to different photogenerated currents by simply balancing the voltages of all the submodules in the string. Typically, subMICs are bidirectional converters with unity conversion gain. In addition, the isolated-port architecture in [4] requires galvanic isolation between the input and the output of the converter. In the past, those requirements have been satisfied with simple architectures such as the flyback converter [4] which can be operated in discontinuous conduction mode (DCM) and with closed-loop regulation of the voltages. Although the flyback converter presents poor transformer utilization, it is well-suited for the application, given that transformer use increases with the power level, resulting in conversion efficiencies around 90 % for loads above 2 W. The approach has been demonstrated to be effective in PV plants affected by partial shading, increasing the energy yield of the system by more than 5% [6].

Besides of partial shading mitigation, DPP has also been proposed to reduce the effects of ageing mismatch in unshaded unity-scale PV systems [6]. In absence of shading, only small currents are processed and the low power efficiency of the converter (below 2 W) is even more relevant in this case. Possible converter candidates featuring bidirectional power transfer, isolation and unity gain with open-loop control include the Ćuk and also resonant converters such as the series-resonant (SRC) or the LLC converter. In this context, the Ćuk presents disadvantages related to hard-switching and leakage inductances of the transformer, whereas the resonant converters can operate with soft-switching and can integrate inductors and transformer in the same magnetic core.

This paper presents the architecture and control of a bidirectional isolated low-power DC-DC converter which can be used for submodule-level balancing of PV systems in the isolated-port architecture of [4]. The converter is based on a symmetric version of the LLC resonant tank. Although the converter requires a large number of switches, this approach results in other interesting advantages, including improved light-load efficiency. Besides of zero-voltage switching (ZVS) and integration of the magnetic elements in one single core, the proposed converter can be controlled in open loop with a simple hysteresis band. The inherent dependence of the tank response on the load allows to operate the converter in burst-mode under very light loads and also to automatically limit the power transfer in case of heavy loads. Thanks to this mode of operation, efficiency has been shown to be above 90 % for a range of loads between 500 mW and 5 W.

II. Proposed Topology

In the isolated-port DPP architecture, subMICs must balance the voltages between the primary ports connected to the PV, and the secondary port. In absence of mismatch, submodule voltages are approximately equal, and the converters are simply shut-down. In case of differences between submodules,

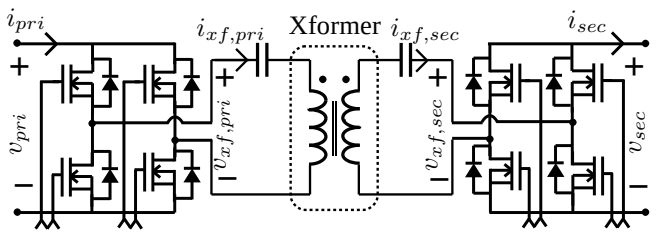

Fig. 1: Proposed symmetric and bidirectional isolated LLC converter.

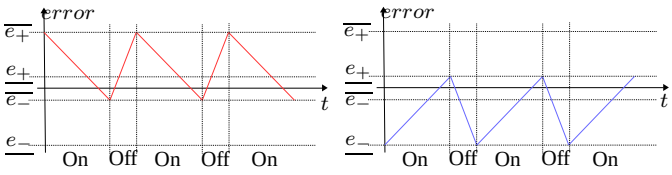

(a) Example of error trajectory in case of power transfer from primary to secondary.

(b) Example of error trajectory in case of power transfer from secondary to primary.

Fig. 2: Double-band hysteresis control limits error and allows burst-mode operation.

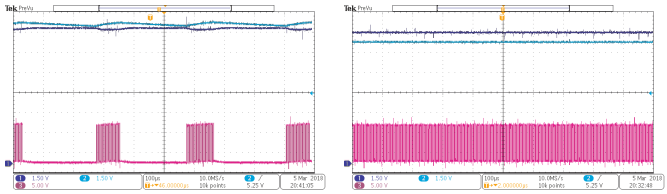

(a) when the load demands 500 mW.

(b) when the load demands 10 W.

Fig. 3: Input voltage (CH1), Output voltage (CH2) and Gate-Source Voltage of a primary side switch.

TABLE I: Efficiency Table.

$P_{in,\text{on}}$	$P_{in,\text{off}}$	P_{out}	η_{on}%	η_{off} %	T_{on}/T	η %
655 mW	526 mW	505 mW	77.1	96.0	.25	91.3
1.23 W	1.03 W	1.01 W	84.8	98.1	.40	91.6
2.29 W	2.08 W	2.05 W	89.5	98.6	.60	93.1
5.92 W	5.18 W	5.15 W	87.0	99.4	.80	89.5
11.64 W	-	9.89 W	85.0	-	1	85.0

the converters operate in the appropriate direction due to the positive or negative voltage difference between the primary and secondary ports.

The power rating of the converter depends on the rating of the submodule. In this paper, a conventional poly-crystalline PV module from Trina (TSM-230PC05) has been considered, which presents a maximum power point of 76 W when the submodule voltage is approximately 10 V. In a previous study [6], it was shown that a converter rated at only 20 % of the submodule power rating could provide full mitigation in the case of ageing related mismatches for 25 years. In consequence, the paper considers that the power rating of the converters is 15 W.

The proposed topology is the resonant LLC symmetric converter shown in Fig. 1. It is assumed that the converter operates at a constant switching frequency f_{sw}, with 50 % duty cycle, such that a square waveform with amplitude equal to the input voltage is seen at the input of the resonant tank. Although the converter requires two full bridges, the circuit takes advantage of the isolation transformer to realize the resonant and magnetizing inductances of the resonant tank.

III. Control scheme

A very simple control approach for the symmetric LLC converter is proposed in this section. SubMICs are controlled independently, balancing the voltages between the primary and secondary ports. When the primary voltage is higher than the secondary voltage, power is transferred from primary to secondary. Similarly, if the primary voltage is lower than the secondary, power is transferred in the opposite direction. Considering $error = v_{pri} - v_{sec}$, Fig. 2 shows the double-band hysteresis regions and two example trajectories of the error. One of the full bridges is activated at the switching frequency, while the other full-bridge acts as a non-active rectifier. If the converter is switched at the resonant frequency, the input-output gain is approximately one, and only enabling the appropriate full-bridge, subMICs balance voltages between the primary and secondary ports. Nonetheless, we propose to operate below the resonant frequency, such that the output voltage can be higher than the input (light loads) or lower than the input (heavy loads).

IV. Experimental Results

The performance of the converter has been verified with a range of loads between 500 mW and 10 W. Fig. 3 shows the input voltage (CH1), output voltage (CH2) and one of the primary port driver outputs (CH3) for a power transfer of 500 mW and 10 W. In Fig. 3(a), it can be seen that the output voltage rises above the input voltage and that the switching of the converter stops when the error goes above the threshold. This results in an ON/OFF ratio of approximately 25 %. At 10 W (Fig. 3(b)), the output voltage is slightly lower than that of the input voltage and the converter is always ON.

The efficiency of the converter for the loads shown above can be observed in Table I. The table presents estimates of the input power when the converter is on and off, together with the output power and the corresponding partial efficiencies η_{ON} and η_{OFF}. Thanks to the burst mode, the 500 mW load exhibits an overall efficiency of 91 %. Efficiency increases up to 93 % for a 2 W load, and then it decreases to about 85 % for the 10 W load.

References

[1] P. S. Shenoy, K. A. Kim, B. B. Johnson, and P. T. Krein, "Differential power processing for increased energy production and reliability of photovoltaic systems," *IEEE Transactions on Power Electronics*, vol. 28, no. 6, pp. 2968–2979, 2013.

[2] Y. Nimni and D. Shmilovitz, "A returned energy architecture for improved photovoltaic systems efficiency," in *Circuits and Systems (ISCAS), Proceedings of 2010 IEEE International Symposium on*, pp. 2191–2194, IEEE, 2010.

[3] J. Stauth, M. Seeman, and K. Kesarwani, "A high-voltage cmos ic and embedded system for distributed photovoltaic energy optimization with over 99% effective conversion efficiency and insertion loss below 0.1%," in *Solid-State Circuits Conference Digest of Technical Papers (ISSCC), 2012 IEEE International*, pp. 100–102, IEEE, 2012.

[4] C. Olalla, D. Clement, M. Rodriguez, and D. Maksimovic, "Architectures and control of submodule integrated dc–dc converters for photovoltaic applications," *IEEE Transactions on Power Electronics*, vol. 28, no. 6, pp. 2980–2997, 2013.

[5] T. Shimizu, M. Hirakata, T. Kamezawa, and H. Watanabe, "Generation control circuit for photovoltaic modules," *IEEE Transactions on Power Electronics*, vol. 16, no. 3, pp. 293–300, 2001.

[6] C. Olalla, C. Deline, D. Clement, Y. Levron, M. Rodriguez, and D. Maksimovic, "Performance of power-limited differential power processing architectures in mismatched pv systems," *IEEE Transactions on Power Electronics*, vol. 30, no. 2, pp. 618–631, 2015.

Inverted Organic Solar Cells of PTB7:PC70BM Using HIZO as Cathode Buffer Layer.

M. Ramírez-Como[1*], V. S. Balderrama[2**], A. Sacramento-Orduño[1], L. F. Marsal[3], and M. Estrada[1].

[1]Centro de Investigación y de Estudios Avanzados del Instituto Politécnico Nacional (CINVESTAV-I.P.N)
Av. Instituto Politécnico Nacional 2508, 07360 Ciudad de México, Mexico.
[2]Center for Engineering and Industrial Development (CIDESI), Micro-Electro-Mechanical Systems Department (MEMS), Av. Playa Pie de la Cuesta 702, Desarrollo San Pablo, 76125 Santiago de Querétaro, Querétaro, Mexico.
[3]Departament d'Enginyeria Electrònica Elèctrica i Automàtica Universitat Rovira i Virgili
Av. Països Catalans 26, 43007 Tarragona, Spain.
Corresponding authors email: *magaly.ramirez@cinvestav.mx and **victor.balderrama@cidesi.edu.mx

Abstract

We studied the effects of Hafnium-Indium-Zinc-Oxide (HIZO) as cathode buffer layer into inverted bulk heterojunction polymer solar cells, based on Thieno[3,4-b]thiophene/benzodithiophene (PTB7) and [6,6]-phenyl-C71-butyric acid methyl ester ($PC_{70}BM$). We studied the devices using the current density-voltage (J-V) characteristic and modeled these devices through the three-diode equivalent circuit model. Some devices were fabricated using poly [(9,9-bis (30- (N,N-dimethylamino) propyl) -2,7-fluorene) -alt-2,7- (9,9-dioctylfluorene)] (PFN) as cathode buffer layer as control samples. The highest PCE was obtained for a thickness of 2.6 nm of HIZO.

1. Introduction

The polymer solar cells (PSC's) have attracted much attention in recent years by the advantages they present such as low-cost, as well as the possibility of their application to large area flexible substrates and flexibility [1]. In order to improve the performance and stability, inverted structure (iPSC) have been developed and buffer layers with low work function metal electrodes have been introduced. TiO_2, ZnO and Cs_2CO_3 have been used in inverted structures as cathode buffer layer (CBL) [2]. Zn-based transparent semiconductor oxides has been widely used, because they present good transparency associated with large bandgap energies (Eg), usability in low-temperature processes, large-scale fabrication feasibility, and sensitivity to gas molecule [3]. The Hafnium component in these materials imped charge carrier generation and can suppress the dissociation of HIZO due to the nature of Hf atoms, which have a high electronegativity difference with Oxygen, as a result can form stronger bonds with it supply good stability [4]. In current–voltage characteristics it has been observed that some devices show a kink-shaped curve. This phenomenon can be reproduced with the three-diode model as was reported in [5]. The kink-shape is associated to the presence of barriers between cathode (anode) and active layer, due to the difference mobility of charge carriers, to the creation of traps, and/or to strong interfacial dipoles [6].

In this work, we present the use of HIZO as CBL. The devices were based on the blend of Thieno[3,4-b]thiophene/benzodithiophene (PTB7) and [6,6]-phenyl- C71-butyric acid methyl (PC70BM). The devices were fabricated partially under air environment. In order to study the effects of HIZO on the iPSC performance, density current-voltage (J-V) characteristic were modeled using the three-diode model. In addition, iPSCs with PFN as CBL were fabricated as control samples under the same environment.

2. Experimental and Results

The blend solution was prepared dissolving PTB7 and PC70BM with a weight ratio of 1:1.5 in a solvents mix of chlorobenzene (CB) and 1,8-diiodooctane (DIO) (CB:DIO = 97:3 by volume) to get 25 mg/mL of the total solution. The solution was left stirring and heating under nitrogen atmosphere at 45 °C overnight. The HIZO interlayer was deposited by RF magnetron sputtering, using a single target (with composition HfO_2:In_2O_3:ZnO = 0.3:1:1 mol%). The iPSC were fabricated on ITO-coated glass. The deposition of HIZO was done in an atmosphere of Ar at room temperature. For devices as control, the PFN interlayer material was dissolved in methanol (1.84 mg/mL) using as additive acetic acid (1.84 µl/mL). The solution was spin-coated on an ITO substrate at 4200 rpm for

60 s. Subsequently, blend solution was spin-cast on top of the HIZO and PFN layers, at 750 rpm for 30 s. Finally, 5 nm of V_2O_5 followed by 100 nm of Ag, were thermally evaporated on the active layer in a vacuum chamber outside of the glove box.

Figure 1 shows the inverted polymer solar cells (iPSC) fabricated. The performance parameters are shown in Table 1, which summarizes the open circuit voltage (VOC), short circuit current density (JSC), fill factor (FF) and power conversion efficiency (PCE) of the iPSC's using HIZO as CBL. The sample, with a thickness of 2.6 nm, exhibited the highest PCE. The sample presents a value of J_{SC} similar to the one obtained for PFN-iPSC. The J-V curves, just after fabrication, were modeled using the three-diode equivalent circuit model shown in the Fig. 2. Table 2 shows the parameters extracted from the model. The predominant transport mechanism in both kind of devices is recombination. The kink-shape becomes more pronounced with HIZO-iPSC than with PFN-iPSC. However, the kink-shape disappears quickly for HIZO-iPSC. This is due to the presence of ZnO in the HIZO, which can absorb oxygen molecules that can act as surface trap states. Therefore the concentration of the free electron carriers increases due to the desorption of molecular oxygen.

3. Conclusions

We showed an inverted solar cell based on PTB7:PC70BM using HIZO as the CBL. The PCE of HIZO-iPSC was 4.77%, with a V_{OC} of 678 mV and J_{SC} of 18.1 mA/cm^2. Using a three-diode equivalent circuit the current–voltage curves just after fabrication were modeled. The S-shape disappeared more quickly for HIZO-iPSC, due to desorption of molecular oxygen. Finally, we showed the effect of the HIZO thickness on performance of iPSC, suggesting that it is possible to optimize it in order to increase even more the PCE.

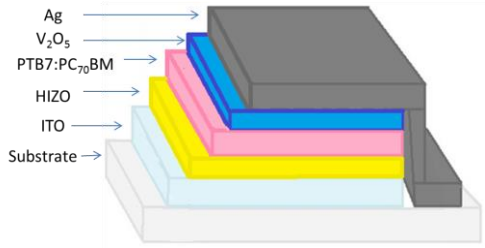

Fig.1. Inverted polymer solar cells with HIZO as CBL.

ETL	V_{OC} (mV)	J_{SC} (mA cm^{-2})	FF (%)	PCE Best (%)
HIZO 2.0 nm	725	14.01	38.59	3.92
HIZO 2.4 nm	630	13.40	37.59	3.17
HIZO 2.6 nm	678	18.10	38.86	4.77
PFN	754	18.63	53.32	7.49

Table1. Performance parameters of the PTB7:PC70BM PSCs.

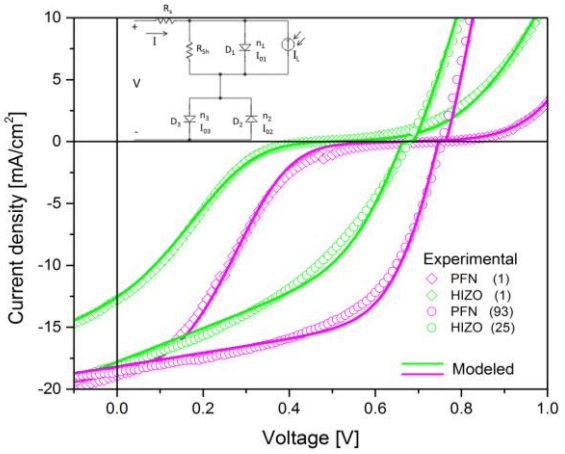

Fig.2. Modelling of current-voltage characteristic.

ETL	*Measurement*	n_1^a	n_2^b	n_3^b
HIZO 2.6 nm	1	1.95	1.9	2.5
HIZO 2.6 nm	25	1.95	-	-
PFN	1	1.95	1.8	2.5
PFN	93	1.95	-	-

Table2. Parameters obtained from circuital model.

Acknowledgements

This work was supported by the Consejo Nacional de Ciencia y Tecnología (CONACYT) under the Project 237213 in Mexico. The work of Victor S. Balderrama (ID Researcher 7340 and CVU-227699) was supported by "Cátedra-CONACYT para Jóvenes Investigadores" under the Call 2017 from the project number II "Strengthening Scientific Capacity and Human Capital for the Development of MEMS for the Industry" in Mexico. We give thanks to the Spanish Ministry of Economy and Competitiveness (MINECO-FEDER TEC2015-71324-R) and TEC2015-71915-REDT in part by the Catalan Government 2017-SGR-1527, the ICREA under the ICREA Academia Award.

References

[1] K. Wang, C. Liu, T. Meng, C. Yi and X. Gong., "Inverted organic photovoltaic cells", *Chem. Soc. Rev.*, Vol. 45, pp. 2937–2975, 2016.

[2] S. H. K. Park, C. S. Hwang, M. Ryu, S. Yang, C. Byun, J. Shin, J. I. Lee, K. Lee, M. S. Oh, and S. Im, "Transparent and photo-stable ZnO thin-film transistors to drive an active matrix organic-light-emitting-diode display panel", Adv. Mater., Vol. 21, pp. 678–682, 2009.

[3] J. G. Sánchez, V. S. Balderrama, S. I. Garduño, E. Osorio, A. Viterisi, M. Estrada, J. F. Borrull, J. Pallarès and L. F. Marsal, "Impact of inkjet printed ZnO electron transport layer on the characteristics of polymer solar cells", RSC Adv., Vol. 8, pp. 13094–13102, 2018.

[4] A. Thakura, S. J. Kang, J. Y. Baik, H. Yoo, I. J. Lee, H. K. Lee, S. Jung, J. Park and H. J. Shin, "Blue shift in the optical band gap of amorphous Hf–In–Zn–O thin films deposited by RF sputtering", J. Alloy Compd., Vol. 525, pp. 172– 174, 2012.

[5] F. Garcia-Sanchez, D. Lugo-Muoz, J. Muci and A. Ortiz-Conde, "Lumped parameter modeling of organic solar cells s-shaped I–V characteristics". IEEE J. Photovolt., Vol. 3, pp. 330–335, 2012.

[6] A. Gusaina, S. Singhb, A. K. Chauhana and V. Saxenaa, "Electron density profile at the interfaces of bulk heterojunction solar cells and its implication on the S-kink characteristics", Chem. Phys. Lett., Vol. 646, pp. 6–11, 2016.

Efficiency optimization of a variable bus voltage DC microgrid

D. García Elvira, H. Valderrama Blaví, A. Cid Pastor, J.M. Bosque Moncusí, L. Martínez Salamero
Departament d'Enginyeria Electrònica, Elèctrica i Automàtica.
Universitat Rovira i Virgili (URV). Tarragona (Espanya). Email: david.garciae@urv.cat

Abstract

A variable bus voltage DC microgrid (MG) is simulated in Matlab for optimization purposes. The starting point is this MR being controlled with a Voltage Event Control (VEC) algorithm.

Two strategies are evaluated for improving the DC/DC converters efficiency. First, a hierarchic controller, manages the battery power in order to make the bus voltage follow the optimal voltage reference. And second, each converter is controlled distributedly to operate at the optimal switching frequency.

Index Terms *— Efficiency optimization, DC microgrid, Voltage Event Control, Variable switching frequency, Hierarchical vs. distributed control.*

1. Introduction

Microgrids (MG) are receiving increasing attention as electrical power systems tend to de-centralization.

MG management is a key issue to improve energy efficiency, to extend battery lifetime and to achieve maximum economic yield.

2. Description of the MG

The studied MG is based on the one described in [1]. Its elements and configuration are shown in Table 1 and Fig. 1. Every element is connected to the DC bus through a DC/DC converter controlled as a power source.

Sources	PV: Photovoltaic WT: Wind Turbine	FC: Fuel cell
Loads	LOAD: DC charges	EZ: Electrolyzer
Bidirectional elements	BESS: Battery Energy Storage System	INV: Bidirectional inverter

Table 1. MG elements

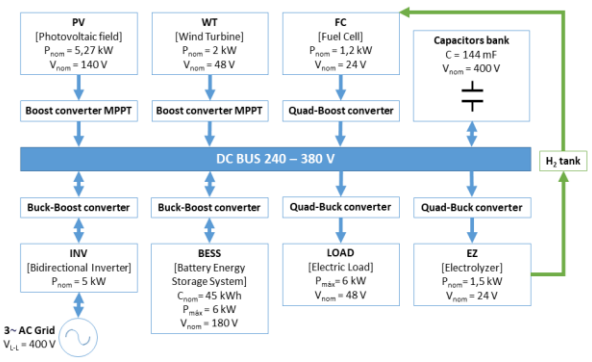

Fig. 1. MG block diagram

Initial control (C_0) of the MG consists of a distributed Voltage Event Control (VEC). Each element follows the control laws shown in Fig. 2.

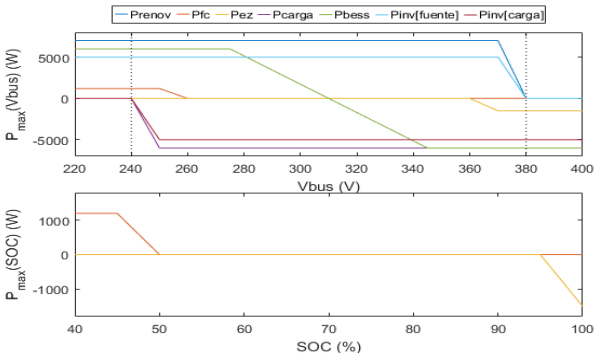

Fig. 2. Initial control laws (C_0)

In order to make the system stable, the power of renewable energy sources (RES) is limited when bus voltage is too high (over 370 V), and the power of loads is limited when bus voltage is too low (under 250 V). BESS power equilibrates the system around 310 V. When the battery State of Charge (SOC) reaches either high (95 %) / low values (50 %), hydrogen production / consumption is activated. The inverter will only work if the BESS fails.

While most MG management works focus on economic optimization (e.g. [2]), this article proposes, instead, two strategies for efficiency optimization: optimal bus voltage (C_{1V}) and optimal switching frequency (C_{1f}).

3. Bus voltage optimization (C_{1V})

The goal is keeping the bus voltage at its optimal value (v_{optim}) in every moment. A centralized Energy Management System (EMS) calculates v_{optim} and determines the power that the BESS must perform.

The EMS gathers sensors' readings of input and output voltages and currents from all the converters. Given the instantaneous power flows existing in the MG, the EMS evaluates an online loss model of each one of them. An optimization function (*fminbnd*, in Matlab) returns the value of bus voltage (v_{bus}) that is a minimizer of the sum of converters' power losses (P_{loss}^{MR}) inside the indicated interval (eqs. (1) and (2)):

$$v_{optim} = \min_{250\,V \le v_{bus} \le 370\,V} P_{loss}^{MR}(v_{bus}) \quad (1)$$

$$P_{loss}^{MR}(v_{bus}) = P_{loss}^{PV}(v_{bus}) + P_{loss}^{WT}(v_{bus}) + P_{loss}^{FC}(v_{bus}) + P_{loss}^{LOAD}(v_{bus}) + P_{loss}^{EZ}(v_{bus}) + P_{loss}^{BESS}(v_{bus}) + P_{loss}^{INV}(v_{bus}) \quad (2)$$

Losses are calculated using small-signal models of the converters. As an example, the expression for PV power loss (P_{loss}^{PV}) is provided in eqs. (3) to (5). The equations for the rest of converters are analogous.

$$\eta = v_{OUT} i_{OUT} / v_{IN} i_{IN} \quad (3)$$

$$d = (v_{bus} - v_{IN}\eta\,)/v_{bus} \quad (4)$$

$$P_{loss}^{PV} = \{R_L i_{IN}^2 + K(\Delta b(d)/2)^{\beta} f_{SW}^{\alpha}\}_{inductor} + \{(1-d)(R_D i_{IN}^2 + V_F i_{IN})\}_{diode} + \{d(R_D i_{IN}^2 + V_F I_{IN}) + (0.5 v_{bus} i_{IN} T_{SW} f_{SW})\}_{igbt} \quad (5)$$

With the reference v_{optim}, a PI controller determines the BESS power. When battery capacity is sufficient, the system will be able to operate at optimal bus voltage (while maximizing RES contribution and minimizing load disconnections, thanks to the VEC still present in unidirectional elements).

4. Switching frequency optimization (C_{1f})

Converters incorporate a controller that imposes their respective optimal switching frequencies (f_{optim}^{i}). f_{optim}^{PV} calculation is shown in eqs. (6) to (8):

$$f_{optim}^{PV} = \min_{3\,kHz \le f_{sw} \le 50kHz} P_{pérds}^{PV}(f_{sw}) \quad (6)$$

$$D = (v_{OUT} - v_{IN} \cdot \eta\,)/v_{OUT} \quad (7)$$

$$P_{loss}^{PV} = \{R_L i_{IN}^2 + K(\Delta b(f_{sw})/2)^{\beta} f_{sw}^{\alpha}\}_{inductor} + \{(1-D)(R_D i_{IN}^2 + V_F i_{IN})\}_{diode} + \{D(R_D i_{IN}^2 + V_F I_{IN}) + (0.5 v_{bus} i_{IN} T_{SW} f_{sw})\}_{igbt} \quad (8)$$

5. Simulation results

Simulation illustrates MG operation during 7 days, including simulation of failures of several elements. The purpose is showing that C_{1V} and C_{1f} work as expected, as well as they maintain C_0 robustness, even facing failures.

Efficiency improvement is calculated to assess which optimization strategies are worth of implementation. Results are depicted in Table 2:

Control	$\Delta\eta_{global}$ respect to C_0	
	Simulating failures in BESS, PV, WT & INV $\eta_{global\,C_0} = 88{,}6221$ %	**No failures** $\eta_{global\,C_0} = 88{,}8345$ %
$C_1 = C_{1V}+C_{1f}$	0.6490 %	0,7706 %
C_{1V} (fixed f_{sw}^{i})	0.0906 %	0,1410 %
C_{1f}	0.5469 %	0,6166 %

Table 2. MG global efficiency under various control algorithms during a 7 days' simulation

Results show that efficiency improvements achieved with both strategies are lower than 0,8 %. Control C_{1V} obtains an exiguous efficiency rise and, moreover, it is difficult to implement (it performs complex calculation and requires communicating the EMS with all the MG's converters). Control C_{1f}, for its part, leads to better results, being easier to implement.

C_{1f} alone is thus preferred. Stability and dynamics of the MG controlled with C_{1f} are shown in Fig. 3.

6. Conclusions

Bus voltage optimization and switching frequencies optimization have been simulated resulting in low efficiency improvements. Utilizing the latter is suggested, although some future research work must be done to introduce active filtering.

References

[1] J. M. Bosque-Moncusi, «Ampliación, mejora e integración en la red de un sistema fotovoltaico», Universitat Rovira i Virgili, 2015.

[2] J. M. Lujano-Rojas, R. Dufo-Lopez, J. L. Bernal-Agustin, y J. P. S. Catalao, «Optimizing Daily Operation of Battery Energy Storage Systems Under Real-Time Pricing Schemes», *IEEE Trans. Smart Grid*, vol. 8, n.º 1, pp. 316-330, 2017.

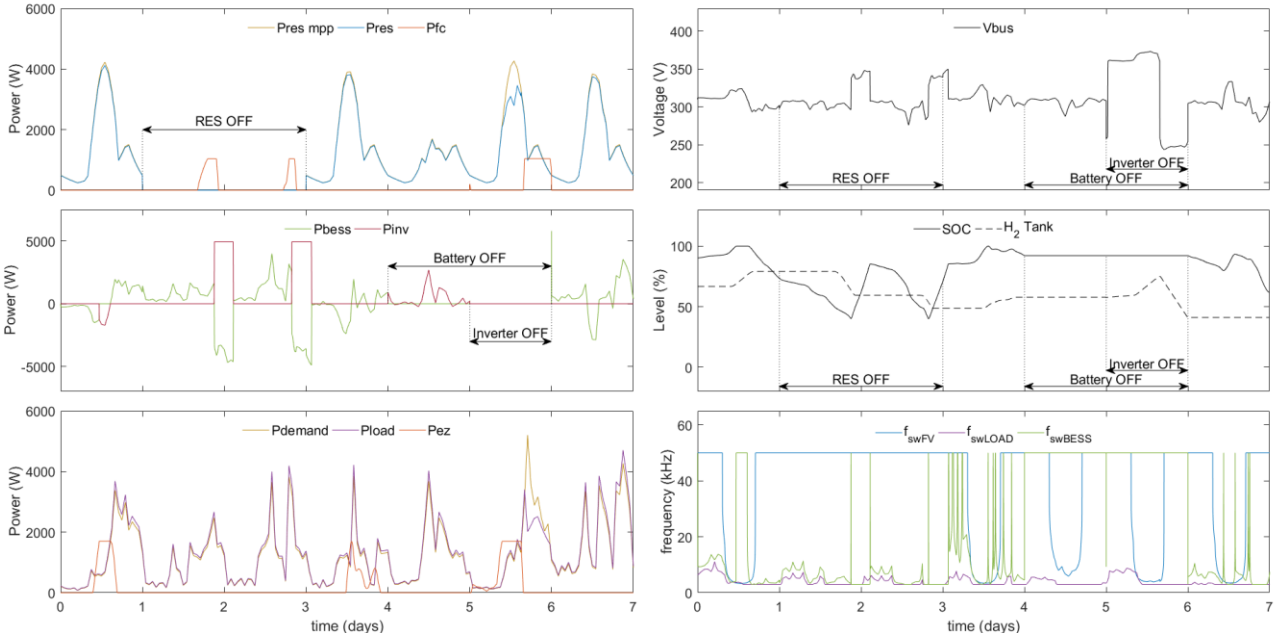

Fig. 3. MG operation during 7 days, under C_{1f} control

Fabrication and characterization of hydrogen sulfide sensor based on silver doped tungsten trioxide

E. González[1], E. Navarrete[1], E. Llobet[1]

1. Minos-EMaS, Departament d'Enginyeria Electrònica, Elèctrica i Automàtica
Universitat Rovira i Virgili
Tarragona, Spain
ernesto.gonzalez@urv.cat

Abstract

In this work we present the manufacturing process and characterization of a hydrogen sulfide sensor based on silver doped tungsten trioxide (WO_3) nanoneedles (NNs), using chemical vapor deposition (CVD) and sputtering with one and two steps synthesis procedures. Morphological characterization and sensor response to different H_2S concentrations with different operating temperatures are presented.

1. Introduction

In our atmosphere there are some natural and anthropogenic gases which are harmful to human health and the environment and, because of this we need to take a control on their concentration in some environments, in order to get an alarm when detected at too high concentrations in protected or potentially explosive atmospheres [1]. Gas sensors are devices which are able to quantify gas concentration in situ, generating an electric or optic signal, which changes in accordance with concentration. Among gas sensors, chemical sensors are transducers with a chemically active layer which is sensible to one or some gases. Chemo-resistive properties of metal oxides, their high temperature resistance and being catalytically active materials, made them highly used materials in gas sensing applications [2]. Metal oxide based gas sensors have their operating principle on redox reactions taking place between target gas and metal oxide surface. During this reaction, O^- ions distributed on the surface react with molecules of the target gas, generating a change in electric resistance which is monitored to characterize the sensor performance [3]. Controlled synthesis of nanostructures, its shape, size, crystallographic structure and distribution, allows to improve sensitivity and selectivity of the sensors [4]. On the other hand, doping with noble metals, such as Au, Pt, Pd and Ag, which act as catalysts of the reactions that occur on the surface of the metal oxide, modifies the sequence and the speed of the reaction, generating an increase in detection limits, as well as improving the selectivity of the material to specific gases [2, 5]. In this work we use aerosol assisted chemical vapor deposition (AACVD) and sputtering to synthesize silver doped WO_3 nanoneedles using one and two steps procedures. Morphologic characterization and phase composition analysis of sensors was carried out using environmental scanning electron microscope (ESEM), transmission electron microscope (TEM) and X-ray diffraction (XRD).

2. Experimental

We use AACVD as synthesis method to obtain WO3 nanoneedles, using 50 mg of tungsten hexacarbonyl $W(CO)_6$ precursor, with a mixture of 15 ml of acetone and 5 ml of methanol. In order to generate vapor from precursors we used an ultrasonic atomizer and a flow of 1 l/m of nitrogen N2 as carrier gas. In order to realize the silver doping, we used two different ways. First we used AACVD with 6 mg of silver acetylacetonate Ag(acac) as precursor in 10 ml of methanol as solvent. Second doping method was magnetron RF sputtering, modelo ATC Orion 8-HV de AJA International, with a power of 150 W during 10 and 20 sec. On the other hand, a simple step process was used by mean of a mixture of $W(CO)_6$ and Ag(acac) precursors with 16 ml of acetone and 4 ml methanol solvents. Tabla 1 shows temperatures and precursor and solvent quantities used in deposition processes.

Sample		Temp. [ºC]	Precursor weight [mg]	Solvent vol. [ml]
Ag6-2st	1	400	W(CO)6,50	acetone, 15 methanol, 5
	2	380	Ag(acac), 6	methanol, 10
Ag6-1st pure WO_3		380	W(CO)6,50 Ag(acac), 6	acetone, 15 methanol, 5

Table 1. Deposition details.

After each deposition step, sensors were subjected to an annealing process at 500 ºC during 2 h.

By means of ESEM FEI Quanta 600 with an operating voltage of 20 kV and TEM JOEL JEM 1011 with an operating voltage of 100 kV we obtained images of the sensors´ surface in order to characterize the sensors morphologically and XRD analysis were made to obtain information about sensors´ composition in a Bruker-AXS D8-Discover, operated at 40 kV and 40 mA with Cu_{ka} radiation.

Gas sensing test were made in a Teflon/stainless chamber under 100 sccm constant gas flow. Resistance changes were measured and stored via Agilent 34970A data acquisition system. Calibrated bottles were used to program the desired gas concentration, driven by a Bronkhost Hitech 7.03.241 mass flow controller system. Operating temperatures of the sensors were set by means of an Agilent E3631A power supply connected to the sensors´ heaters. By setting the current flow by the heater we establish the operating temperatures of the sensors in order to look for the best behaviour and responses of them.

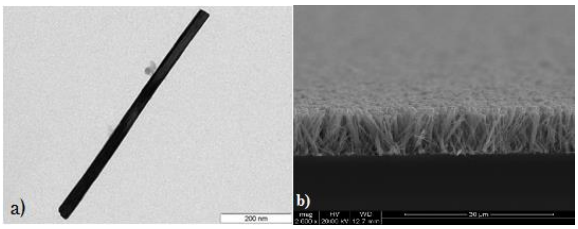

Fig.1. a) TEM image of a single nanoneedle. b) ESEM image of the WO_3 nanoneedle deposition on silicon.

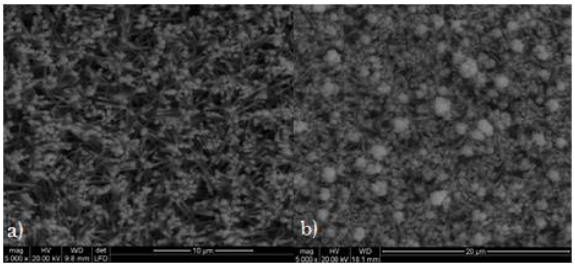

Fig.2. ESEM images of WO_3 nanoneedles doped by sputtering (a) and AACVD (b).

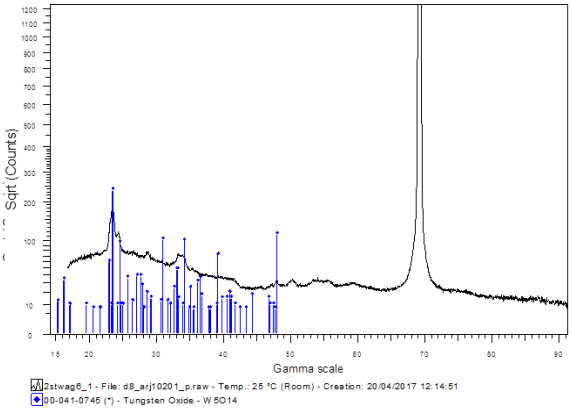

Fig.3. XRD spectrum of sub-stoichiometric WO_3.

3. Results

As is shown in fig.1, we obtained WO_3 nanoneedles with homogenous and randomly oriented distribution on the sensors´ surface. WO_3 NNs conform a 10 µm thick layer and have a diameter of 15-200 nm. Doping procedures by AACVD and sputtering generate different visual results in morphology due to the presence of carbon on NNs in the case of AACVD doping as consequence of precursor residues in synthesis process as is shown in fig. 2. By means of XRD analysis we could check growth of sub-stoichiometric WO_3. This is a proof of existence of oxygen vacancies in material lattice which improve the sensitization mechanisms.

Gas sensing tests were made by measuring dc resistance changes. Pure WO_3, and with AACVD and sputtering doped ones were tested at operating temperatures of 150, 200 and 250 ºC. In all cases sensors were exposed to 5, 10, 15 and 20 ppm of H_2S. Fig. 4 and 6 display sensor responses for 3 cycles of different concentrations of H_2S. In fig. 5 we can observe pure WO_3 sensor present best response at lower operating temperature, while AACVD doped one present its best response at 200 ºC. It would be necessary to study the behaviour of pure WO_3 senor at lower temperature in order to determinate if response keep increasing with temperature decreasing. Fig. 6 and 7 show a comparison among responses of pure WO_3 sensor and sputtering doped ones. In this case all sensors have a lower response when temperature is increased. In the case of sputtering doped sensors we can observe an increase in their baseline resistance. It can be due to the decrease of conduction channel in tungsten trioxide nanoneedles caused by the formation of junction with silver oxide nanoparticles. This result can be confirmed by means of X-ray photoelectron spectroscopy (XPS) or high resolution TEM in order to look for silver nanoparticles, which are not detected with the instrument we used in morphological and composition characterization.

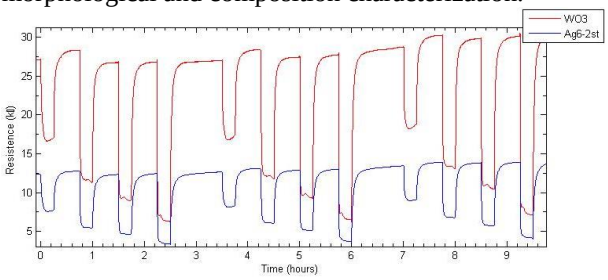

Fig.4. Pure WO_3 and AACVD doped sensor response at 150 ºC.

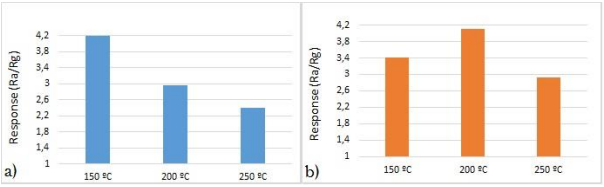

Fig.5. Response to 20 pm of H_2S. a) Pure WO_3 b) Ag6-2st.

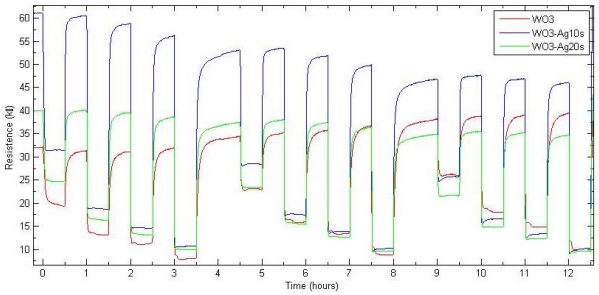

Fig.6. Pure WO_3 and sputtering doped sensors response at 150 ºC.

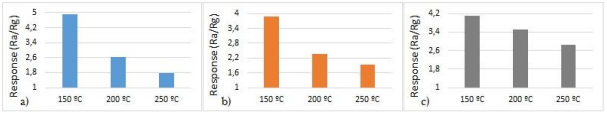

Fig.7. Response to 20 pm of H_2S. a) Ag_sputt10sec b) Ag_sputt20sec c) pure WO_3.

4. Conclusions

Silver doped tungsten trioxide based gas sensors were synthesized using one and two step AACVD methods. XRD analysis showed that the WO_3 nanoneedles grown have a sub-stoichiometric character, which improves the gas sensitization mechanisms. XPS and HRTEM are necessary to confirm the growth of silver nanoparticles on WO_3 NNs because with the detection limits of the instruments we used is not possible to detect them. In the case of AACVD doping process we obtained results which can be attributed to the presence of carbon as residue of the synthesis procedure. On the other hand sputtering doped sensors showed a behaviour which can attributed to formation of heterojunction between tungsten trioxide (n type) and silver oxide (p type).

References

[1] Yamazoe, N. and K. Shimanoe, Overview of Gas Sensor Technology, in Science and technology of Chemiresistor gas sensor, D.K. Aswal and S.K. Gupta, 2007.

[2] Metal Oxide Nanomaterials for Chemical Sensors. Integrated Analytical Systems, ed. R. Potyrailo. New York: Springer, 2013.

[3] Liu, X., et al., A Survey on Gas Sensing Technology. Sensors. 12: p. 9635-9665, 2012.

[4] Wang, C., et al., Metal Oxide Gas Sensors: Sensitivity and Influencing Factors. Sensors. 10: p. 2088-2106, 2010.

[5] Choopun, S., N. Hongsith, and E. Wongrat, Metal-Oxide Nanowires for Gas Sensors, InTech, 2012.